Doctoral Dissertation
Doctoral Program in Energy Engineering (34^{th}cycle)

Advanced modelling of the CR apparatus, design of innovative injection system architectures and assessment of new strategies for the injected mass control and combustion noise evaluation in diesel engine

By

Zhiru Jin
******

Supervisors:
Prof. Alessandro Ferrari

Doctoral Examination Committee:
Prof. Zhijun Wu, Referee, Tongji University
Prof. Antonio Garcia Martinez, Referee, Universitat Politècnica De València
Prof. Tommaso Lucchini, Referee, Politecnico di Milano
Prof. Giacomo Falcucci, Referee, University of Rome "Tor Vergata"

Politecnico di Torino
2022

Declaration

I hereby declare that, the contents and organization of this dissertation constitute my own original work and does not compromise in any way the rights of third parties, including those relating to the security of personal data.

Zhiru Jin

2022

Abstract

The Common Rail (CR) fuel injection system has been introduced into the market for ages and the investigation has been continuously carried out. CR apparatus enables to achieve high nominal pressure and various injection strategies and it has been considered as a key for the further development of modern diesel engines. The investigation of the CR system has been put forward in different aspects: pressure and injected mass control strategies, innovative system layout and the pollutant emissions improvement, etc.

In this study, the diesel CR system control has been investigated. A previously developed numerical model pertaining to the proportional-integrative-derivative (PID) controller and the pressure control valve of a CR system (electronic, electrical, hydraulic and mechanical aspects were considered) has been validated and optimized. Parametric analyses on the PID controller parameters have been conducted under different working conditions. Moreover, the effect of the accumulator size on the rail pressure time history has been studied when the rail volume is dramatically reduced and it suitable solutions for a fuel injection system without rail have been determined.

With regard to the system layout, an innovative Common Feeding (CF) fuel injection system without rail has been developed for a light duty commercial vehicle diesel engine. In the CF apparatus, an additional delivery chamber is mechanically fit at the high-pressure pump outlet and the rail is removed from the hydraulic circuit. The benefits pertaining to the CF system are the low production costs, the easier engine installation and the prompter dynamic response during transients. Experimental tests have been performed on the test bench with different accumulation volumes integrated at the pump delivery for various injection strategies. In general, the injection performance of the fuel injection system did not vary significantly when the pump delivery changed volume or its shape was modified. In addition, an injection system

numerical model has been developed and validated in order to study the reduced accumulation volumes lined phenomena.

As far as the injected quantity control strategy is concerned, an estimation method of the injected mass based on time-frequency analysis has been proposed for a passenger car CR injection system. The injector inlet pressure time history measured by means of a pressure transducer has been processed with the short time Fourier transform (STFT) technique in order to realize a virtual sensor of the injector needle. The injection temporal length (ITL) has been obtained by identifying the SOI (start of injection) and the EOI (end of injection) of the injection. A correlation between the ITL and injected mass has been determined at different nominal pressures and it has been discovered that it is independent of the fuel tank temperature variation. Therefore, the injected mass can be calculated by means of the above correlation and the estimation of the ITL with the TFA based virtual sensor features an overall accuracy below 2mg.

With regard to the combustion noise modelling, an innovative algorithm based on the time-frequency analysis technique has been developed to calculate an instantaneous combustion noise. The input parameter is the in-cylinder pressure signal, measured on a Euro 5 diesel engine during the combustion process, and the quantitative contribution pertaining to the different combustion phases has been evaluated. The algorithm for the evaluation of the instantaneous combustion noise contribution has been realized through a home-made tool and single and multiple injection strategies have been considered. The time-frequency analysis enables to identify detailed information on the contribution of the various combustion phases and the causality relationship between the injection schedule and combustion noise could be obtained.

Keywords: Common Rail, system control, Common Feeding, time-frequency analysis, injected mass, combustion noise.

Acknowledgements

to the past
to the present
to the furture

Contents

List of Figures

List of Tables

Nomenclature

Roman Symbols

A restricted flow-area

$bmep$ brake mean effective pressure

C geometric constant of the magnetic circuit

CF Common-Feeding

$Cn, \dot{C}n$ combustion noise, instantaneous combustion noise

CR Common-Rail

CW Choi-Williams distribution

D diameter of the valve seat; derivative part

d_{or} orifice diameter

DC duty cycle

DT dwell time

E signal energy

E_f energy of a signal

ECU Electronic Control Unit

EGR exhaust gas recirculation

EOC end of combustion

ET energizing time

F force

f frequency

$f(t)$ signal function

FFT Fast Fourier transform

FMV fuel metering valve

G system transfer function; mass flowrate

h window function

$HCCI$ homogenous charge compression ignition

HHR heat release rate

I electric current; integrative part

ITL injection temporal length

K PID controller gain; geometrical term

k spring stiffness

m valve armature mass; polytropic exponent

M_{inj} injected mass

MIF mean instantaneous frequency

n engine speed

NCD nozzle closure delay

NCS Needle Closing Sensor

NOD nozzle opening delay

P proportional part; energy density spectrum

p pressure

P_f energy density spectrum

p_{inj} injector inlet pressure

p_{nom} nominal rail pressure

$PCCI$ premixed charge compression ignition

PCV pressure control valve

PID Proportional-integrative-derivative

PWM pulse width modulation

S surface

SCW Smoothed Choi-Williams distribution

SOC start of combustion

SPL sound pressure level

$STFT$ short time Fourier transform

t time

TDC top dead center

TFA time-frequency analysis

V volume

V_{cc} control chamber volume

V_{dc} delivery chamber volume

$x, \ddot{x}, \dot{x}$ valve displacement, velocity and acceleration

x_b mass fraction burned

ET energizing time

p_{nom} nominal rail pressure level

Greek Symbols

α valve-seat cone semi-angle

β valve damping coefficient

Δp pressure drop

μ dynamic viscosity; flow coefficient

ν frequency

ω crankshaft angular velocity

σ coefficient of variation

τ time

θ flux-force angle; crank angle

ε injected mass difference

Mathematical Symbols

3D   three-dimensional

Subscripts and superscripts

acc accumulator

aft after injection

dyn dynamic

$main$ main injection

pil pilot injection

after   after injection

c   compression phase

comb   combustion

cyl   cylinder

d   derivative part

e   expansion phase

fl   flux forces

i   integrative part

inj   injected

mag   magnetic

main   main injection

nom   nominal value

ov   overall

p   proportional part

pc   pressure control

ref   reference

tot   total

Chapter 1

Introduction

1.1 Background and importance

Internal combustion engines are facing considerable challenges due to their role in energy consumption, environemental pollution and climate change [1].

Researchers and engineers are forced to achieve further progress on an already existing technology, driven by the more stringent and severe pollutant emission strandards [2]. All the elements of the powertrain are involved in this development. Improvements in the combustion chamber shape, affecting the soot formation and in-cylinder nitrogen oxides (NO_x) in diesel engines [3]. Development in the aftertreatment systems through which a sensible reduction of pollutants can be achieved [4]. Optimization in the fuel injection system apparatus, that has a key role in a powertrain since combustion [5], emissions [6] and efficiency [7] are strongly related to the injection events.

The Common Rail (CR) fuel injection system has given many degrees of freedom in terms of injection timing, injection rate and number of injection events during a single engine cycle [8].

Due to its versatility, the CR system has been in-depth explored in numerous research activities, also by means of 1D numerical diagnostic tools, leading to the design of innovative control strategies to improve its performance, the development and optimization of new fuel injection system layouts and to enhance the quality of numerical simulations, regarding the overall injection system, the injector or the high-pressure pipelines, studied with the assumption of the 1D flow.

1.2   Contributions and outline

In this work, diesel Common-Rail system control along with the parametric analyses on the PID controller have been achieved with a fully predictive numerical model. Moreover, the effect of the accumulator size on the rail pressure time history has been studied. The development of a Common Feeding (CF) system without rail for commercial light-duty vehicles within the framework of a cooperation with a Chinese firm (Nanyue Fuel Injection Systems Co., Ltd) has been carried out.As far as the injected quantity control strategy is concerned, an estimation method of the injected mass based on time-frequency analysis has been developed for a passenger car CR injection system. The combustion noise modelling has been charactized. The instantaneous combustion noise pattern has been realized by analyzing the in-cylinder pressure signal with the time-frequency analysis technique.

In Chap. 2, a previously developed numerical model pertaining to the proportional-integrative-derivative (PID) controller and the pressure control valve of a Common Rail system (electronic, electrical, hydraulic and mechanical aspects were considered) has been optimized. Parametric analyses on the PID controller parameters have been analysed under steady-state and transient working conditions. Moreover, the effect of the accumulator size on the rail pressure time history has been studied when the rail size is dramatically reduced. The suitable solutions in terms of the PID controller parameter and of the system sampling frequency for a fuel injection system without rail have been determined. This chapter is based on a scientific paper that was published in [92].

In Chap. 3, the innovative common feeding (CF) fuel injection system has been designed and manufactured for Asia market for the application to light-duty commercial vehicles. With regard to CF apparatus, at the outlet of high-pressure pump a delivery chamber has been mounted and the rail is absence in the hydraulic circuit, compared with the common rail (CR) system. Experimental tests pertaining to the prototypal CF system and CR system have been performed on a hydraulic test rig for the performance comparison under single injection as well as double injections. For different rail sizes, the pressure time histories inside the high-pressure circuit and the injected flow rates have been collected. Injector leakages including static and dynamic, the nozzle opening and closure delays and also the injected quantity dispersion pertaining

to cycles have also been considered. As far as the numerical diagnostic model of the injection system has been concerned, the model has been developed and validated in order to analyze different rail volumes linked effect acting on the injector. This chapter is based on a scientific paper that was published in [23].

In Chap. 4, an innovative estimation method of the injected mass based on time-frequency analysis has been developed for a passenger car CR injection system. The injector inlet pressure time trace measured by means of a pressure transducer has been processed with the short time Fourier transform (STFT) technique in order to realize a virtual sensor of the injector needle. The injection temporal length (ITL) has been obtained by identifying the SOI and the EOI of the injection. A correlation between the ITL and injected mass has been determined at different nominal pressures; it is independent of the fuel tank temperature variation. Therefore, the injected mass can be calculated by means of the above correlation and the estimation of the ITL with the TFA based virtual sensor: the method features an overall accuracy below 2mg. This chapter is based on a scientific paper that was published in [93].

In Chap. 5, it has been focused on combustion noise modelling. An innovative algorithm based on the time-frequency analysis technique has been developed to calculate an instantaneous combustion noise. The input parameter is the in-cylinder pressure signal, measured on a Euro 5 diesel engine during the combustion process, and the quantitative contribution pertaining to the different combustion phases can be evaluated. Single and multiple injection strategies have been considered in the current study. The time-frequency analysis enables more detailed combustion information to be identified and the causality between injection strategy and combustion noise to be better emphasized.

1.3 Research activities general descriptions

1.3.1 CR injection apparatus modelling and analysis for the standard and decreased volume sizes

The development progress regarding to the diesel combustion engines plays a major role for the improvement of the engine-out pollutant emissions, fuel economy and the generated combustion noise [9–11]. The scientific research have

been focusing on various aspects and recently some efforts have been devoted in the development of the fuel injection system modelling [12, 13]. This work which mainly deals with the development of the accurate simulation tools enables the hydraulic behaviour of each component to be further investigated and the fuel injection system performance could be improved without demanding a huge experimental tests. In recent times, experimental tests and numerical simulations have been carried out to further develop the control strategies focusing on the rail pressure signal [14]. The innovative strategy could realize the control strategies of non-linear type [15], and new hardware components involved [16] as well as the overall system dynamics analysis [17, 18]. The mentioned studies deal with the dynamic interaction occurred among each component and it becomes a fundamental role when some significant modifications in the high-pressure hydraulic circuit have been taken into account [19]. It can be inferred that a global predictive numerical model pertaining to the injection system progress enables to make a significant contribution to analyse and optimize the system performance. One benefit of investigating the fully predictive injection system models is the reduced number of injection apparatus prototypes as the boundary conditions pertaining to the developed tool are the diagnostic models instead of experimental test data [20]. In the current research, an existing predictive model of a Common Rail (CR) fuel injection system which has been carried out by [21] has been further improved through the completion of the submodel regarding to the pressure control system.

As far as the controller type has been concerned, the proportional-integrative-derivative (PID) controller has been mostly chosen for the fuel injection apparatus as it is simple and robust during the application [22]. The validation of the upgraded model pertaining to the CR system has been completed by the comparison with the experimental data and the thus validated model has been applied to the PID controller parametrical design analysis. The causal effect of the PID controller operating mode on the rail pressure trace are stated in the current research under both steady state and transient working conditions. Moreover, the criteria to select the optimized settings for the PID controller are established. Eventually, the upgraded predictive model has been utilized to study the accumulation volume effect on the fuel injection system performance. For a rail volume reduced markedly, the PID parameters and the pressure-sensor sampling frequency modification have been analyzed by means

of the new injection system model. This study has been carried out also for the activity reliability regarding to the innovative fuel injection system apparatus without the rail, namely CF system [17, 23], or when the rail size is reduced significantly.

1.3.2 Application of a prototypal Common Feeding injection system

The high-pressure common rail (CR) fuel injection system has been developed since 20th century and then been applied to the diesel engines [24, 25]. The improvement on the performance of the current CR system keeps undergoing in order to meet the emission standards and final user requirements [26]. Different research have been carried out from different aspects, such as the optimization of the combustion chamber [27], the improvement of the aftertreatment system [28], the introduction of new fuel and fuel blends [29]. CR injection system is equipped with a high pressure control system in order to stabilize the high rail pressure and the mass injected could be controlled [30, 31]. For the modern diesel engines, different injection parameters and characteristics could be managed and possessed by the state-of-the-art CR systems with a robust, accurate and fast response under every working condition [32, 33]. Recently, the researchers have been contributed to different aspects of the CR system improvement. The solenoid injectors have been equipped with the pressure balanced pilot valve for reaching higher nominal pressures but still producing small value of static leakage which features the benefit of smaller system energy consumption [30]. By introducing the Minirail into the injector part, the pressure waves oscillations have been restrained and part of injector inner leakage paths have been avoided [31, 32]. With regard to the innovation of injector, a control-plate installed in the control chamber is able to restrict the fuel flow path through the pilot valve during the opening [33]. The wobble-plate-type fuel pump designed for the CR system allows the engine to be fueled with dimethyl ether [34]. The innovative closed-loop control strategy aimed at injected mass control has been presented in order to improve the engine performance. The methodology to obtain the effective injected fuel quantity is based on the analysis of the pressure time history along the high-pressure circuit. A real-time control on the nominal pressure or energizing

time for each injection event could be realized for an accurate injected mass control [35–37]. Despite of the studies focused on the modifications of injection system or on the implementation of the control strategies, the structure of the CR system has also been investigated and certain innovative changes have been put forward [38]. The cost/performance trade off should be paid attention while designing the system [39]. The idea of removing the rail but integrating a chamber into the high-pressure pump, namely Common Feeding (CF) system, has been realized and received great interest from economic point of view [19, 39]. In the current study, an innovative CF prototype system has been developed and implemented on a light duty commercial diesel engine. Comparison of the injection performance has been performed on single and multiple injections pertaining to the CR and CF system. Moreover, a 1D predictive model has been realized for the study on the cause-effect relationship related to the volume size.

1.3.3 Closed-loop control strategy of injected mass on the basis of time-frequency analysis

Under the continuous development of the internal combustion engine, the diagnosis and real time monitoring of the system is becoming more and more important. As far as diesel engine is concerned, the topic related to the injected mass accurate control of the diesel injection systems is shown to be great interest among the real time monitoring aspect [40]. After certain calibration tests, the injected quantity could be obtained with the information of nominal rail pressure p_{nom} and the energizing time ET by means of the ECU calibration maps [41]. The above procedure is the so-called open-loop injected mass control as no feedback signals have been applied. Under different engine thermal regime, the injected mass varies under the same values of p_{nom} and ET [42]. It also results in a bad performance especially under a multiple injection strategy where the pressure oscillations excited by the injector opening and closure events affect the fuel injected quantity [43]. In this way, the assessment of the robust closed-loop control strategies of the injected mass is necessary and becomes the main topic of many diesel engine studies. The injected mass estimation has been determined through the correlation between the needle lift and the fuel volumetric flowrate as well as the fuel properties under the current

thermal regime in [44]. Another strategy, proposed in [45], is achieved with the information of the oxygen concentration at the exhaust manifold collected by the lambda sensor. By computing the difference in oxygen fractions between the flowrates entering and existing the cylinder, the injected mass can be estimated.

Recently, various injection apparatus suppliers have put effort and released different advanced compensative strategies aiming to improve the injected mass accuracy. The i-ART injector, proposed by Denso, is equipped with the piezoelectric pressure sensor at the pilot stage [**?**]. By analyzing the measured control chamber pressure time history, it is able to detect key time instants for example the start of injection, the time when the maximum injection rate achieved and the end of injection. The injected mass is then estimated by a flow-rate model [46]. Another method is realized with the detection of the needle lift trace obtained from the fuel pressure collected by the sensor, the injected mass is then computed by means of a needle model [47]. The above technique is the so-called NCS (Needle Closing Sensor) that is developed by Bosch. The last technology is from Delphi which is realized by analyzing the opening and closure of the nozzle time instants [48]. It is identified by the measured voltage inside the injector since the electric circuit behaves in different ways under the non-ballistic needle reached the nozzle seat and the stroke end. With these techniques, the improvement of the injected mass accuracy could be achieved under the working condition where the correlation fits. Moreover, the application of complex transfer functions and models leads to a non physical and difficult control strategy. Time-frequency analysis (TFA) has been commonly applied to non-stationary signals and it has been introduced to diesel engines combustion study and machinery fault detection [49, 50]. By evaluating the vibration signals through this powerful tool, the knock and injector faults could be detected in these engines [51, 52]. The combustion parameters such as the peak combustion pressure and pressure rise rate [53], the main events of an injection [54] have been identified by means of short-time Fourier transform ($SFTF$) analysis on the in-cylinder pressure time history.

The innovative method for the injected mass estimation is based on the TFA where the correlation between the injected mass, injection temporal length (ITL) and the nominal rail pressure p_{nom} has been built. A robust, closed-loop control of the injected mass has been reached.

1.3.4   Time-frequency analysis application to combustion noise in CI engines

The development of the diesels engines has been focused on the engine performance and exhaust emissions aspects [55, 56]. Among these, the more and more stringent regulations and the acoustics demand from the customers leads the investigation working on the NVH analysis to be more urgent and important [57–60]. With regard to the diesel engine noise, it is composed of mechanical and combustion-related noise [61, 62]. The engine components, such as gears, valves, camshaft and crankshaft, injectors, release noise which is the function of the engine speed and is not related to the combustion event is the so-called mechanical noise [63, 64]. During the combustion, the rapid and sharp increase rate of the pressure results in the high-pressure waves and then the waves radiate to the engine structure forming the combustion noise [65]. Since the resulted noise is generated by the gas force directly due to the combustion event, it has been defined as the direct combustion noise. Another portion of the combustion noise is named as the in-direct combustion noise which comprises the noise originated by the rotary and piston normal force due to the reciprocating piston motion [66]. The combustion noise is closely related to the in-cylinder pressure rise rate as well as the heat release rate peak value and the combustion duration [67–70]. Indeed, the latter two parameters have been expressed to represent the intensity related to the premixed phase which is often considered as the predominant part in the total combustion noise [71]. Nevertheless, a trade-off is usually discovered between the combustion noise and the engine performance [72]. The present innovative modern combustion technologies have improved the pollutant emissions while the combustion noise performance becomes worse [73]. By manipulating the fuel injection timing either advanced or delayed, the premixed charge compression ignition (PCCi) strategies can be implemented [74]. By applying the advanced fuel injection along with a high portion of EGR rate, the NO_x pollutant and soot emissions could be reduced due to the longer ignition delay and the more homogenous combustion mixture [75–77]. On the other hand, the faster and prompter burning phase pertaining to the premixed phase results in a higher combustion noise with respect to the conventional one [78–80]. Conversely, the fuel injection timing after TDC, namely late PCCI, is able to reduce combustion noise [81]. In conventional diesel combustion, by splitting the injection into several shots

in order to realize multiple injection strategy has been proved to be beneficial for combustion noise reduction [82, 83]. The introduction of the pilot injection before the main injection has potential to decrease combustion noise due to the reduced main ignition delay [84, 85]. The dwell time influence on the combustion noise has been analysed in [37] and it has shown that in the digital rate shaping regime the noise decreases obviously with dwell time. This could be explained by the heat release rate (HRR) pattern [86, 87]. The application of multiple injection strategy leads to a lower combustion noise due to the smaller maximum HRR [88]. The HRR pattern has been manipulated to be as linear as possible for the cases with three and four pilot injections in order to achieve the optimized combustion noise [89]. The general method to evaluate the combustion noise is based on the time-frequency analysis applied on the in-cylinder pressure signal. A fast Fourier Transform (FFT) is applied to the cylinder gas pressure signal to obtain the corresponding power spectrum [90]. The effective combustion noise level has been defined as by applying two types of filters with regard to the frequency attenuation effects of the human hearing system and the engine [91]. Based on the obtained combustion noise Fourier spectra, the dominant frequency range pertaining to the largest contribution to the overall combustion noise could be identified. However, it is not able to quantify the contribution from different combustion phases during the combustion process. Lately, the time-frequency analysis has been developed and implemented in the real-time performance monitoring field for the aim of fault diagnosis. It has been realized by analysing the frequency variations when the combustion is taken place [52]. In the current study, time-frequency analysis has been applied to detect each combustion phase during the combustion period and the corresponding contribution to the direct combustion noise has been assessed. The presented methodology could be implemented in the ECU for real-time controlling and diagnosis. Moreover, it could be used for validating and refining the combustion models.

Chapter 2

CR injection apparatus modelling and analysis for the standard and decreased volume sizes

2.1 Experimental setup and the measurement devices

A Common Rail (CR) diesel injection system which features a 700 mm^3 displacement of high pressure rotary pump, a 20 cm^3 internal volume of rail and three solenoid type electroinjectors has been adopted. The applied injectors is equipped with a Microsac nozzle and features 7 injection holes. The rail-to-injector pipe has a length of 200 mm and an internal diameter of 3 mm.

With regard to the system pressure control, two types of devices have been included in the CR diesel injection system. A pressure sensor and a pressure control valve (PCV) have been equipped on the rail. The other is a fuel-metering valve (FMV) which is mounted at the inlet part of the pump for the aim of controlling the absorbed flowrate based on the injector requirements and the high-pressure control system efficiency has been improved. In the current work, the PCV has been selected to control the high pressure instead of the FMV. The experimental tests have been performed with a solenoid actuated CRI 2.18

injector which features a pressure-balanced pilot-valve aimed at reducing the static leakage as well as optimizing the multiple injection control.

The experimental tests regarding to the injection system have been carried out at the Moehwald-Bosch hydraulic test bench located at the Internal Combustion Engine Advanced Laboratory (ICEAL) of the Politecnico di Torino. The test rig is equipped with the piezoresistive transducers and the thermal-couples in order to acquire the pressure transients and the temperatures at different locations inside the high-pressure hydraulic circuit of the injection system. With regard to the instantaneous injected flowrate and the injected quantity during the tests, the Mexus flowmeter has been installed to collect the data of one injector. The electric driving signals acting on the injectors have been acquired by means of a current clamp. Furthermore, the injector leakages happened during the injection event have been collected through KMM flowmeter.

2.2   PID controller and PCV submodels

A previously homemade predictive model, reported in Fig. 2.1, has been developed for the 1D simulation with regard to the CR system in [21]. It has been made up of various submodels pertaining to the high-pressure pump, the injectors and the rail which are presented in Fig. 2.1a. The hydraulic model includes several chamber elements which are in zero dimension and they are coupled through one dimensional orifices or pipes. The barotropic flow has been considered and the corresponding ordinary and partial differential equations have been computed and solved with the Newton equations regarding to the valves mobile elements. Fig. 2.1b refers to the scheme of the tested injector. More detailed information related to the pump hydraulics and mechanical submodel have been reported in [94].

The presented CR system model has been further developed by adding another submodel which stands for the PCV installed in the rail. The original rail submodel, which was considered as a pure hydraulic capacitance, was performed to simulate the valve through a varied flow-area throttle based on the PID controller output demand (cf. Fig. 2.1a). The updated newly PCV submodel contains both mechanical and hydraulic components as shown in Fig. 2.2a. Based on the schematic drawing, port 1 refers to the connection

of the fuel flowing into the rail and port 2 indicates the fuel passage back to the tank. A restricted flow-area, expressed as A, is presented between port 1 and 2 varying as a function of the armature lift x. The mechanical equilibrium
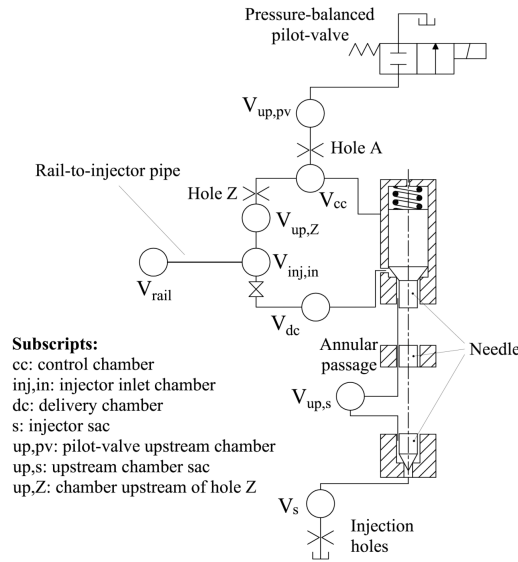
(a) The sketch of the CR system model.
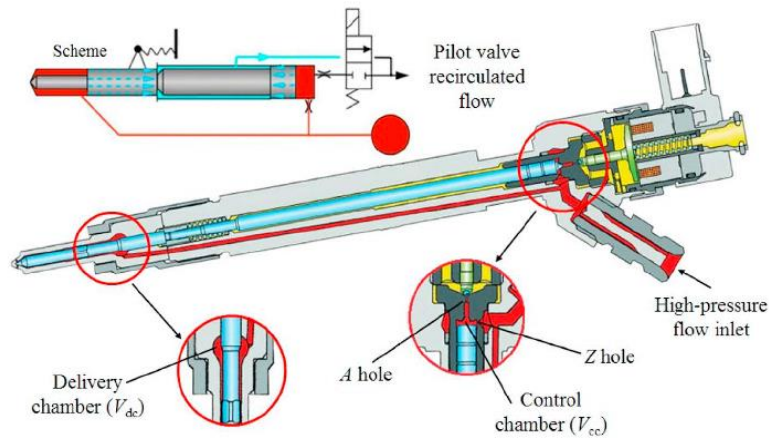
(b) The drawing of the applied solenoid injector.

Figure 2.1: CR injection system model and the tested CR injector.

equation pertaining to the PCV armature has been expressed as:

$$m\ddot{x} + \beta\dot{x} + kx = p_{rail}S - F_{mag} - F_{fl} \tag{2.1}$$

where m stands for the valve armature mass, β represents the damping coefficient and k is the spring stiffness. The injector receives a force ($p_{rail}S$) from the rail pressure that is acting to open the valve, while the electromagnetic force (F_{mag}) originated from a solenoid output signal pertaining to the *PID* controller results in an opposite direction which is to close the valve. F_{fl} represents the flow force acting at the restricted flow-are between the armature ball valve and the valve seat. Based on the previous study, this force caused by the fluid acceleration tends to close the ball valve and it acts in the opposite direction with respect to the rail pressure force. The flow force F_{fl} is the function of the pressure drop through the *PCV* and the restricted flow-area $A(x)$ which is shown in the following:

$$F_{fl} = 2\mu A(x)\Delta p \cos\theta \tag{2.2}$$

where the valve flow coefficient is expressed by the parameter μ. θ is the flow force angle inclination and it has been estimated as the valve-seat cone semi-angle, expressed as α shown in Fig. 2.2a. The restricted flow-area $A(x)$ could be roughly expressed as $A(X) \approx \pi D x \sin\alpha$ (D is the ball valve seat diameter) since the valve seat features $x/D \ll 1$. Based on the approximation equation, A is proportional to the armature lift x and an equivalent stiffness, namely k_{fl}. The equivalent stiffness with regard to the flow force could be defined as following:

$$k_{fl} = 2\mu\pi D\Delta p \cos\alpha \sin\alpha \tag{2.3}$$

It should be noted that, the equivalence stiffness k_{fl} gives a big contribution to the total system stiffness ($k_{tot} = k + k_{fl}$). To be specific, k_{fl} features a bigger natural frequency value and therefore the frequency response of the valve as well as the pressure control performance have been improved (cf. Fig. 2.2b).

The working principle of the *PID* controller is based on the pressure difference, namely e, between the setting nominal pressure p_{nom} and the real-time rail pressure level $p_{rail}(t)$ as shown in Fig. 2.3. With regard to the controller coefficients, P represents the proportional contribution, I refers to the integrative portion while D stands for the derivative part. The above-

mentioned parameters have been expressed as following: K_p, K_i and K_d. p_{rail} pressure signal has been captured by a rail-integrated pressure sensor every 5 ms and is monitored by the electronic control unit ECU.

To be specific, target value is defined as p_{nom} while the output instantaneous pressure signal is expressed as $p_{rail}(t)$. This $p_{rail}(t)$ is controlled by the
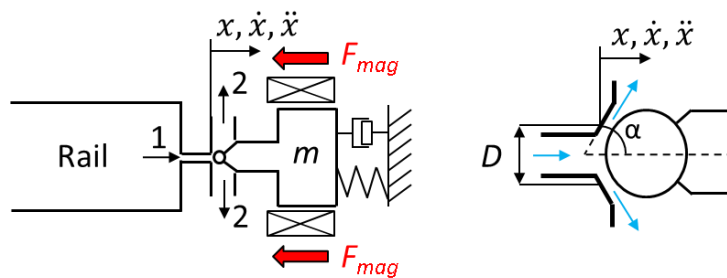
(a) Schematic drawing of PCV submodel.
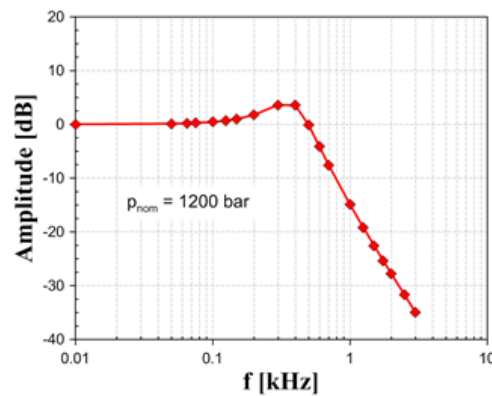
(b) Frequency response of the valve.

Figure 2.2: PCV submodel.

injection system transfer function, namely G_s. The PID controller working on the pressure difference e generates an electric current (I_{PCV}) that should be provided to the PCV solenoid for generating the desired electromagnetic force based on the following equation:

$$F_{mag} = C\mu_0 N^2 I_{PCV}^2 / (1-x)^2 \tag{2.4}$$

where C is a constant coefficient which depends on the geometric sizes of the considered magnetic circuit [20], μ_0 stands for the magnetic constant, N is the PCV controller solenoid turns number and l represents the initial length of the air gap. In practical, the electrical current I_{PCV} has been applied to the PCV through a pulse width modulation (PWM) controller featuring a fundamental frequency of 1 kHz.

In Fig. 2.4, the current signal I_{PCV} has been reported under the working condition $p_{nom} = 1000$ bar and $ET = 3000$ µs. The oscillations of the reported current feature an amplitude of nearly 0.3 A and a frequency of 1kHz with respect to the mean value (expressed with dashed line) which are due to the operation mode of the PWM. Based on Fig. 2.2b, it could be inferred that the optimal operating working frequency range of the PCV controller should be within the range of 0< f< 500 Hz in order to reach a satisfied dynamic response
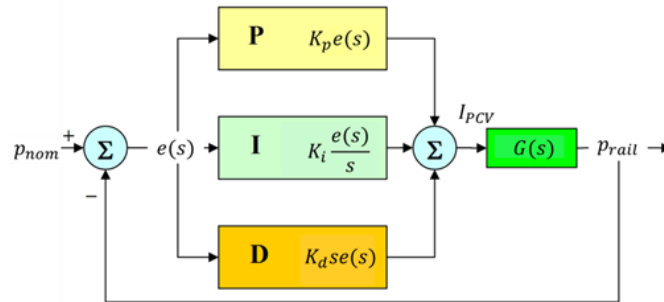
Figure 2.3: Control strategy of the p_{rail}.

while the performance is bad for the condition of $f \geq 800$ Hz. It should be noted that the valve is controlled by the I_{PCV} average value instead of the fluctuations caused by the PWM controller. The validation of the upgraded predictive CR model including the new PCV and PID controller submodels has been realized by comparing the rail pressure and injected flowrate under different working conditions. In order to reduce the prediction errors related to the PID model, a least square technique has been developed to the coefficients K_p, K_i and K_d and the obtained values have been applied preliminarily to the experimental rail pressure data in terms of n=2000rpm under steady-state and transient conditions.

In Fig. 2.5, some steady-state experiments results pertaining to the validation process have been reported in terms of the rail pressure level and injected flowrate. The numerical simulation results are plotted in solid line while the corresponding experimental data are represented with symbols. The almost coincident between the numerical and experimental results under different working conditions shows a satisfied performance and an accurate simulation of the presented predicted pressure control system model pertaining to the steady state working conditions.
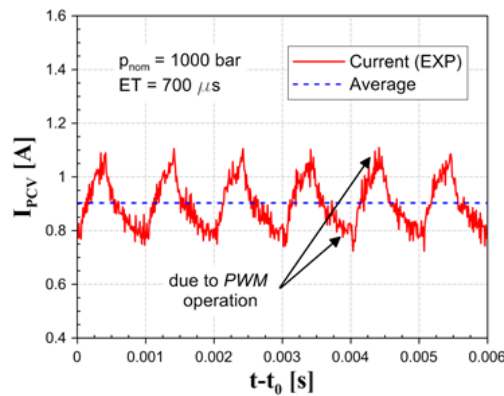
Figure 2.4: The current I_{PCV} provided to the PCV.

2.3 Parametric analysis on the PID controller parameters

In order to study the *PID* controller parameters affect on the performance of the injection system, parametric analyses have been carried out in the present investigation. Figs. 2.6-2.8 refer to the change of K_i, K_p and K_d parameters influencing on the rail pressure trace under p_{nom} step pressure transient conditions (n=2000 rpm). During the practical pressure control, the load transients are more critical than the engine speed transients due to the longer duration for the latter condition. In Fig. 2.6, under an injection event featuring $ET = 500$ μs condition, a rail pressure step transient from $p_{nom} = 600$ bar to $p_{nom} = 1000$ bar has been modified with regard to different K_i values while maintaining the same baseline values of K_p and K_d. The K_i percentage variation is defined as the reference to the corresponding baseline value which has been evaluated during the model validation procedure. It could be seen from the figure that the injection system response time to the nominal pressure step transient decreases with integrative parameter increasing. That is to say, the pressure time history features a steeper slope for a higher K_i. However, a bigger pressure overshoot can be resulted when K_i increases. In the case of "$K_i + 100\%$" (plotted in solid line with rhomboidal symbols), the generated
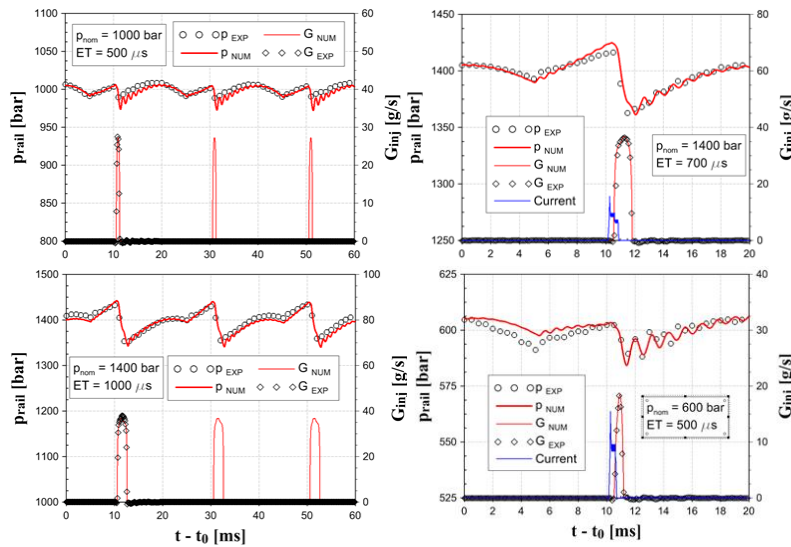
Figure 2.5: The numerical and experimental results for the model validation.

overshoot arrives about 60 bar with respect to the baseline case due to the
doubled K_i. As far as "$K_i + 50\%$" case (plotted in dotted line without symbols)
has been concerned, no overshoot has been observed but the pressure raise
rate appears to be slow, indeed, over 8 engine cycles are needed to reach the
new nominal pressure value. Nevertheless, based on the simulation result, K_i
value as the half of the baseline one is able to exclude the steady-state error
pertaining to the p_{rail} within the simulation time. It does not appear in the
"$K_i \to 0$" case since the reduction rate is not sufficiently fast. It should be
note that a trade-off between overshoot and settling time, that is, the time
required to achieve the target steady-state working condition with an acceptable
tolerance, should be considered when choosing the integrative gain. Fig. 2.6
shows that the baseline case (plotted in solid line without symbols) features a
satisfactory compromise selection since it represents a pressure overshoot value
which is similar to the amplitude of the natural fluctuations of the steady-state
condition rail pressure level and an acceptable settling time.

Fig. 2.7 refers to the influence of K_i on the pressure step change from 1000
bar to 1400 bar. The dotted line indicated as $P \ll I$ represents a pressure
control system with the proportional part shares the less contribution with
respect to the integrative one. Under this control strategy, the steady-state error
pertaining to the rail pressure could be cancelled, however, the performance
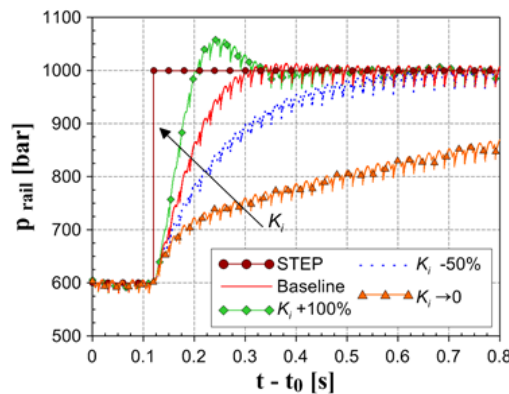
Figure 2.6: Effect of integrative gain on the p_{nom} step change ($ET = 500$ μs).

with regard to the pressure overshoot and settling time become worse. A bigger K_i (the case plotted in solid line with rhomboidal symbols) benefits for a faster settling time and a reduced pressure overshoot during the pressure transients as shown in Fig. 2.7a. The disadvantage caused by a high K_i value is related to the system performance after the step transient is finished. Based on Fig. 2.7b, an extremely high K_i value that is $P \ll I$, plotted with solid line with triangle symbols, results in high oscillations in I_{PCV} and thus leads to a relatively high pressure fluctuations around the desired new pressure level p_{nom}.

The effect of K_d on the p_{nom} pressure step change from 600 bar to 1000 bar has been finally investigated and the result has been shown in Fig. 2.8. The derivative contribution has been set to be null for the baseline case (in the legend of the plot, K_d is a positive value that is doubled in the "$K_d+100\%$" case). As far as the effect of K_d has been concerned, the parametric analysis has been performed and the result indicates that the influence of derivative part is negligible during the steady-state working conditions but it has the influence on the injection system performance under pressure step change case. To be specific, a bigger value of K_d lets the pressure rise in a bigger slope at the beginning of p_{rail} change since a sudden rise occurred in the (p_{nom}-p_{rail}) error as soon as the nominal pressure starts to increase. The rail pressure increase begins to slow down subsequently since the (p_{nom}-p_{rail}) error diminishes. The derivative of the error with respect to time multiplied by derivative coefficient makes a negative contribution to the PID output signal (cf. fig. 2.3). Generally speaking, among all the simulation tests, the pressure overshoot and the settling time are not correlated to K_d value.

Nowadays, the PID parameters tuning could be realized in various approaches in engineering systems. Some procedures, proposed in [95, 96], are still applicable due to the simplicity. In [97], the parameters haven been preliminarily optimized during the experimental tests carried out on the injection system. An improved performance has been achieved by developing a reliable physical model of the fuel injection apparatus without the need of a large number of the experimental tests in [98, 99]. Based on this, the presented upgraded CR system model could be applied to the PID parameters optimization process in order to reach a more refined and efficient tuning method

2.4   Variable coefficient PID strategies

By implementing more complex control methods instead of applying the linear constant coefficients pertaining to PID strategies, the rail pressure control under the transient working condition could be improved. For instant,
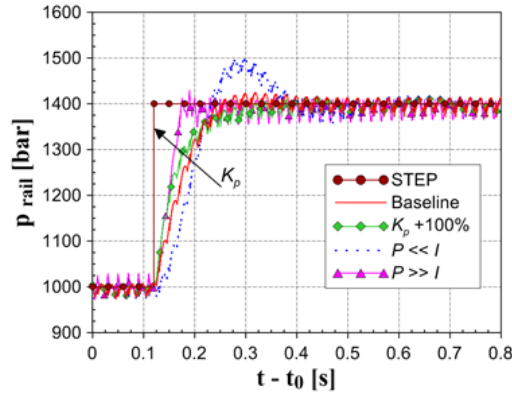
(a) p_{nom} step pressure change
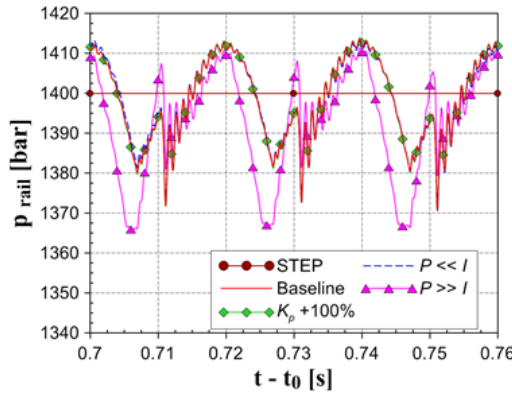
(b) p_{nom} steady state condition

Figure 2.7: Effect of proportional gain on the p_{nom} pressure signal ($ET = 300$ μs).

variable coefficient PID control strategy have been developed based on a certain limit which is set for the $\mid p_{nom}\text{-}p_{rail} \mid$ error. Once this error exceeds the set threshold, the proportional and derivative contributions will be modified to a bigger value in order to achieve the desired advantages. On the other hand, the decrease in the coefficients K_p and K_i will be realized if the $\mid p_{nom}\text{-}p_{rail} \mid$ error is smaller than the limit for the aim of pressure overshoot or the steady-state pressure fluctuations control. Nevertheless, Figs. 2.9 and 2.10 show two examples that the tolerance of 50 bar pertaining to the error $\mid p_{nom}\text{-}p_{rail} \mid$ has been set and the resulted reduction (30 %) in the K_p or K_i do not lead to any obvious beneficial with regard to the rail pressure transient while the steady-state pressure fluctuations have been slightly reduced. In Figs. 2.9 and 2.10, the baseline control strategy referred to the constant coefficient (plotted in lines without symbol) have been compared with the variable coefficient strategy (potted in lines with rhomboidal symbols). It should be noted that when the new working condition is about to reach, the contribution pertaining to the proportional and integrative aspects of the PID controller starts to gradually decrease since the pressure error $\mid p_{nom}\text{-}p_{rail} \mid$ progressively reduce. In this way, these two parts, proportional and integrative parts, begin to reduce the effect within the band and not depend on the corresponding K_p or K_i.
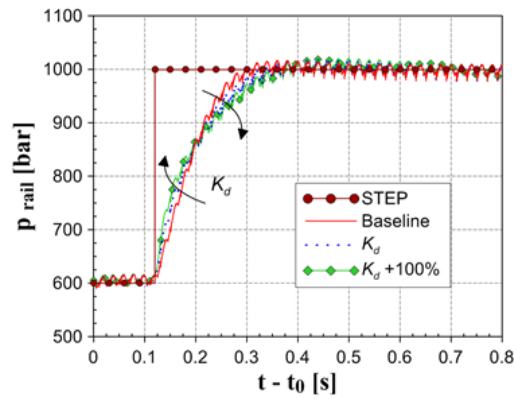
Figure 2.8: Effect of derivative gain on the p_{nom} step change ($ET = 300$ μs).

Moreover, the considered variable coefficient PID control strategy does not show any advantages at the beginning of the pressure step change since the maximum mechanical stress that is allowed on the considered high-pressure pump facilities restricts the pressure rise rate.
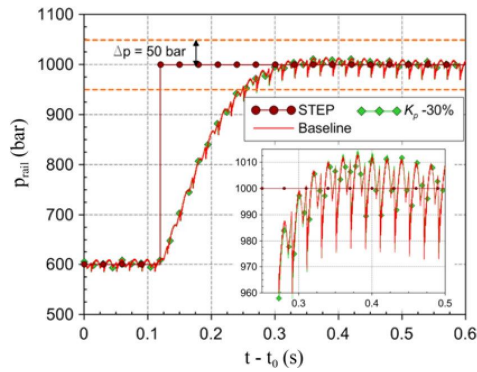
Figure 2.9: Variable coefficient PID strategy: Effect of proportional gain.
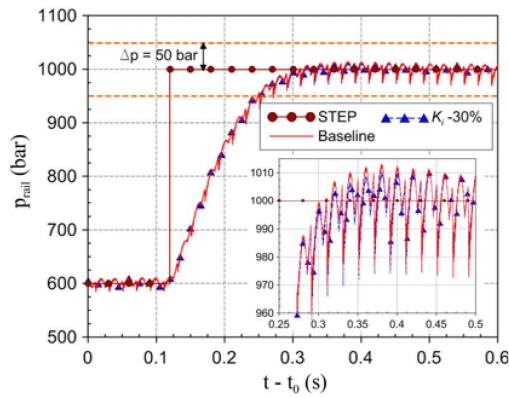
Figure 2.10: Variable coefficient PID strategy: Effect of integrative gain.

With regard to the rail pressure rise rate limitation during the pressure transient process for the Common Rail system, the dedicated calibration maps have been developed and the pressure time derivative value has been limited to 3000 bar /s $^{-1}$ which is enough for the constant linear coefficients PCV control strategy. In other words, the baseline PID control strategy have chosen the value of the constant coefficients K_p or K_i on the basis of the pressure rise rate limit presented in the calibration maps aiming at a faster system response. It should be noted that the cases presented in the Figs. 2.6 and 2.7, where the parametric analyses have been studied, have not expected this dp_{rail}/dt threshold limit but only considered the PID controller coefficients change influences. The complex PID controller method, namely variable efficient control strategy, presents a more efficient control by applying it in FMV based fuel injection systems since a more rapid control process is occurred and this leads to a much higher proportional and integrative coefficients than the one with PCV. In this way, the behaviour of the proportional and integrative parts is shown to be satisfied in the FMV controlled system.

2.5 Volume size variation effect

Based on the cases plotted in Fig. 2.11, it could be concluded that the amplitude of the rail pressure fluctuations tends to increase with reducing the accumulation volume (V_{rail}) during the engine cycle. The working principle of the rail pressure control system in the CR system is to maintain the average value of the rail pressure $p_{rail}(t)$ close to the nominal pressure level p_{nom} regulated by the ECU. Therefore, with regard to a smaller accumulation volume, the initial value of p_{rail} appears to be slightly higher in order to compensate the bigger pressure drop due to the injection event [100]. The injected flowrate pattern remains almost the same when the rail size has been modified, it is also true for a big injected mass as shown in Fig. 2.11 with $M_{inj} \approx 50mg$. An obvious difference could be detected in the latter part of the injection with regard to different rail volumes: a lower rail pressure level has been shown during this period for a smaller accumulation volume and it results in a slightly smaller flowrate and a longer nozzle closure delay which features under 20 ms difference. However the decreased flowrate has been compensated by the higher nozzle

closure delay and finally the injected mass variation is within 1% pertaining to
the reported single injections.

In Fig. 2.12, a double injection strategy has been reported with $p_{nom} = 1000$
bar, $ET_{main} = 500$ μs, $ET_{after} = 150$ μs and $DT = 600$ μs. With regard to
$V_{rail} = 12.9$ cm^3, the injected masses pertaining to main and after injection
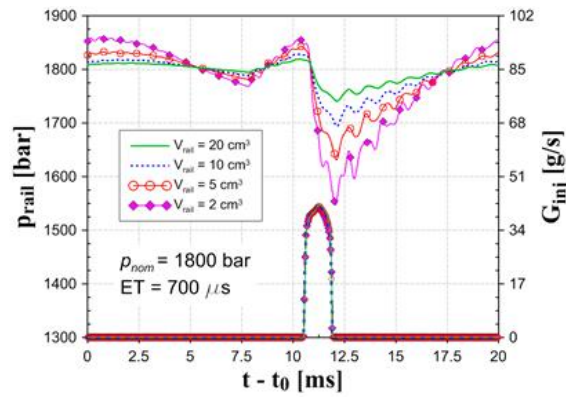
(a) Single injection: $ET = 300$ μs, $p_{nom} = 1800$bar, $n = 2000$rpm
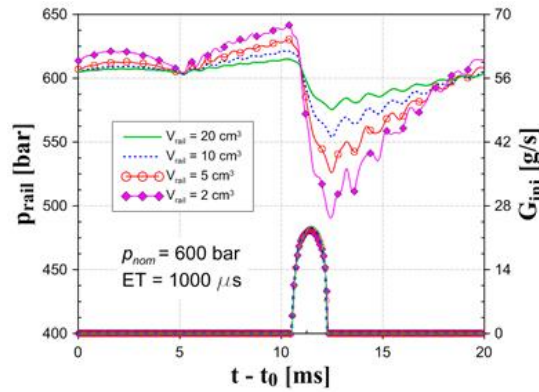
(b) Single injection: $ET = 1000$ μs, $p_{nom} = 600$bar, $n = 2000$rpm

Figure 2.11: Effect of accumulator size on the rail pressure and injected flowrate.

shots approximately equal to 17 mm^3 and 2.5 mm^3, respectively. The above mentioned working condition has been analysed in order to study the influence of a bigger pressure drop value when the main injection finishes for a smaller accumulation size at the presence of the after injection.

The mass variation pertaining to the main injection with respect to V_{rail} is under 3% while the after injection features a maximum deviation of 10% for the $V_{rail} = 2$ cm^3 when comparing with the $V_{rail} = 20$ cm^3 one. With regard to the layout featuring $V_{rail} = 2$ cm^3, the lowest level of the rail pressure signal during $11.5\text{ms} < t - t_0 < 15\text{ms}$ when the after injection is taken place leads to a smallest peak flowrate.

The $V_{rail} = 5$ cm^3 layout has been modified in order to reach the approximately same rail pressure trace as the $V_{rail} = 20$ cm^3 case by means of the developed predictive model through regulating the PID controller coefficients. The pressure control system frequency has been defined as $f_{pc} = 1/\delta t$ where δt refers to the time interval between two continuous electronic control unit evaluations of the rail pressure. Single injections have been selected as example and the pressure control system frequency as well as proportional gain will be adjusted based on the requirement.
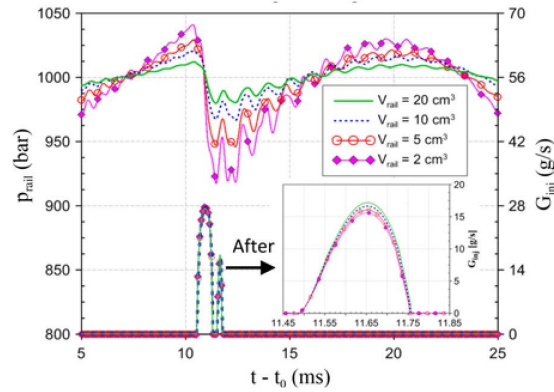
Figure 2.12: Effect of accumulator size on Main-after injections: $p_{nom} = 1000$ bar, $ET_{main} = 500$ μs, $ET_{after} = 150$ μs, $DT = 600$ μs, $n = 2000$rpm.

In Fig. 2.13a, the influence of the proportional coefficient K_p on the rail pressure signal for the accumulator size equal to 5 mm^3 has been shown. It could be concluded that with a bigger K_p which is 5 times the baseline value, the rail pressure trace $p_{rail}(t)$ (plotted in solid line with circular symbols) has been changed with respect to the baseline case. However, such change does not show any advantages when the injection is happened. Another case pertaining to zero contribution of the proportional part, plotted in solid line with rhomboidal symbols, has also been investigated for the $V_{rail} = 5$ cm^3 case and the rail pressure time history appears to be almost coincident with the reference case under a steady-state working condition. Generally speaking, the proportional gain only gives a contribution on the rail pressure when the engine is facing a transient situation. The effect of the system frequency on the $p_{rail}(t)$ pattern has been analysed also for the $V_{rail} = 5$ cm^3 case and the result is shown in Fig.
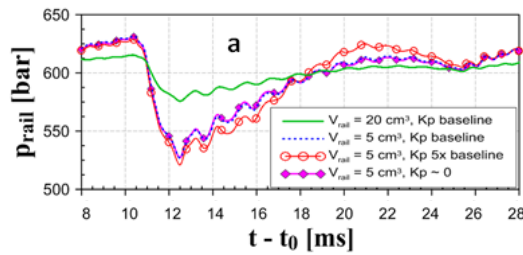
(a) Effect of different K_p values.
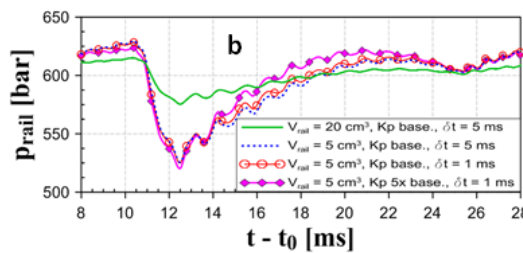
(b) Effect of different δt values.

Figure 2.13: Effect of proportional gain and control system frequency on the rail pressure and the injected flowrate under steady state working conditions ($p_{nom} = 600$ bar, $ET = 1000$ μs, $n = 2000$rpm).

2.13b. The decrease of δt from 5 ms (baseline value) to 1ms, where it refers to the control system frequency increases from $f_{pc} = 0.2 kHz$ to $f_{pc} = 1 kHz$, has no obvious changes on the rail pressure trace. As far as the combination effect has been concerned, the case plotted in solid line with rhomboidal symbols has shown that the significant increase in the control system frequency as well the proportional gain results that the rail pressure starts to increase more rapidly when the injection is finished. In this way, the Minirail dynamic response to the injection event could be optimized. Nevertheless, it should be noted that when the injection is taken place, the rail pressure time history is not affected.

In Fig. 2.14, different accumulator sizes have been analysed under a step pressure transient from $p_{nom} = 1000$ bar to $p_{nom} = 1400$ bar. For a smaller V_{rail} value, the pressure rise rate is higher at the beginning of the step transient since the PCV has discharged some fuel when the p_{nom} varies and the injected flowrate is therefore reduced. Nevertheless, the increasing rate of the rail pressure starts to gradually reduce in the second phase of the transient.

The above explanation has been proved in Fig. 2.15a by plotting the calculated moving average rail pressure time histories corresponding to the ones shown in Fig. 2.14. The time required to reach the new setting nominal pressure has been delayed when the volume size has been reduced significantly.
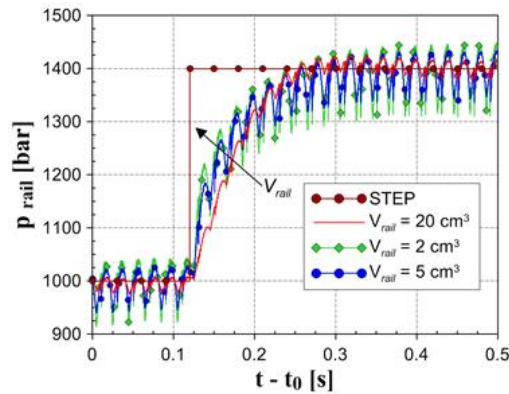
Figure 2.14: Effect of accumulator size under transient condition: from $p_{nom} = 1000$ bar to $p_{nom} = 1400$ bar ($ET = 300$ μs, $n = 2000$rpm.

It is explained by the *PID* controller coefficients setting criteria since it is
based on the baseline volume size $V_{rail} = 20$ cm^3. Another accumulator size
with $V_{rail} = 2$ cm^3 has also been reported and the proportional gain has been
decreased with 90% with respect to the baseline case one (expressed as K_p-90%).
At first, the pressure rise rate is slower and then the pressure starts to increase
rapidly due to the reduced proportional coefficient and finally the performance
behaves similar as the baseline reference. Based on the comparison plot between
$V_{rail} = 2$ cm^3 with K_p-90% and $V_{rail} = 20$ cm^3 which is shown in Fig. 2.15b,
the rail pressure traces for these two layouts are almost the same although the
high frequency pressure waves feature a higher amplitude pertaining to the
smaller rail size one.

The following Figs. 2.14 and 2.15 reveal that a reduced accumulator size is
possible to promote the injection system response since the hydraulic inertia has
been decreased. With regard to the rail pressure control, under a pressure step
transient working condition the rail size does not have any influence by applying
the *PID* controller. In this way it offers a suitable solution for a fuel injection
system without rail and in the Chapter 3 the innovative Common-Feeding
system has been investigated based on the present study.
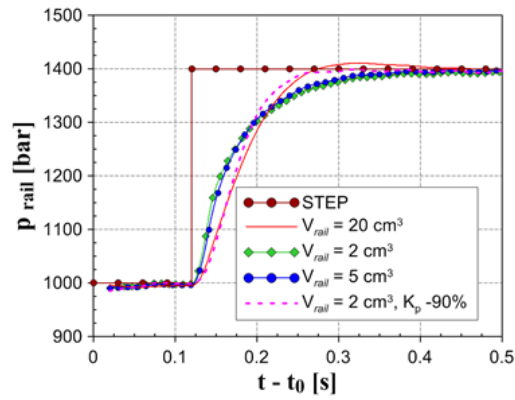
(a) The moving averaged curves of the p_{rail}
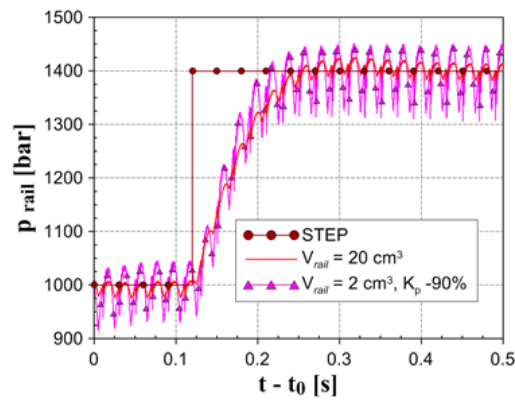
(b) p_{rail} comparision

Figure 2.15: Combined effect of accumulator size and proportional gain on the p_{nom} step change .

Chapter 3

Application of a prototypal Common Feeding injection system

3.1 CR and CF fuel injection systems apparatus

The hydraulic layouts containing the schematic diagram and the photo pertaining to the CF and CR systems have been displayed in Figures 3.1a and 3.1b. In the CR system, the fuel flows out of the high-pressure pump and then reaches the accumulator, the so-called rail, through a pipe that has an internal diameter of 2.7 mm. In the present work, for the aim of analyzing the accumulator size affect, various rail prototypes featuring different volume sizes of 10 cm^3, 4.7 cm^3 and 2.1 cm^3 have been manufactured by changing the internal cylinder diameter but remaining the same total length. Whereas, as indicated in Figs. 3.1b and 3.2, a chamber C (numbered as 4 in Fig. 3.2) has been realized which is a cross shape with an internal volume of 10 cm^3. Three chamber prototypes have been manufactured: an additional gauge orifice has been selected for two of them with the diameter of $d_{or} = 1.2$ mm and 1.6 mm, respectively. The orifice is located at the connecting area between the chamber and the injector feeding pipe and is designed for the aim of pressure waves attenuation. In order to capture the rail pressure time history, a pressure sensor indicated as item 5 in Fig. 3.2 has been mounted inside the chamber

C. With the modifications of the system layout, the CF system leads to a lower cost as well as a simpler installation process. The high-pressure pump is a single cylinder double-acting type for both the CR and CF apparatus. The pump outlet, that is the high-pressure part, is equipped with a solenoid valve (indicated as item 2 in Fig. 3.2) used to regulate the fuel pressure in the high-pressure circuit by discharging the excess pumped fuel during the operation. The parameters of the pipes mounted in both CF and CR systems are $l = 300$ mm of length and $d = 2.7$ mm of internal diameter. The injector features a number of 6 nozzle holes and the diameter is 0.135 mm. In the current research, the injection system is designed for the Asia market of light
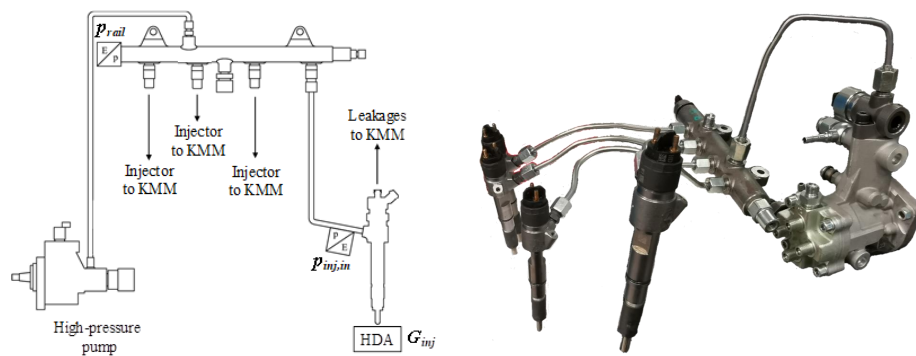
(a) CR system
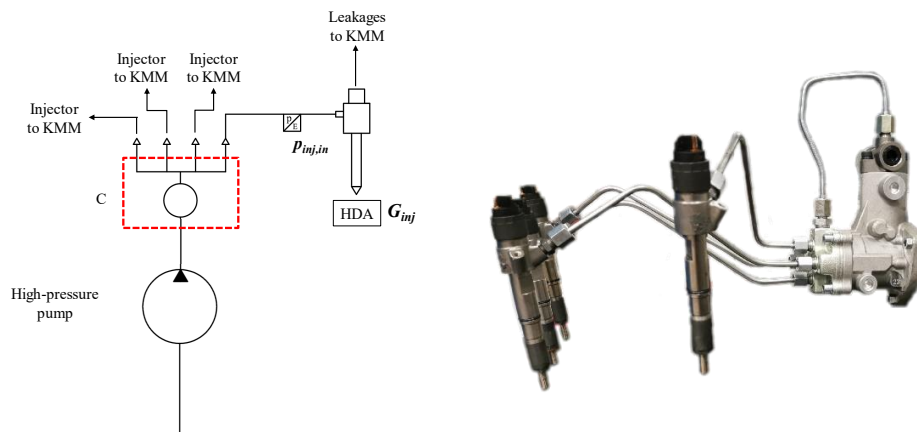
(b) CF system

Figure 3.1: The schematic diagram and the photo of the high-pressure circuit of the CR and of the CF systems.

1. Outlet of the pump
2. Pressure regulation valve
3. Inlet of the accumulator
4. Chamber C (the accumulator)
5. Accumulator pressure sensor
6. Inlet of the pump
7. Outlets of the accumulator
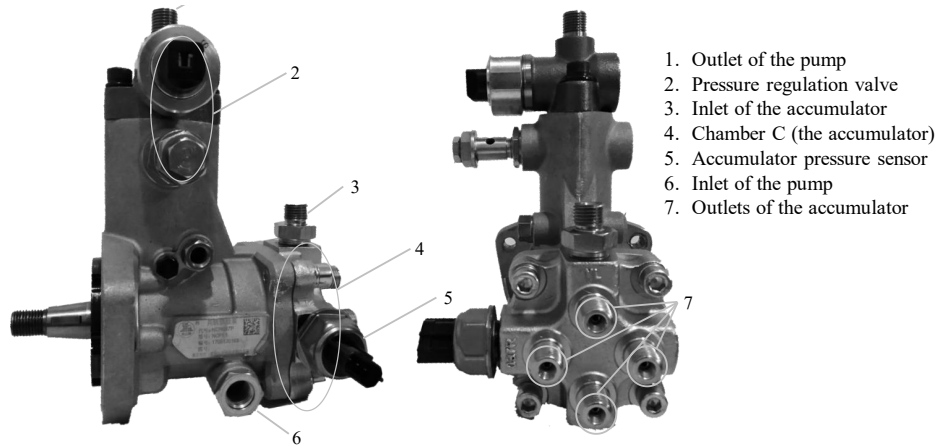
Figure 3.2: The photo of the accumulator fixed in the high-pressure pump.

duty commercial vehicles. In this way, the fuel injected mass defined for each engine cycle is set to be varied from 0.5 mg to 60 mg. The present investigation has been established as a research project that are shared between Nanyue Fuel Injection Systems Co., Ltd. and Politecnico di Torino. The facilities under the research such as the high-pressure pump, high-pressure pipes, injectors and different volumes of rails have been fabricated and provided by Nanyue Fuel Injection Systems Co., Ltd.

3.2   Experimental facility

Both the CF and CR fuel injection systems have been performed at the Moehwald Bosch hydraulic test rig installed in the ICEAL Laboratory of Politecnico di Torino. The bench has the ability to provide 35 kW nominal power, 100 Nm maximum torque and 6100 rpm maximum speed. Figure 3.3, installed with the CR system as an example, shows the schematic drawing of the whole acquisition system with the applied devices.

The test bench is installed with two types of flowmeters which are HDA and KMM. With regard to the working principle of HDA, the pressure signal in a fixed volume is collected based on Zeuch method. In the current project, HDA has been applied to catch the instantaneous flowrate and report the overall injected mass for one injector. KMM connected to the injectors has been used to constantly record the recirculated flowrates within the injectors [30]. As far as the pressure time history along the rail-to-injector pipe has been
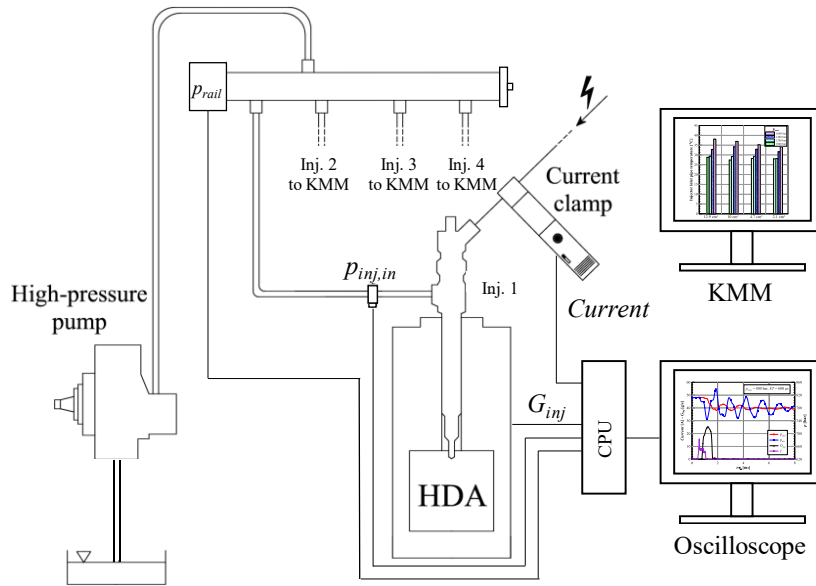
Figure 3.3: Scheme of the acquisition system.

concerned, namely $p_{inj,in}$, piezoresistive type of pressure sensors have been installed to fulfil the aim. The rail pressure transients presented in the CR system are captured by another piezoresistive transducer, while the pressure inside the chamber pertaining to the CF system is not able to be measured. As shown in the plotted diagram, a current clamp has been mounted for the aim of measuring the energizing current applied to the injector. The signal process procedures, that are the pressure transients from the pressure sensor, the instantaneous injected flowrate from HDA and the energizing current from the current clamp, are realized by a CPU. In order to remove the meaningless spurious oscillations presented in the collected signals, the low-pass filter with an adaptable cut-off frequency has been selected and applied in the CPU. The output of the conditioner is connected with an oscilloscope in order to synchronize the acquired signal time histories. It should be noted that, the installed KMM subsystem could also detect the flowed fuel quantity for each engine cycle. In order to simulate the diesel oil properties under an appropriate pressure and temperature scope, Shell V-oil 1404 (ISO 4113) calibration type fluid has been applied in the test bench [101]. The pump speed has been fixed at a constant value, i.e. $n = 1000$ rpm referring to 2000 rpm engine speed, for all the experimental tests. It should be noted that, the obtained research

(a) $p_{nom} = 1600$ bar, $ET = 180$ μs   (b) $p_{nom} = 1100$ bar, $ET = 800$ μs
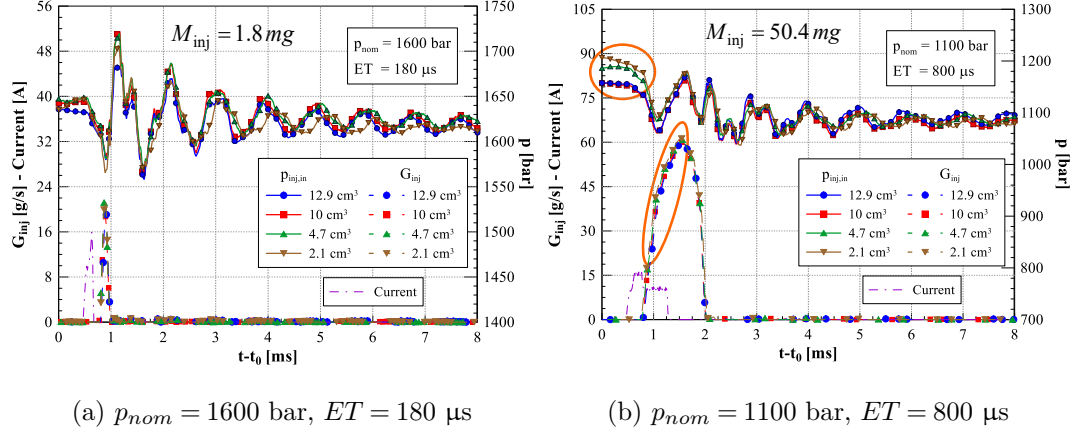
Figure 3.4: Comparison of the G_{inj} and the $p_{inj,in}$ between the CR systems with different rail volumes.

results are appropriate for the other different engine speeds since n does not cause any effect on the injection system performance.

3.3   Results and discussion

In Figure 3.4, two engine operating points $p_{nom} = 1600$ bar, $ET = 180$ μs and $p_{nom} = 1100$ bar, $ET = 800$ μs with single injection strategy have been considered for different rail volumes (V_{rail}) pertaining to the CR layout. The measured injector inlet pressure time histories ($p_{inj,in}$), the instantaneous injected mass flowrates (G_{inj}) and the electrical current signals have been collected and reported as an average value over 100 consecutive engine cycles under steady state working conditions. The pressure signal $p_{inj,in}$ which shows the pressure variation trend is known as a critical parameter in the high-pressure circuit. Before the current starts to increase (0 ms $< t - t_0 < 0.5$ ms, where t_0 stands for the reference time instant), the $p_{inj,in}$ pressure time histories remain almost constant and stable for different V_{rail} values which cause negligible effects to the incoming injection events. The occurrence of the possible influences acting on the $p_{inj,in}$ pressure is due to the residual pressure waves transmitted through the rail-to-injector pipe that are excited by the last injection cycle.

For a relatively small injected mass ($M_{inj} = 1.8$ mg) which is shown in Fig. 3.4a, when the rail volume V_{rail} varies, the $p_{inj,in}$ and the G_{inj} time histories are almost identical during the whole injection event that is 0 ms $< t - t_0 < 8$ ms.

It could be included that the V_{rail} value has negligible influence on the injection performance when the small injections are considered. With regard to a large injected mass ($M_{inj} = 50.4$ mg displayed in Fig. 3.4b), the initial phase of the $p_{inj,in}$ pressure traces, signed with a circle, have shown to be increased with the reduced accumulator size. This pressure difference fact leads to a more quickly needle lifting process during the start of the injection period pertaining to a smaller accumulator volume and as a consequence, a slightly bigger instantaneous injection flowrate is caused which is indicated as the circled region of G_{inj} in Fig. 3.4b. Finally, for the same electrical command to the injector, the fuel injected quantity has been altered. In Fig. 3.4b, referring to different values of V_{rail} , a depression wave originated from the start of the injection event begins to travel along the pipeline following the path from the injector to the rail. This pressure wave reaches $p_{inj,in}$ pressure sensor position at $t - t_0 \approx 0.8$ ms. Since there is a constraint area between the injector needle and the seat, part of the fuel travelling from the injector feeding pipe passage to the nozzle is not able to be drained through the nozzle orifices [102]. In this way, a compression wave is generated at $t - t_0 \approx 1$ ms. At the same time, the before-mentioned depression wave reaches the end of the rail and then reflects back as a compression wave propagating towards the injector nozzle side. The effective hydraulic injection is considered to be finished at $t - t_0 \approx 2$ ms when the needle reaches the end of stroke and causes the needle closure. The water hammer effect has been detected in the $p_{inj,in}$ pressure traces and a series of oscillations occurred afterwards is also presented.

By applying the mass conservation equation to the rail, the following equation is defined:

$$\frac{V_{acc}}{a^2} \cdot \frac{dp_{acc}}{dt} = G_{pump} - G_{inj} - G_{leak} \tag{3.1}$$

where V_{acc} stands for the accumulator volume (in this case it represents the rail volume), p_{acc} is defined as the mean pressure in the accumulator, a is the fluid speed of sound, and G_{pump}, G_{inj} and G_{leak} refer to the fuel pumped, injected and leakage mass flow-rates, respectively. By realizing the integration of Eq. (3.1) over an entire injection cycle (T_{inj}), one obtains:

$$\frac{V_{acc}}{a^2} \cdot \int_{t_0}^{t_0+T_{inj}} \frac{dp_{acc}}{dt} = M_{pump} - M_{inj} - M_{leak} \tag{3.2}$$

where t_0 is defined as the reference time instant. By considering a similar total amount of fuel mass $(M_{inj} + M_{leak})$ has been discharged from the injector for different values of V_{rail} and the pumped fuel M_{pump} is nearly identical, it could be concluded that $p_{inj,in}$ variation is inversely correlated to V_{acc}. In other words, $p_{inj,in}$ starting level is higher for a smaller V_{rail} and it is intentionally set by the control strategy of ECU in order to keep the time average value of the rail pressure remaining around the nominal value. Since the subsequent rail pressure drop due to the injection is larger for a reduced V_{rail}, the initial difference in $p_{inj,in}$ is said to be compensated by the injection event. It could also be seen from the plot shown in Fig. 3.4b that $p_{inj,in}$ pressure traces pertaining to different values of V_{acc} are basically coincident.

Same variables displayed in Fig. 3.4 have been analysed under another working point ($M_{inj} = 61.4$ mg) and shown in Fig. 3.5. The CF layout featuring $V_C = 10$ mm^3 and no additional orifices has been studied. With regard to the pressure signal $p_{inj,in}$, the initial value pertaining to the configuration of the CF system is located between the CR system with $V_{rail} = 12$ cm^3 and 2.1 cm^3. It is also true for the increasing phase of the injected flowrate as shown in Fig. 3.4. Therefore, the injection performance is strongly related to the accumulator volume size.

As far as the CR system is concerned, the free pressure waves generated due to the injection event behave differently when the rail volume is varied: the frequency of the free pressure waves tends to increase with the rail volume
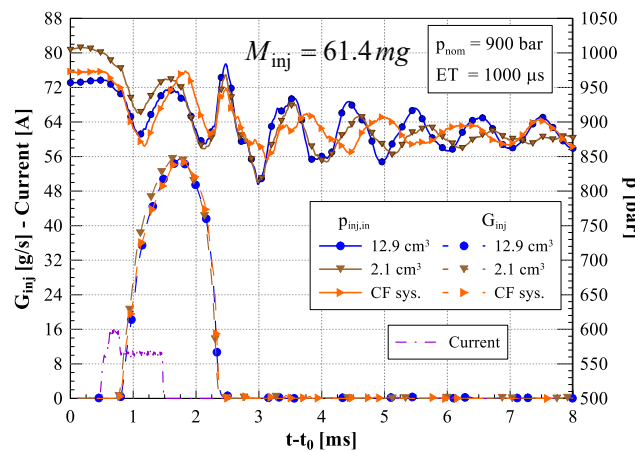
Figure 3.5: Comparison of the G_{inj} and the $p_{inj,in}$ under single injection strategy between the CR and the CF systems.

size. By considering the CF configuration, although it features a capacitance volume equals to $V_C = 10$ cm^3, the pressure wave natural frequency is shown to be almost 30% lower than those of the other rail conditions. The varied accumulator shape could lead to this change.

The injector characteristics plot regarding to the CR and the CF systems has been shown in Fig. 3.6. The two extreme values of V_{rail} in the CR layout and the CF system non equipped with the gauged orifices have been chosen for the comparison. The CR system featuring the smallest rail volume size, $V_{rail} = 2.1$ cm^3 plotted in dash line, characterizes a biggest slope of the $M_{inj} - ET$ curve and the injected mass difference between the two CR systems reaches up to 5.5 mg with a fixed *ET*. By changing from the CR layout ($V_{rail} = 12.9$ cm^3) to the CF one, the injector characteristics results to be similar. As it has been said, a chamber with volume of 10cm^3 is presented in the CF system and this volume is comparable with the one existed in the CR system. Therefore, it can be concluded that the injector characteristic slope tends to increase when the accumulator volume is reducing and it is independently from the accumulator shape. Moreover, the observed trends are also in accordance with the initial $p_{inj,in}$ pressure trace difference for varies sizes of the accumulator (cf. Fig. 3.4b)

As far as static leakage is concerned, it represents the amount of fuel expelled from the injector back to the tank recirculation passage when the pilot valve keeps in a closed situation during one entire engine cycle (for the current engine
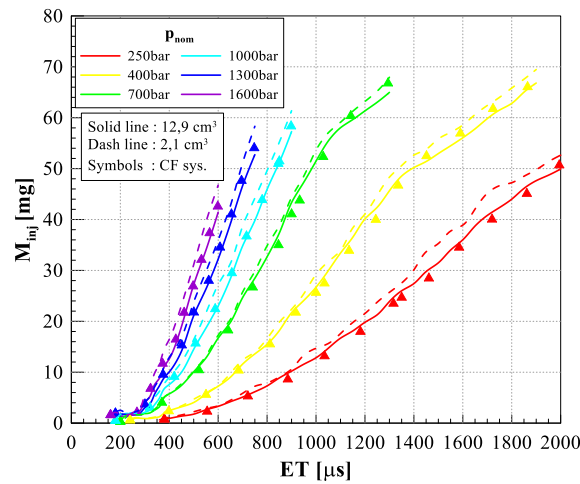
Figure 3.6: Injector characteristics comparison between the CR ($V_{rail} = 12.9$ cm^3 and 2.1 cm^3) and the CF (without gauged orifices) systems.

speed, 60 ms). The measurement of the static leakage has been realized under steady-state working conditions by fixing a certain p_{nom} level and forcing the hydraulic system running without performing any injections. The static leakage per engine cycle of the CR system has been measured and shown in the Fig. 3.7a. The static leakage for $p_{nom} > 1200$ bar group is shown to decrease as the rail volume reduces. From the fluid dynamcis point of view, the static leakage could be achieved by performing a stationary volumetric flowrate based pn Hagen-Pouseille equation:

$$Q_{leak} = K\frac{\bar{p}}{\bar{\mu}} \tag{3.3}$$

where K is a geometrical parameter which describes the injector pilot valve layout and other existences of the clearance passages. $\bar{\mu}$ stands for the fuel dynamic viscosity as a function of the time averaged pressure $\bar{p}$ and temperature $\bar{T}$ values inside the injector. The ECU control strategy forces the pressure $\bar{p}$ to be constant under the same p_{nom} pressure levels when V_{rail} varies. With regard to the temperature inside the injector, namely $T_{inj,in}$, it has been measured at the position closed to the injector inlet along the high-pressure pipeline instead of the exact inner part of injector since it is virtually impossible to be done. In Fig. 3.7b, $T_{inj,in}$ tendency with respect to different nominal pressure levels has been reported for different volume sizes. The trend of $T_{inj,in}$ has shown to be similar with respect to that of the static leakage and it can be supposed that the dependence of $\bar{T}$ on the rail volume size is more evident than that shown by $T_{inj,in}$. By considering that $\bar{\mu}$ is sensitive to the temperature change, the difference occurred for the static leakage could be due to thermal effect.

By subtracting the static leakage from the total leakage, the amount of the fuel flowing through the pilot valve during an injection event within one engine cycle, namely dynamic leakage, has been evaluated. This quantity pertaining to all the volume sizes of the CR system has been recorded and represented in Fig. 3.8. An increasing ET results in a longer opening duration of the pilot valve and this leads to a larger dynamic leakage. By considering the pressure level affect, the dynamic leakage rises when the nominal pressure is higher. However, no evident change can be observed when the V_{rail} changes.

The injected mass coefficient of variation σ is considered as an important parameter for the engine application and an injection is required to meet a coefficient lower than 10% standard [103]. In the present case, the CR system

injected mass coefficient of variation has been measured by HDA with 100 engine cycles and the result has been shown in Fig. 3.9. It can be discovered that, except for some working conditions under $p_{nom} = 250$ bar and small ETs, the other remaining points satisfy the basic requirement. Basically, the high coefficients of the injected mass variation happen at either low p_{nom} or ET. Moreover, σ tends to drop dramatically with an increasing ET.

By considering the entire working zone shown in Fig. 3.9, the smaller rail volume worsened the dispersion coefficient performance. For the aim of

(a) Static leakage comparison

(b) Injector inlet pipe temperature comparison
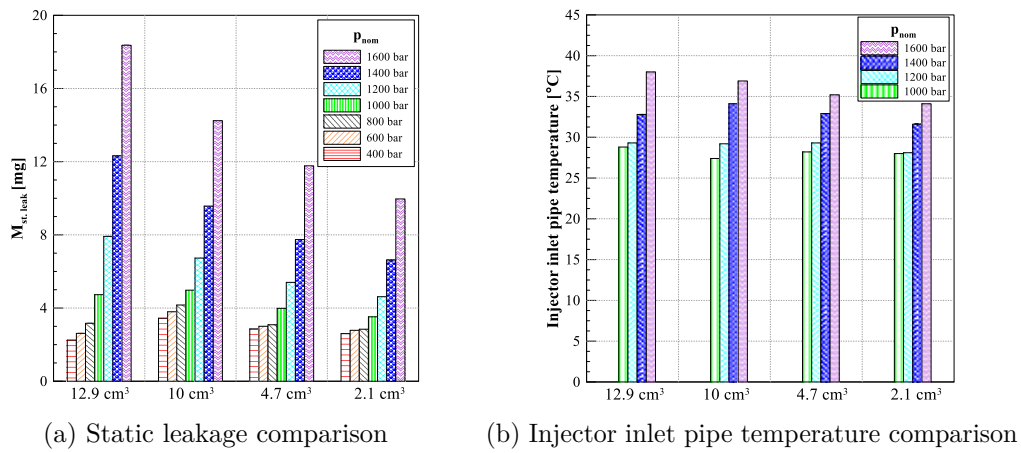
Figure 3.7: Static leakage and injector inlet pipe temperature comparison among different rail sizes of the CR system.
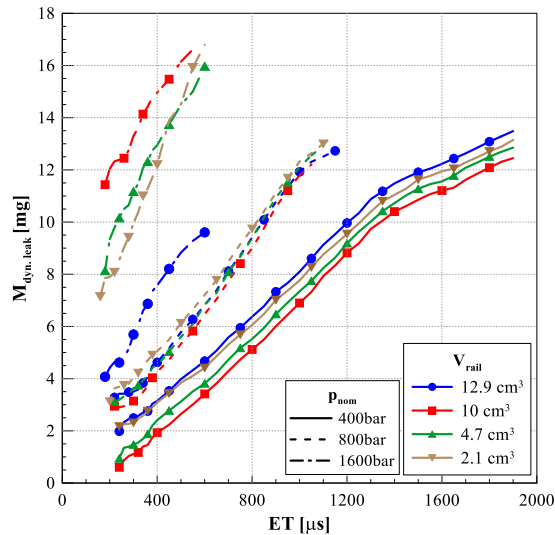
Figure 3.8: Dynamic leakage comparison among different rail sizes of the CR system.

simplicity, the dispersion pertaining to $V_{rail} = 10$ cm^3 and 4.7 cm^3, which also follow the trend, have been omitted in the figure.

The duration between the start of energizing current signal and the beginning of the effective injection,namely the nozzle opening delay (NOD), has been evaluated and reported in Fig. 3.10. The injector dynamic response has been defined as a short NOD. In figures 3.11a and 3.11b, the performances of NOD parameter pertaining to the CR systems with two rail volume sizes $V_{rail} = 12.9$ cm^3 (solid line) and $V_{rail} = 2.1$ cm^3(dashed line) have been reported. For a fixed p_{nom}, a linear interpolation has been applied to the NOD data for each configuration.

(a) $V_{rail} = 12.9$ cm^3 (b) $V_{rail} = 2.1$ cm^3
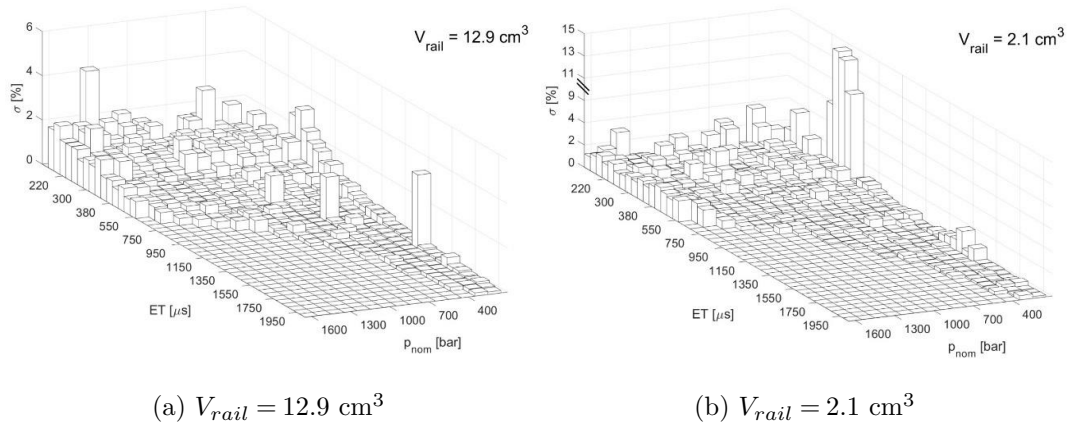
Figure 3.9: Injected mass coefficient of variation comparison between the CR systems with different V_{rail} and the CF systems.

Figure 3.10: NOD and NCD.

(a) $V_{rail} = 12.9$ cm^3 (b) $V_{rail} = 2.1$ cm^3
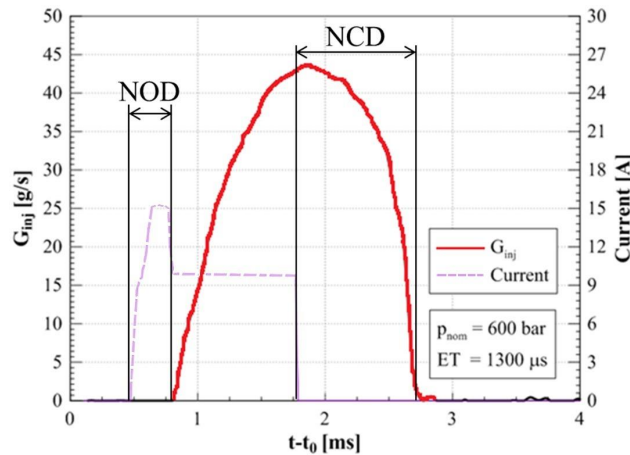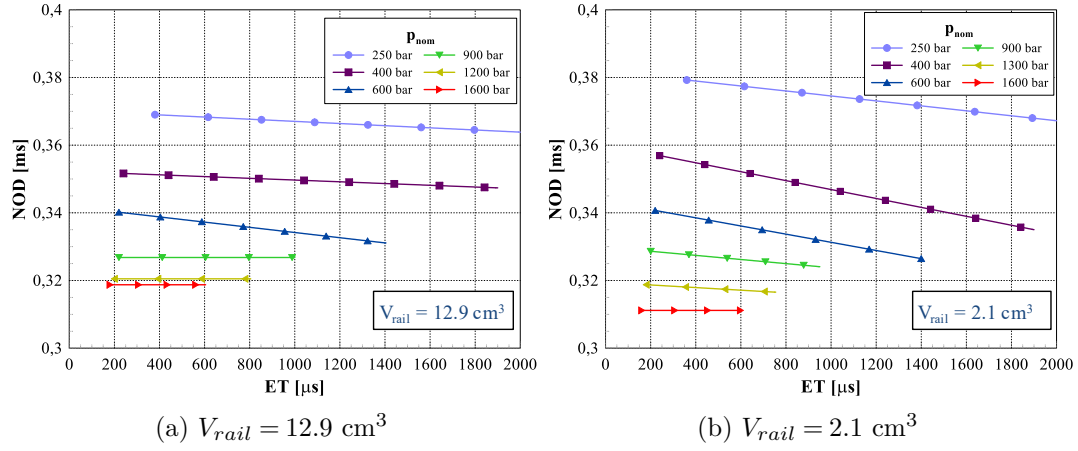
Figure 3.11: *NOD* performance of the CR systems for different rail volumes.

In general, *NOD* starts to be smaller with an increasing p_{nom} since a larger dynamic leakage flowrates happened under higher pressure level and the time to empty the control chamber will be reduced [20].

Another parameter that is usually mentioned together with nozzle opening delay is needle closure delay, namely *NCD*, as shown in Fig. 3.10 . It refers to the duration between the shut off of the electric command from ECU and the closure of the nozzle. The measured *NCD* values have been reported in Fig 3.12 for different pressure values with two rail volume sizes. It could be seen that, with a larger *ET*, *NCD* tends to increase and a greater slope curve is presented for a higher nominal pressure level. When *ET* is large enough for the needle reaching the stroke end, *NCD* will be constrained and remain constant even *ET* continues to increase[20]. As far as a small nominal pressure level p_{nom} is concerned, the needle closure force is smaller and it leads to a larger *NCD* as confirmed in Fig 3.12.

The experimental tests have also been made under pilot-main injections strategy. In Fig. 3.13, same variables as Fig. 3.4 have been conducted under two engine working conditions $p_{nom} = 1000$ bar, $DT = 400$ μs, $V_{pil} = 2$ cm^3, $V_{main} = 50$ cm^3 and $p_{nom} = 1000$ bar, $DT = 1200$ μs, $V_{pil} = 2$ cm^3, $V_{main} = 50$ cm^3. The *ETs* have been set under the dwell time *DT* (the time length between two electrical currents) equals to 3000 μs when the second injection is not affected by the pressure waves excited by the first injection. In order to reach the same injected quantity for different V_{rail} values, the predefined *ETs*

have been fixed when DT changes. In the Fig. 3.13, only one current signal of one V_{rail} has been plotted for the simplicity.

As far as double injection strategy (pilot and main injections) is concerned, the small injected quantity pertaining to pilot injection V_{pil} causes the depression wave immediately after the generated compression wave. The water hammer effect due to the needle travels back to the seat then appears at the end of pilot injection which induces the pressure waves travelling along the rail-to-injector pipe. The free oscillations occurred in pressure signal $p_{inj,in}$ feature an amplitude up to 200 bar and frequency around 1 kHz.

(a) $V_{rail} = 12.9$ cm^3 (b) $V_{rail} = 2.1$ cm^3
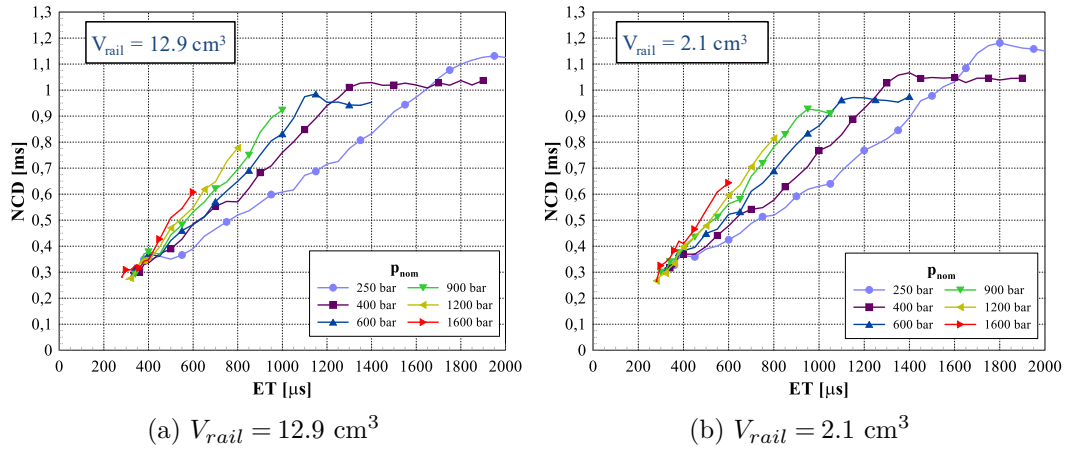
Figure 3.12: *NCD* performance of the CR systems for different rail volumes.
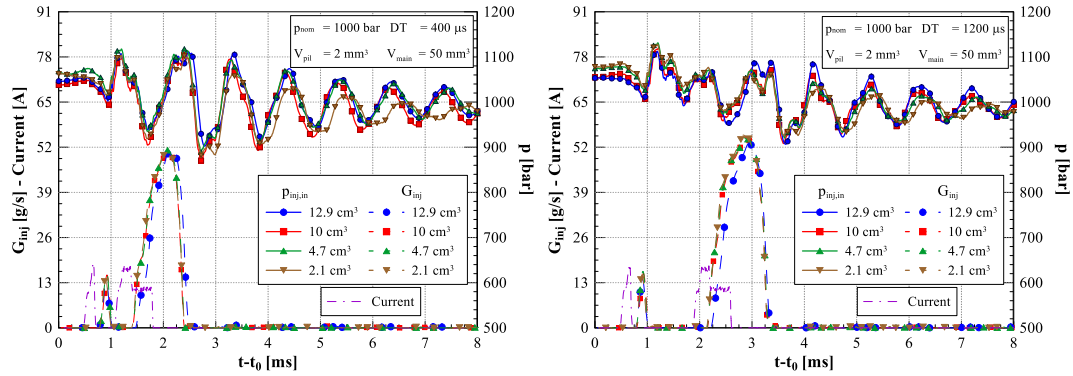
(a) $p_{nom} = 1000$ bar, $V_{pil} = 2$ mm^3, $V_{main} = 50$ mm^3 and $DT = 400$ μs   (b) $p_{nom} = 1000$ bar, $V_{pil} = 2$ mm^3, $V_{main} = 50$ mm^3 and $DT = 1200$ μs

Figure 3.13: Comparison of the G_{inj} and the $p_{inj,in}$ under pilot-main injection strategy between the CR systems with various rail volumes.

Figure 3.13a and Fig. 3.13b report the injection performance under the same V_{rail} group, the target injected volumes and the ETs but with different DT. In Figure 3.13a, the main injection starts with the presence of a depression wave in the nozzle, while in Figure 3.13b, the main injection begins at the time instant when a compression wave has arrived at the nozzle. The above two examples show that the pressure waves triggered inside the injector play a dominant effect on the main injection by means of the needle lifts, and in turn, it affects the effective hydraulic injection duration. Indeed, the effective injection duration pertaining to the case shown in Fig. 3.13a is slightly shorter with respect to the situation in Fig. 3.13b. As a result, the injected flow rate and the corresponding injected quantity are bigger for the cases in Fig. 3.13b.

The pilot and main injected volumes have been compared with respect to different DT sweeps from 100 µs to 2000 µs and the results are shown in Fig.3.14 where the lower curves refer to the pilot injected volume and the upper ones are main injected volume. The injection fusion between the pilot and main injection occurs when DT reached below a certain threshold. Under the fusion situation, the separate pilot and main injected volume could not be detected but evaluated as the overall quantity. As a result, the sudden rise marked as a circle zone is occurred in the main injected volume while the corresponding pilot injection volume data have been removed in Fig.3.14. With regard to a high DT when the injection fusion is not happened, the pilot injected volume ($V_{inj,pil}$) remains almost unchanged, while the main injected volume ($V_{inj,main}$) varies with respect to the DT change and the variation has been evaluated based on the percentage variation and defined as follows:

$$\sigma = \left| \frac{V_{main}\left(DT\right) - \bar{V}_{main}}{\bar{V}_{main}} \right| \tag{3.4}$$

where $V_{main}(DT)$ refers to the main injected volume under a certain DT value and $\bar{V}_{main}$ represents the average main injected volume with respect to DT. Based on σ reported in Fig. 3.14, $V_{inj,main}$ variation shows up in the values of σ which could reach 20% for small DTs. By considering the frequency aspect, the $V_{inj,main}$ oscillation with respect to DT features a frequency nearly 1 kHz which is almost identical to the one regarding to the pressure waves shown in Fig. 3.13. It could be concluded that the pressure waves initiated by
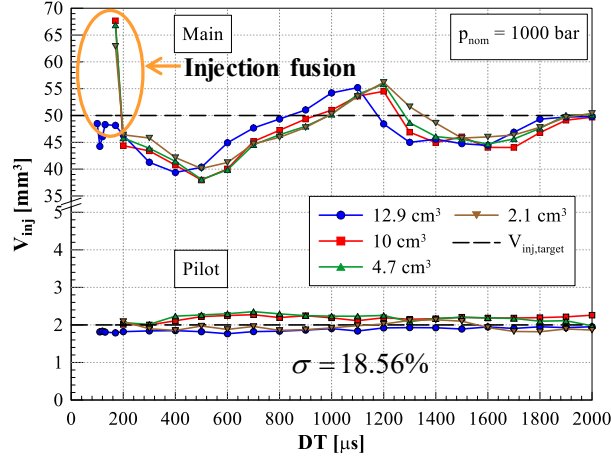
Figure 3.14: Injected volumes pertaining to pilot injection and main injection between the CR systems with different rail volumes ($p_{nom} = 1000$ bar).
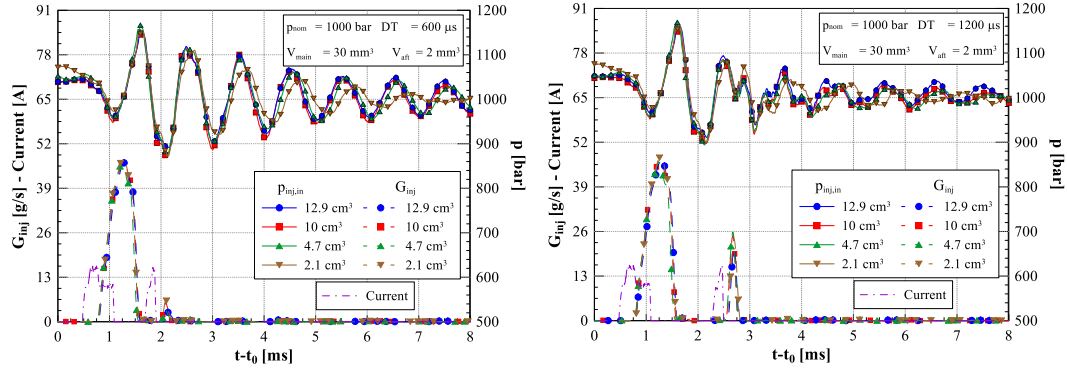
(a) $p_{nom} = 1000$ bar, $V_{main} = 30$ mm^3, $V_{aft} = 2$ mm^3 and $DT = 600$ μs

(b) $p_{nom} = 1000$ bar, $V_{main} = 30$ mm^3, $V_{aft} = 2$ mm^3 and $DT = 1200$ μs

Figure 3.15: Comparison of the G_{inj} and the $p_{inj,in}$ under main-after injection strategy between the CR systems with various rail volumes.

the pilot injection and passing inside the rail-to-injector pipe have influenced significantly on the main injected quantity [104].

With regard to the double injection strategy, the main-after injections have also been performed and analysed. As explained for the pilot-main injections, for all the V_{rail} values, the main-after injections strategy features fixed ETs which are defined under $DT = 3000$ μs for the aim of achieving the same injected volumes. In Fig. 3.15, the injector inlet pressure time histories, the instantaneous injected flowrates and the electrical current signal (the one pertaining to $V_{rail} = 12.9$ cm^3 has been selected as an example) have been

shown under 1000 bar of nominal pressure level. The target values for the main and after injections are 30 mm^3 and 2 mm^3, respectively. Fig. 3.15a makes reference to the situation with *DT* equals to 600 μs while Fig. 3.15b features DT value being 1000 μs. The quantity of after injection depends closely on the dynamic pressure waves excited by the main injection. To be specific, for the case shown in Fig. 3.15a, the water hammer effect happens when the main injection has finished and the needle closure excites a compression wave. As soon as the after injection begins, the compression wave has been reflected back as an expansion wave towards to the nozzle. As a result, the fuel injected during the after injection event tends to decrease compared with the target value. On the contrary, with regard to the example displayed in Fig. 3.15b, the occurrence of a compression pressure wave during the after injection leads to a bigger injected volume. Fig. 3.16 reports the injected volume variation pertaining to main (upper curves)and to after injection (lower curves) with respect to *DT* sweep. A visible after injection volume oscillation has been detected as a result of the pressure waves triggered by the main injection event. The frequency of the observed injected quantity oscillation is the same as that of the free pressure waves that equals to 1 kHz.

With regard to different rail sizes, Figure 3.17 presents the rail pressure signals and the injected flowrates pertaining to a pilot-main injection (cf. Fig. 3.17a) and to a main-after injection (cf. Fig. 3.17b). As has been explained for the injector inlet pressure $p_{inj,in}$, for a fixed injected volume, a smaller rail
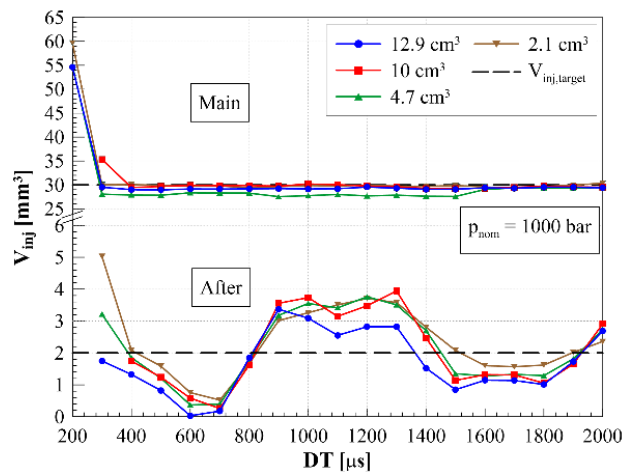
Figure 3.16: Injected volumes pertaining to main injection and after injection between the CR systems with different rail volumes ($p_{nom} = 1000$ bar).
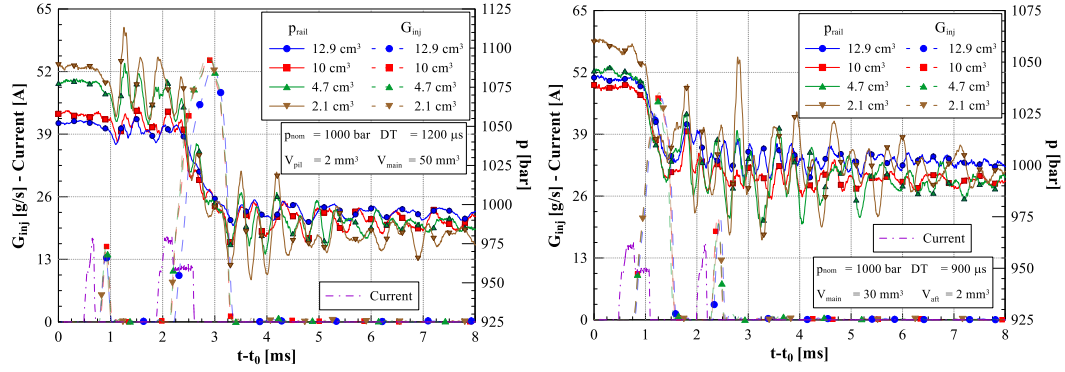
(a) $p_{nom} = 1000$, $V_{pil} = 2$ mm^3,
$V_{main} = 50$ mm^3 and $DT = 1200$ µs

(b) $p_{nom} = 1000$ bar, $V_{main} = 30$ mm^3,
$V_{aft} = 2$ mm^3 and $DT = 900$ µs

Figure 3.17: Comparison of the G_{inj} and the p_{rail} under main-after injection strategy between the CR systems with various rail volumes.

volume leads to a more evident rail pressure drop during an injection event. By reducing the rail size, the initial pressure level before the starting of injection tends to increase in order to keep the same average nominal pressure level p_{nom}. At the end of the injection event, the water hammer generated by the needle closure results in a augmented pressure level as the rail volume reduces. It should be noted that the rail pressure dynamic behaviour differences does not influence the injection system global performance.

With regard to the CF system, the main injected volume variations with respect to DT have been evaluated and presented in Figure 3.18. The working points have been selected as the same ones presented in Fig. 3.14. It could be concluded that for the CF system, by installing the gauged orifices at the output side of the pump, the pressure waves are able to be damped and the amplitude of the $V_{inj,main}$ fluctuations is attenuated. A smaller diameter of the orifice d_{or} shows a more effective damping effect on the $V_{inj,main}$ oscillation amplitude [105]. Moreover, the increase in the passing damping prolongs the free pressure waves period and also the oscillations displayed in Fig. 3.18. The damping effect brought by the gauged orifices investigations has been reported in a previous work and it has been discovered that a reduction of the injected volume could reach up to 8 %. At present, the injected flowrates under the presence and the absence of the gauged orifices are not shown for brevity [100]. This passive damping method could also be applied to the standard CR system.
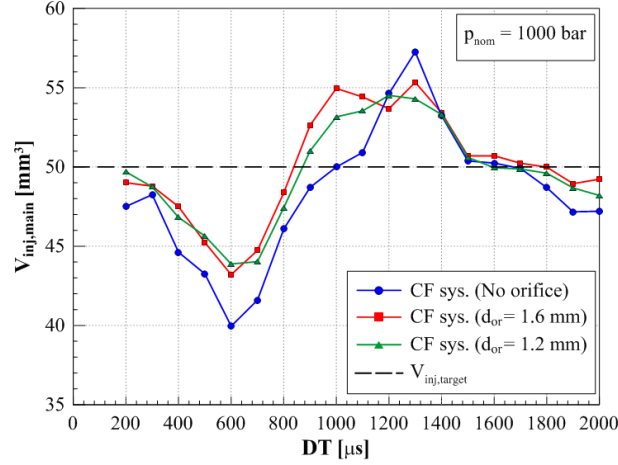
Figure 3.18: Injected volumes pertaining to main injection versus *DT* between the CF systems ($p_{nom} = 1000$ bar).

3.4   1D injection system model

A 1D numerical diagnostic model has been designed and validated for the aim of studying the effect of different V_{rail} on the internal dynamics performance of the CR layout [106]. In Fig. 3.19, the schematic drawing of the 1D injection system model has been shown and the validation process is achieved by applying the collected experimental data [106]. With regard to the displayed model, the main characteristics pertaining to the mechanical modules, the high-pressure hydraulic circuit and the electromagnetic have been taken into account. The circuit is established as a 0D chambers network and is connected through 1D pipes by applying the Lax-Wendroff scheme as the solution method. The boundary conditions have been set as the rail pressure trace and the electrical current signal. An isothermal process regarding to thermodynamics has been considered and the energy equation is then transformed into a state equation. Therefore, the governing equations with regard to the pipe model are conducted by the generalized Euler partial differential equations:

$$\frac{\partial}{\partial t}\begin{bmatrix} \rho \\ \rho u \end{bmatrix} + \frac{\partial}{\partial x}\begin{bmatrix} \rho u \\ \rho u^2 + p \end{bmatrix} = \begin{bmatrix} 0 \\ -4\tau_w/D \end{bmatrix} \tag{3.5}$$

where x represents the spatial coordinate, t stands for the time, ρ, u, and p stand for the density, the velocity and the pressure averaged over the cross-section pipe, respectively. τ_w is the wall shear stress, consisting of a steady state
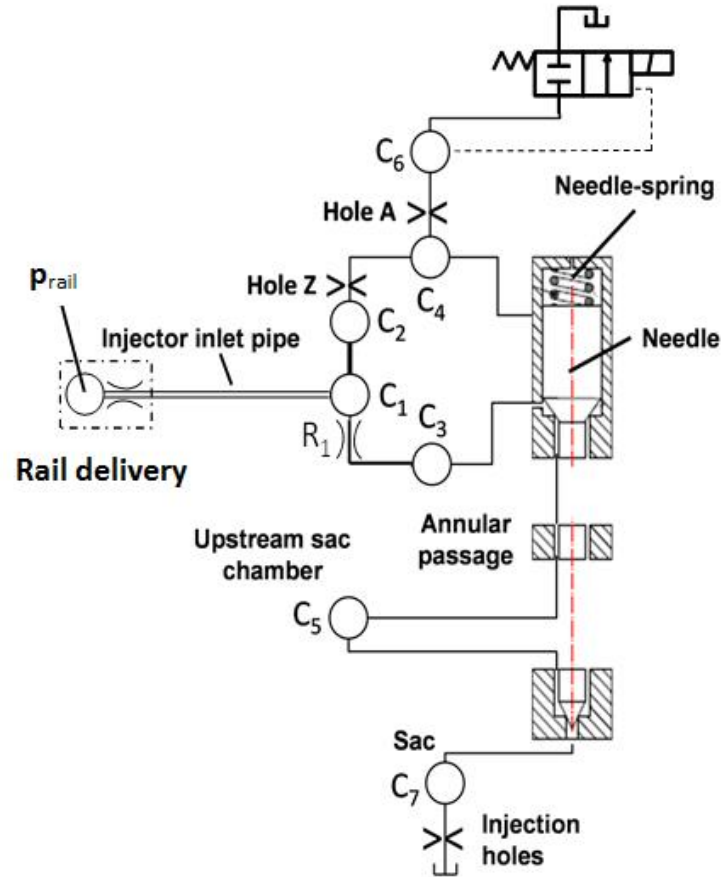
Figure 3.19: The sketch of the CR injection system 1D numerical model.

term and a frequency-dependent term calculated based on the procedure shown in [107]. The moving components are possessed by Newton laws of motion in the ordinary differential form. Hydraulic, mechanical, and electromagnetic phenomena result in the influential forces.

The model validation process has been realized by comparing the simulated injection flowrate and injector inlet pressure time histories with the corresponding experimental collected data. Fig. 3.20 represents an example of the model validation pertaining to a pilot-main double injection strategy ($p_{nom} = 1200$ bar, $V_{pil} = 2$ mm^3, $V_{main} = 30$ mm^3 and $DT = 400$ μs) for two different rail sizes, $V_{rail} = 12.9$ cm^3 (cf. Fig. 3.20a) and the $V_{rail} = 2.1$ cm^3 (cf. Fig. 3.20b), respectively. The injector inlet pressure time history has been plot in continuous line and the injected flowrate in dashed line. It can be concluded that the 1D diagnostic model has been validated since the numerical simulated traces

(a) $V_{rail} = 12.9$ cm^3 (b) $V_{rail} = 2.1$ cm^3
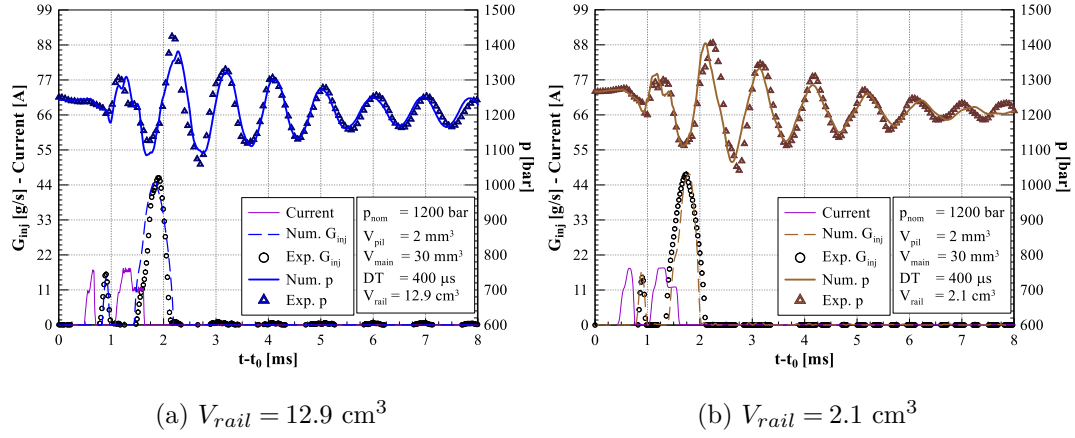
Figure 3.20: Experimental data and numerical simulation results comparison: $p_{nom} = 1200$ bar, $V_{pil} = 2$ mm^3, $V_{main} = 30$ mm^3 and $DT = 400$ μs.

pertaining to both the pressure and the injected flowrate are almost overlapped with the experimental data (the pressure data with triangle symbols and the flowrate with circles).

A single injection under $p_{nom} = 900$ bar and $ET = 1000$ μs has been concerned in Fig. 3.21. The needle lift and the needle velocity pertaining to
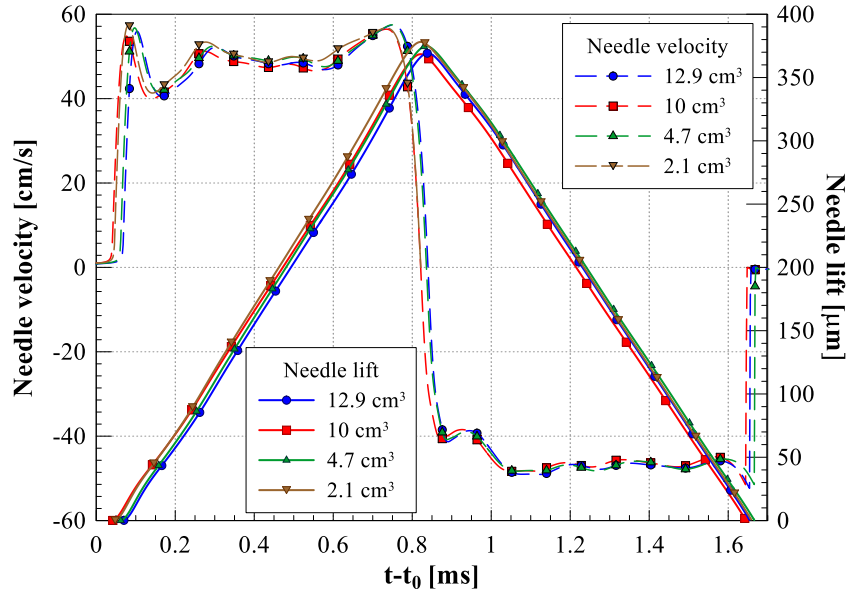
Figure 3.21: Needle velocity and needle lift pertaining to a single injection ($p_{nom} = 900$ bar and $ET = 1000$ μs).

different rail sizes have been plotted and analyzed. Based on the performance shown in the figure, it has been confirmed that the needle lift value and the needle opening velocity increases with reducing the rail volume size. These two factors characterize the injection duration and with a smaller accumulator volume size at fixed ET and p_{nom}, the augment of these two parameters leads to a bigger injected quantity due to a longer injection duration. The reason of the increasing value of the needle lift and of its velocity for a smaller rail size is the higher mean pressure formed in the hydraulic circuit at the start of the injection event. It accelerates the control chamber discharging process and generates a faster injector response to the electrical signal [21]. With regard to a pilot-main injection strategy where p_{nom}, DT and injected volumes are fixed, the main injection performances between different rail volume sizes are varied. Based on the numerical analysis reported in Fig. 3.22, it can be observed that although the injection duration is the same when the rail size is reduced, the needle lift peak value slightly increases and the main injection event begins at a higher delivery chamber inside pressure time instant. Another reason is that the current signals are not the same with the same injection schedule pertaining to different accumulator size. Indeed, the same injection quantities have been realized by modifying ET_{pil} and ET_{main} when the rail configurations have been changed (selected at $DT = 3000$ μs). During the experimental tests, it has been discovered that when the rail size is reduced, a smaller ET_{pil} is needed to reach the defined pilot injected quantity. This implies that with a fixed DT, the current signal with regard to the main injection is brought forward compared with the one of to the biggest rail size (where ET_{pil} is bigger). In this case, the advanced beginning of the main injection for a smaller accumulator volume will not meet the depression wave coming toward the delivery chamber.
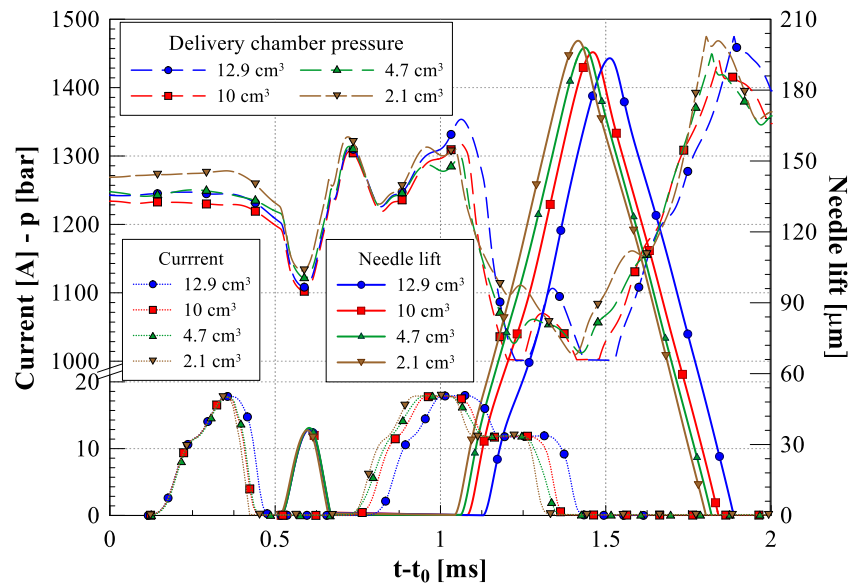
Figure 3.22: Delivery chamber pressure and needle lift under a pilot-main injection strategy ($p_{nom} = 900$ bar, $V_{pil} = 2$ mm^3, $V_{main} = 30$ mm^3, $DT = 400$ μs).

Chapter 4

Closed-loop control strategy of injected mass on the basis of time-frequency analysis

4.1 Experimental setup

The experimental campaign has been carried out on a Moehwald-Bosch hydraulic test bench located in the ICE laboratory at the Politecnico di Torino. The test bench is able to offer 35 kW power, 100 Nm maximum torque and 6100 rpm maximum speed. A state-of-the-art Bosch fuel injection system has been tested and Fig. 4.1 is the experimental layout of the system. A double-effect single piston, high-pressure pump with a total displacement of 430 mm^3/rev has been installed in the system. The injectors are Bosch CR 2.18 solenoid-actuated which features the presence of a pressure balanced pilot-valve as shown in Fig. 4.2. The test bench is equipped with a Zeuch method-based flowmeter, named HDA from Moehwald-Bosch, for the measurement of the injection rate and the injected quantity which refers to the analyzed injector [108]. The electrical current is collected by means of a current clamp. A piezoresistive pressure transducer is mounted along the rail-to-injector pipe in order to capture the injector inlet pressure time history p_{inj} and it has been transmitted to PXI (from National Instruments) with 500 kHz sampling frequency.

Fig. 4.3 shows a hydraulic circuit diagram of the injection system. The working principle of the injection system is to deliver the high-pressure fuel
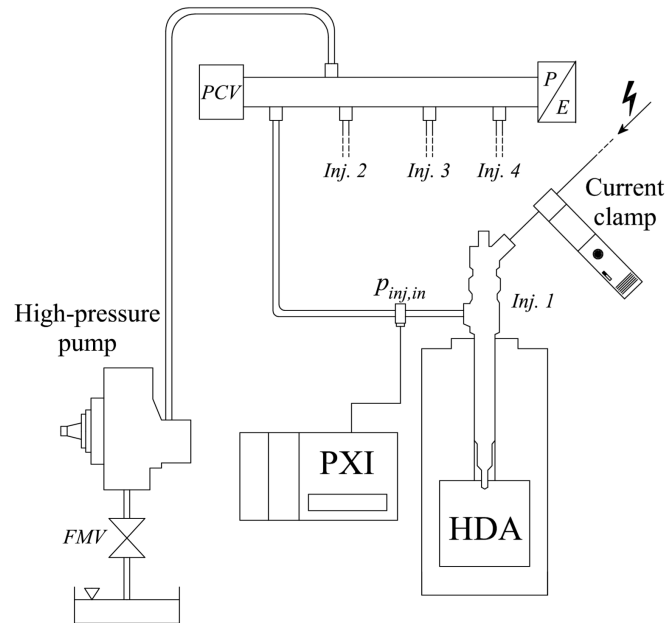
Figure 4.1: The schematic drawing of the injection system.

from the pump to the rail and then the fuel enters into the injectors through the connected pipe between rail and injector. Part of the fuel arrives in the control chamber (volume V_{cc}) passing across the Z hole, and the rest reaches
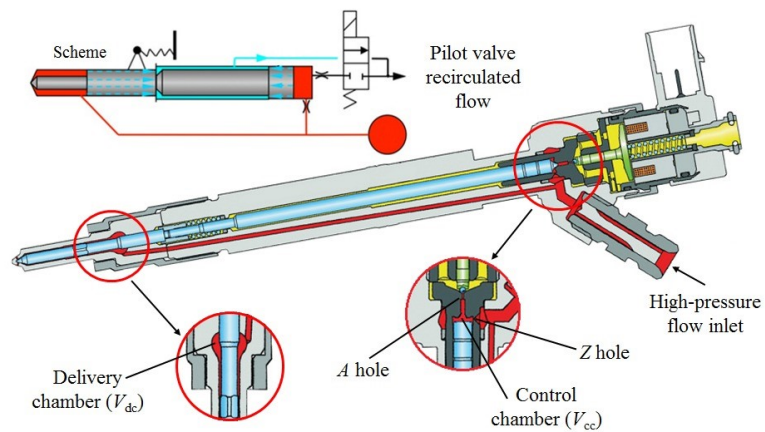
Figure 4.2: The tested CRI 2.18 solenoid injector.
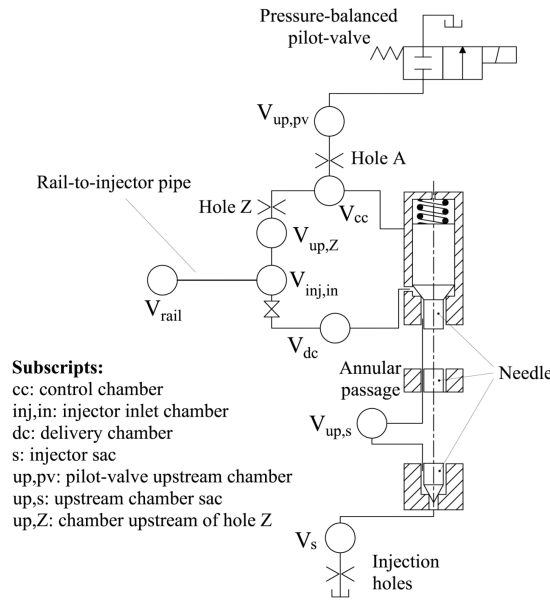
Figure 4.3: The sketch of the hydraulic circuit pertaining to the injection system.

the delivery chamber (volume V_{dc}). The solenoid is engaged when the electrical current is provided by the electronic fuel injection system and the pilot valve is opened with discharging the control chamber. In this way the fuel pressure in the control volume reduces and results an imbalance force on the needle. The needle starts to move upwards, and the nozzle opens to inject the fuel through the injection holes. When the electrical current is shut down by the ECU, the control chamber pressure rises due to the closure of the pilot valve. As a result, the needle begins the downstroke and when it reaches the initial position, the nozzle is again closed and the injection phase finishes. Shell V-Oil 1404 (ISO 4113) calibration fluid has been selected for the current research due to the similar physical properties as the diesel oil over an appropriate pressure and temperature range. Experimental tests have been conducted under single injections by setting nominal rail pressure p_{nom} in the range of 500-1700 bar and energizing time ET over the 0.35-1.1 ms range. Two different oil temperature values have been selected with $T_{tank} = 40$ ℃ or 68 ℃ measured at the fuel tank. Since the pump speed does not introduce any significant change on the CR performance, for the present work, the pump speed is fixed at 2000 rpm for all the tests. The corresponding engine speed is 2000 rpm by applying the 1:1 pump-to-engine speed ratio.

4.2 TFA-based technique

4.2.1 Time-frequency analysis

The time-frequency analysis allows to obtain the information of the studied transient signal $f(t)$ in both time and frequency domain. The proposed injected mass closed-loop control strategy in the present paper is based on the detection of time instants of the nozzle opening and closure events. The fast Fourier transform (FFT) has been selected and applied to each short-time duration while overlapping and consecutive calculations have been done to the signal. The transient signal is assumed to be stable within each time interval and the obtained FFT result corresponds to the mean instant of the time interval.

By processing the signal, a window function $h(t-\tau)$ needs to be multiplied to the signal $f(t)$. This window function contains unit energy and equals to non-zero value only around the time instant τ. The short-time Fourier transform of the signal $f(t)$ is then defined in the following equation:

$$F(\nu,\tau) = \int_{-\infty}^{+\infty} f(t) \cdot h(t-\tau) e^{-j2\pi\nu t} dt \tag{4.1}$$

As it has been explained, the chosen window function does not alter the energy, the energy density spectrum P_f of the signal is supposed to be the square of the short-time Fourier transform function:

$$P_f(\nu,t) = |F(\nu,t)|^2 \tag{4.2}$$

The energy, named as E_f is then evaluated by integrating P_f along time and frequency domain:

$$E_f = \int_{-\infty}^{+\infty} \int_{-\infty}^{+\infty} P_f(\nu,t) \, dt \, d\nu \tag{4.3}$$

In order to compute the mean instantaneous frequency (MIF), probability density function is applied to the energy density spectrum P_f as follows:

$$\bar{\nu}(t) = \frac{1}{\int_{-\infty}^{+\infty} P_f(\nu,t) \, d\nu} \int_{-\infty}^{+\infty} \nu \cdot P_f(\nu,t) \, d\nu \tag{4.4}$$

The calculated MIF is then used as the most representative frequency of the signal at one time instant and applied to represent the variation of the signal.

4.2.2   Injector characteristics

The injected mass measured by the HDA flowmeter as an average value of 100 consecutive engine cycles has been collected and then plotted in Fig. 4.4 under different working conditions. Under different p_{nom} and ET values, two temperature values have been set regarding to the fuel temperature in the tank with 40 ℃ represented by circle symbols and dashed lines, 68 ℃ with square symbols and continuous lines as shown in the Fig. 4.4. 40 ℃ value has been chosen as the common reference temperature for the hydraulic tests applied by diesel fuel injection system suppliers. Due to the safety reasons, the maximum temperature that could be reached for the current test bench is set to be 68 ℃. By applying a third-order polynomial function, the M_{inj} values are fitted to ET curves under different p_{nom} and T_{tank} conditions. The speed and density of the fuel entering out of the nozzle could be simulated as a function of p_{nom} and T_{tank}. With regard to the restricted area at the nozzle, it is considered as a quadratic function of the needle lift. Since the needle lift curve is shown to be a triangular shape under the ballistic injection condition, the maximum needle lift increase proportionally with ET. In this way, under fixed p_{nom} and T_{tank}, the mean injected flow-rate is considered as a quadratic polynomial function of ET and the resulted injected mass as a cubic function of ET. The mean injected flow-rate, namely ($\bar{G}_{inj}$), has been plotted in Fig.4.5 versus ET and three nominal pressures under $T_{tank} = 40$ ℃. Based on the polynomial coefficients displayed in the figure, it could be concluded that with respect to the linear part, the contribution of the second order term is not negligible. Moreover, the obtained interpolating curves through quadratic polynomials function correlates well with the measured experimental data.

By considering the thermal regime effect, the injected mass tends to increase with higher T_{tank} at fixed p_{nom} and ET working condition. This thermal effect behaves more evident for a lower rail pressure, which means, the difference between the injected mass at different fuel temperatures is higher when the rail pressure is lower. In Figs. 4.6a and 4.6b, the mass flow-rate G_{inj} under different ET sweeps have been plotted for two nominal pressure levels p_{nom}=

800 bar and p_{nom}= 1600 bar, respectively. The above mentioned thermal effect
has been studied by comparing the injected mass flow-rate G_{inj} under T_{tank}=
40 ℃ and 68 ℃. As can be inferred, the injected flow rate pattern is more
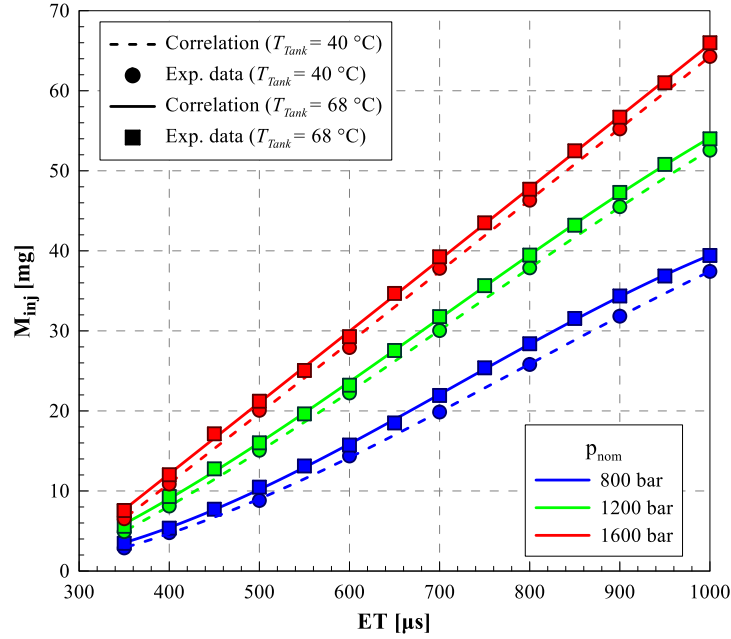
Figure 4.4: Injector characteristics under various p_{nom} and T_{tank}.
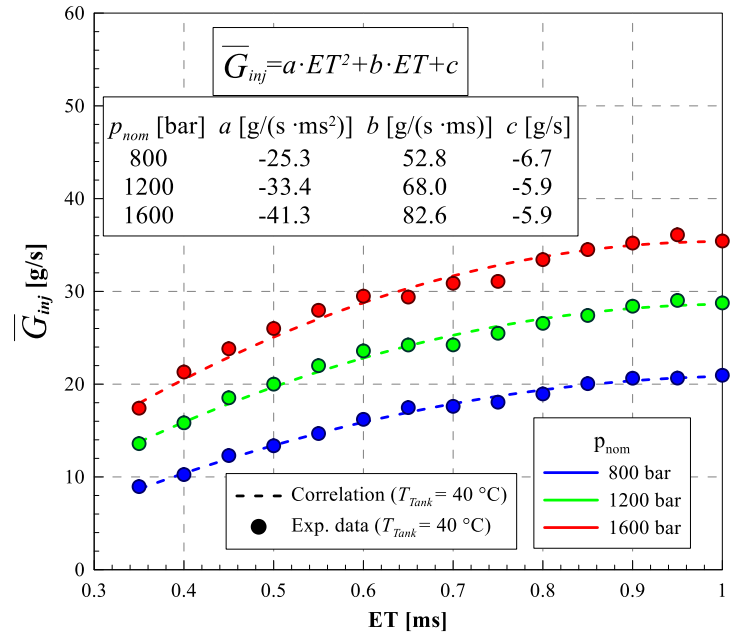
Figure 4.5: The main injected flowrate as a function of *ET* for various p_{nom} levels.

restricted by the needle seat passage at $p_{nom} = 800$ bar than at $p_{nom}= 1600$ bar. In Fig. 4.6a, a higher needle lift peak value is occurred for a longer ET and this results in a larger injected flow-rate peak value. However, this phenomenon doesn't appear in Fig. 4.6b where a higher nominal rail pressure is set. It could be explained that for ET larger than 0.45 ms, the maximum flow-rate is no more controlled by the needle lift peak value but by the nozzle injection holes. In this way, G_{max} remains the same by increasing ET when ET exceeds 0.45 ms. The example shown in Figs. 4.6a and 4.6b implies a more significant influence of the needle lift curve acting on the injected flow-rate pattern for a lower rail pressure value. With an increasing temperature, the fuel viscosity tends to decrease [109] as well as the friction stresses forcing on the needle [110]. This leads to a greater thermal effect impact on the injected mass at $p_{nom}= 800$ bar with respect to that at $p_{nom}= 1600$ bar. By comparing the injector dynamics behaviour under different T_{tank} values, the change of the fuel temperature influences predominantly the friction force acting on the needle which has also been proved in the literature [111].

The difference in the injected mass between the two selected fuel temperatures could reach 3mg ($M_{inj} \approx 25mg$ for $T_{tank} = 40$ ℃, $M_{inj} \approx 28mg$ for $T_{tank} = 68$ ℃) under $p_{nom} = 800$ bar and $ET = 800$ μs based on the data reported in Fig. 4.4. Moreover, it should be noted that compared with the temperature variation collected at the fuel tank of the hydraulic test bench, a higher temperature increase is supposed to be reached for the injection system. The procedure to determine the thermal regimes inside the injector nozzle under working requires a complex and accurate model [112]: for each 100 bar of pump compression, the injector inlet fuel temperature increases at a rate of 1 ℃ with respect to T_{tank}. Subsequently, the fuel flows through the injector and the injector holes increases the temperature and it gives the biggest contribution. With regard to the present study, selecting the T_{tank} values as the representation of the thermal regime is sufficient. As has been explained, the injected flow-rate is sensitive to the temperature T_{tank} variation. The start of injection (SOI) does not vary with respect to the change of T_{tank}, while the end of injection (EOI) tends to occur earlier for a lower temperature value since the resulting injected flow-rate begins to decrease in advance with respect to a higher temperature one. The duration between SOI and EOI is then defined as ITL:

$$ITL = EOI - SOI \tag{4.5}$$

The *ITL* has also been expressed in Figs. 4.6a and 4.6b where the injected mass flow-rate remains higher than zero during this period. It can be inferred
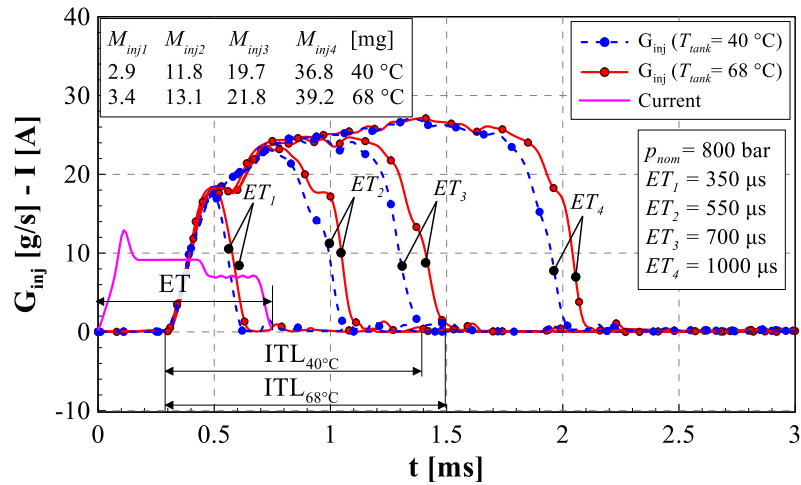
(a) p_{nom}=800 bar.
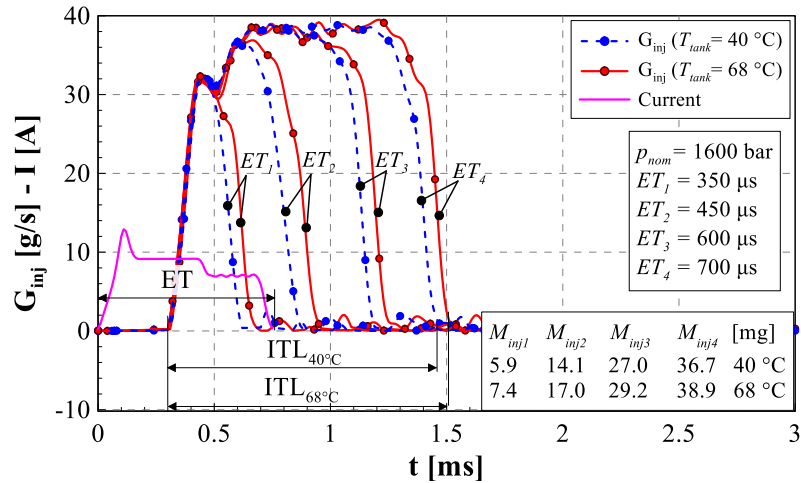
(b) p_{nom}=1600 bar.

Figure 4.6: Injected flowrate patterns pertaining to various *ET* under different thermal regimes.

that, under a higher T_{tank} value, ITL results to be longer ($ITL_{40°C} < ITL_{68°C}$).
This leads to a shift upwards of the correlation between injected mass and ET
if p_{nom} is the same and the fuel temperature increases which is shown in Fig.
4.4.

By substituting ITL for ET, the correlation between ITL and M_{inj} under
each nominal pressure level p_{nom} has been fitted through a 3rd polynomial
function as shown in Fig.4.7. Based on the performance, it can be concluded
that the $ITL - M_{inj}$ correlation remains the same when the fuel temperature
changes from 40 °C to 68 °C. It leads to a discovery that by applying ITL instead
of ET, the injector characteristics is less or almost not affected by the engine
thermal regime. In this way, by applying the correlation between ITL and
M_{inj}, along with the experimental data p_{nom} and ITL, it is possible to obtain
the M_{inj} which not depends on the fuel temperature T_{tank}. Compared with the
commonly applied correlation stored on the ECU, that is $M_{inj} = f(ET, p_{nom})$,
the one based on the ITL parameter results in a more robust and accurate
correlation.

4.2.3 Application of the TFA-based sensor

In Fig. 4.8, G_{inj} measured by means of HDA, $p_{inj,in}$ collected by the
pressure transducer, and the energizing current captured by the current clamp
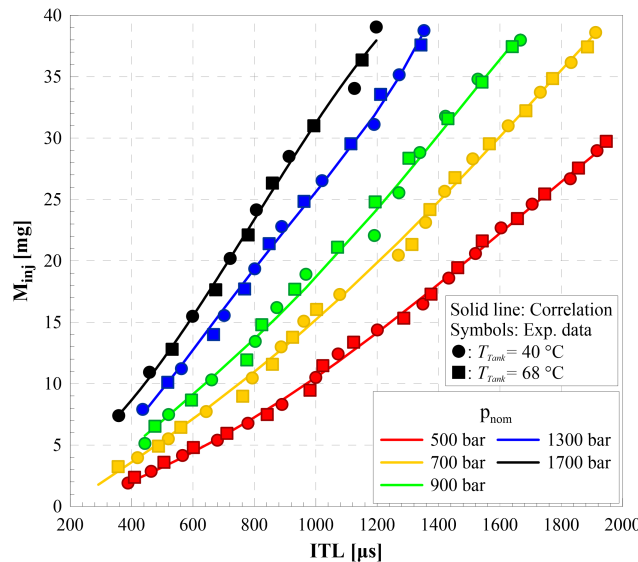
Figure 4.7: $ITL - M_{inj}$ correlations under various p_{nom} and T_{tank} levels.

have been reported for the working condition under $p_{nom} = 1200$ bar and $ET = 600$ µs. It should be noted that the reported traces are the data averaged by 100 consecutive engine cycles. Before the injection event is taken place, the pressure time history $p_{inj,in}(t)$ does not affected by any residual pressure oscillations presented in the hydraulic circuit and it keeps almost constant. As soon as the energizing current starts, the pilot valve opens and results in a slight decrease of pressure signal $p_{inj,in}$. Latterly, the start of injection (SOI) takes place which excites an expansion wave and $p_{inj,in}$ starts to drop dramatically that indicated as '1' in Fig. 4.8. The expansion wave travels along the rail and then reflected back towards the injector through rail-to-injector pipe. Under the transmission of the pressure wave, oscillations are generated and cause the fluctuations on the injector inlet pressure. These oscillations travelled along the pipe and are gradually damped by the wall friction as well as concentrated losses during the whole injection phase. At the end of injection (EOI), the water hammer phenomenon generated by the nozzle closure occurs and $p_{inj,in}$ reaches the highest value marked as 2.

During the entire injection event, the significant changes in $p_{inj,in}$ which are related to the hydraulic events occurred, marked as 1 and 2 in Fig. 4.8, namely SOI and EOI. In this way, the detection of time instants SOI and EOI is
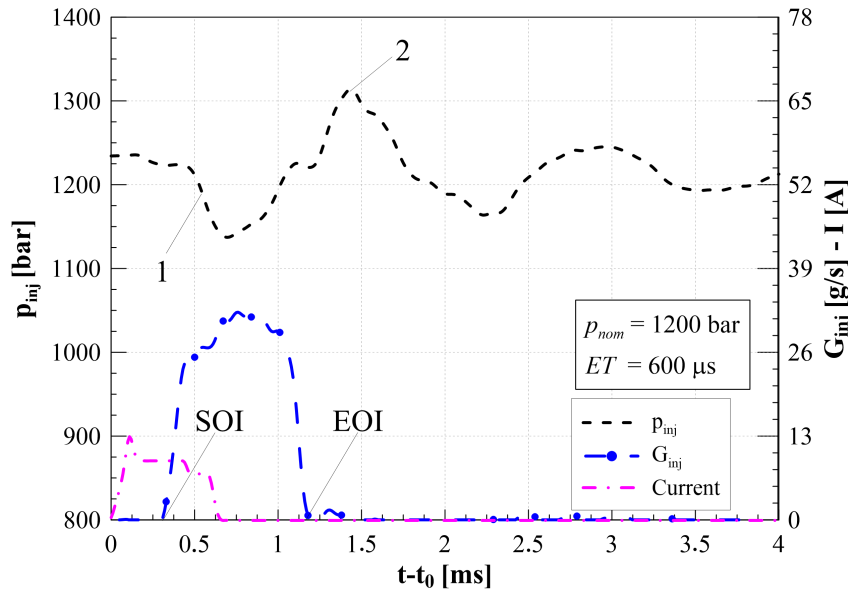
Figure 4.8: G_{inj}, $p_{inj,in}$ and the current under $p_{nom} = 1200$ bar and $ET = 600$ µs.

important and necessary by considering the control of injected mass. However, the presence of the pressure oscillations generated during the injection period causes disturbances on the determination of the time instants pertaining to *SOI* and *EOI*. Indeed, the travelling forward and backward pressure waves leads to an inaccuracy identification.

By applying TFA to the pressure time history $p_{inj,in}$, the useful and important information will be extracted since the signal has been analysed also in frequency aspect. The detection of the time instants pertaining to *SOI* and *EOI* could be applied for the injected mass estimation. Generally, the duration of the effective injection period, that is the period between *SOI* and *EOI*, lasts within 4ms. In order to avoid the disturbances of the leakage error that is generated by the spurious harmonic terms [113], the total length of the pressure signal $p_{inj,in}$ data which is processed with TFA has been subtracted into 8 ms.

A Butterworth low-pass filter with 4th order has been applied to the experimental data $p_{inj,in}$ in order to remove undesired fluctuations and smooth the signal. The cut-off frequency has been selected as 50 kHz and the processed signal, namely $p_{inj,in_{fil}}$, has been inserted to replace $f(t)$ displayed in Eq. (4.1). As far as the window function applied in Eq. (4.1) has been concerned, a Hanning type window has been chosen:

$$h\left(n\right) = 0.5 \ \left(1 - \cos\left(2\pi\frac{n}{N}\right)\right), \ 0 \leq n \leq N \qquad (4.6)$$

where n is indicated as a discretized time instant in the window and the window duration is represented as $N+1$ in accordance with the sample numbers. Referring to the present study, a window length equals to 502 μs has been applied. With regard to a sampling frequency selected as 500 kHz, N will be 251. The STFT has been performed to the pressure signal $p_{inj,in}$ by applying the parameters evaluated above. *MIF* is thus obtained with Eqs. (4.2) and (4.4). There is a concern that the value of the sampling frequency should be selected around 20 kHz in order to avoid the criticism with regard to the energy content contained in the pressure signal frequency spectrum [114]. This reduction is able to reduce the computational time significantly.

4.2.4   Results

Three different working points expressed in terms of p_{nom} and ET under $T_{tank} = 40\,°C$ have been displayed in Figs. 4.9-4.11. The corresponding electrical current, G_{inj}, $p_{inj,in}$ and MIF time histories during a time period of 4 ms have been plotted. With regard to the MIF, the initial value remains a constant value before the electrical current starts but not visible in the plots because of the large value generated by the leakage error.

Based on the information obtained from the analyzed MIF pertaining to the injector inlet pressure time histories, the time instant regarding to some important events during the injection can be identified. It could be concluded that the MIF trace could be applied to detect the needle movements, that is the starting ascendant phase regarding to the beginning of the injection and the latter descending phase where the injection finishes. During these periods, a higher resolution with fast changes could be seen in the MIF value. The MIF diagram starts to increase and reaches a local peak due to the nozzle opening, marked as "1" in Figs. 4.9-4.11, while the injected flowrate G_{inj} value is bigger than zero. The detected time instant could be considered as the hydraulic start of injection, namely SOI, which happens around 0.1 ms delay with respect to the nozzle opening time instant. This delay is the time needed by the rarefaction wave, which is triggered by the injection event, to travel from the nozzle and reach the pressure transducer [54]. At the end of injection where water hammer is occurred, MIF reaches the maximum absolute value and it is defined as the EOI which is located at about 0.1 ms after the hydraulic injection finishes. The criteria to identify the time instants regarding to the SOI and EOI holds for all the considered working points tested under both $T_{tank} = 40\,°C$ and $T_{tank} = 68\,°C$.

The estimated injection temporal length ITL_{est} obtained from the MIF trace and the real one ITL have been evaluated based on Eq. (4.5) with the corresponding experimental data pertaining to the MIF along with the injected flowrate. The analogous delays shown at the beginning and the end of ITL_{est} turns out to be coincident with ITL. With regard to the difference between ITL_{est} and ITL, the legend displayed in Figs. 4.9 and 4.10 shows the errors are 1.49 µs and 5.71 µs with both percentage errors lower than 1 %.

Same quantities plotted in Figs. 4.9 and 4.10 have been shown in Fig. 4.11 in terms of $p_{nom} = 600$ bar and $ET = 1000$ µs. The time instants regarding to

SOI and *EOI* detected with the aim of the *MIF* time history perform a time
delay of approximately 0.18 ms with respect to the real ones. On the other
hand, by considering the injected flowrate trace, the difference between the
ITL and ITL_{est} reaches up to 90.74 µs which is much higher with respect to
the ones in Figs. 4.9 and 4.10. For a very large *ET* working condition, the
estimation accuracy decreases and it could be explained by the double effect
caused by the reflected waves travelling along the rail and the water hammer
inside the rail-to-injector pipe (however, in the modern injection setup, an
injection features $ET = 1000$ µs is not commonly applied).

The ontained ITL_{est} values displayed in Figs. 4.9 and 4.10 have been
considered as the input parameters of the correlation shown in Fig. 4.7 and the
output will be the estimated injected mass ($M_{inj,est}$). The resulted predictions
of $M_{inj,est}$ referring to the above two working conditions are 30.84 mg and
16.01 mg, respectively. By comparing the estimated values with respect to
the corresponding measured injected mass obtained by means of the HDA
flowmeter, the errors regarding to the injection quantities can be considered to
be satisfied if they are within 0.5 mg. With regard to the reported working
condition in Fig. 4.11, the estimated injected mass of $M_{inj,est} = 27.56$ mg
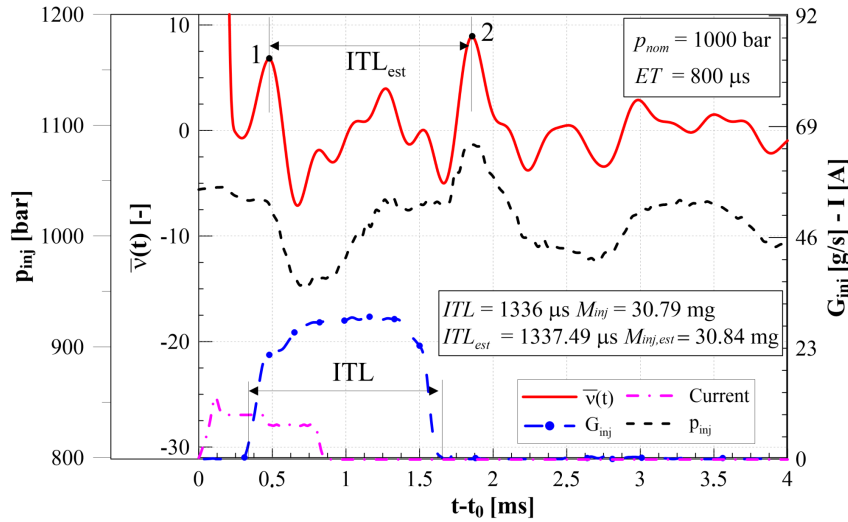
Figure 4.9: G_{inj}, $p_{inj,in}$ and the normalized *MIF* under $p_{nom} = 1000$ bar and
$ET = 800$ µs.
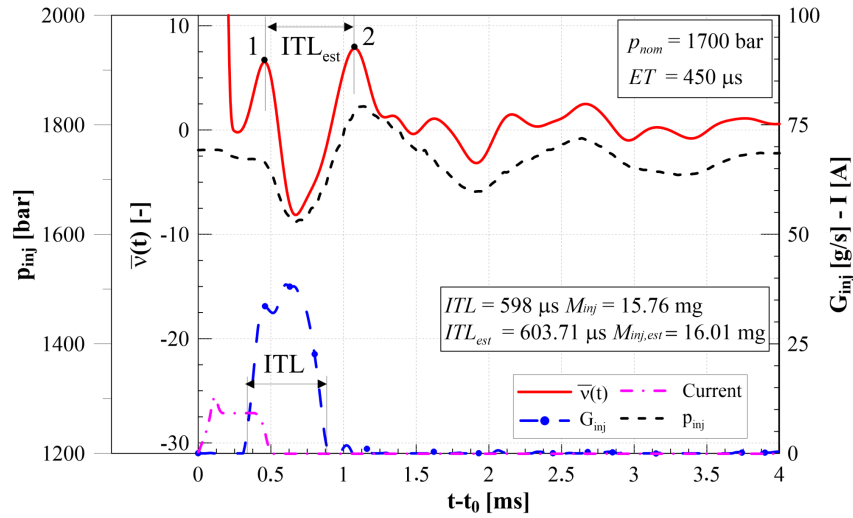
Figure 4.10: G_{inj}, $p_{inj,in}$ and the normalized MIF under $p_{nom} = 1700$ bar and $ET = 450$ µs.

results in a difference of 1.2 mg by comparing with the one obtained from the HDA flowmeter.

The developed correlation method based on the TFA analysis which is aimed at estimating the injected fuel quantity has been analysed under different steady-state working conditions with various p_{nom} and ET. The prediction accuracy $|\Delta M_{inj}|$ calculated by the absolute difference between M_{inj} and $M_{inj,est}$ has been reported in the vertical coordinate of the 3D diagram in Fig. 4.12 as a function of p_{nom} and ET. With regard to the fuel temperature, Fig. 4.12a refers to the one with $T_{tank} = 40$ °C and Fig. 4.12b features $T_{tank} = 68$ °C. The M_{inj} values, measured by the HDA flowmeter, have been considered as the average values of over 100 consecutive engine cycles under each working condition. The operating points with high p_{nom} and ET were not included inside the experimental tests by considering that the maximum limit on the injected mass per engine cycle is lower than 45 mg for these injectors application.

Based on the 3D graphs shown in Fig. 4.12, the prediction accuracy pertaining to the injected mass is almost within 1mg for more than 80% of the whole considered applications. The situations in which $|\Delta M_{inj}|$ reaches 1.5 mg are either 500 bar$\leq p_{nom} \leq$600 bar, medium and high ET values under
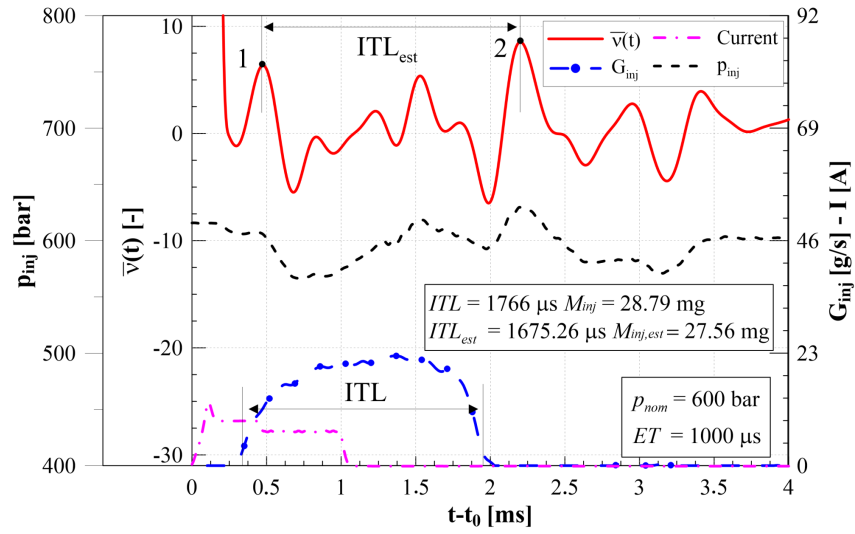
Figure 4.11: G_{inj}, $p_{inj,in}$ and the normalized MIF under $p_{nom} = 600$ bar and $ET = 1000$ µs.

$T_{tank} = 40$ ℃ and 60 ℃, while 350 µs $\leq ET \leq$ 450 µs and high nominal pressure levels p_{nom} for T_{tank} equals to both 40 ℃. The injected mass percentage errors have been calculated and displayed in the 3D diagrams belonging to Fig. 4.13 (cf. Fig. 4.13a refers to $T_{tank} = 40$ ℃ and cf. Fig. 4.13b refers to $T_{tank} = 68$ ℃). For the operating points with small injected masses under both two fuel temperatures, a low absolute error value (value lower than 1 mg) will cause a percentage error up to around 15% but still inside the acceptable range.

Double injections strategy with pilot-main injections have also been considered in the current investigation. It has been observed that the numerous events occurred during the multiple injections lead to the difficulty of detecting the ITL since $p_{inj,in}$ pressure signal has been affected especially under the short dwell time range situation. However, the proposed methodology could be applied to the first pilot injection mass control with regard to the multiple injections strategy and the improvement of soot and NO_x engine out emissions as well as the combustion noise could be achieved. The main injected fuel quantity could be controlled under the presented strategy with regard to a main-after injection train likewise.
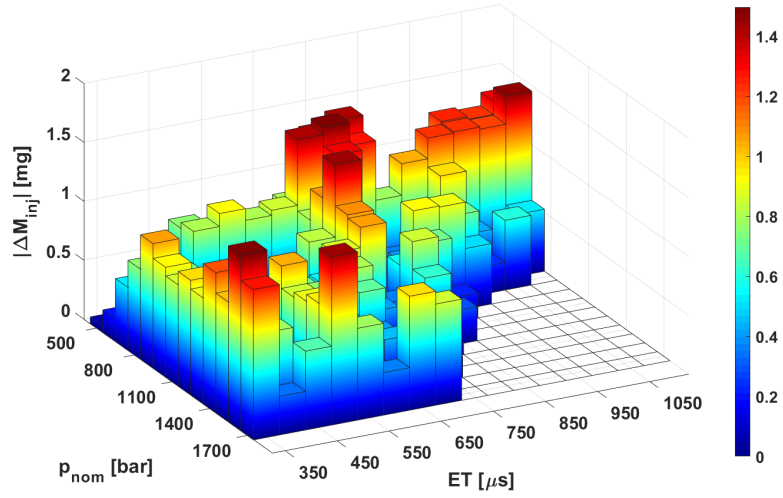
(a) T_{tank}=40 ℃.
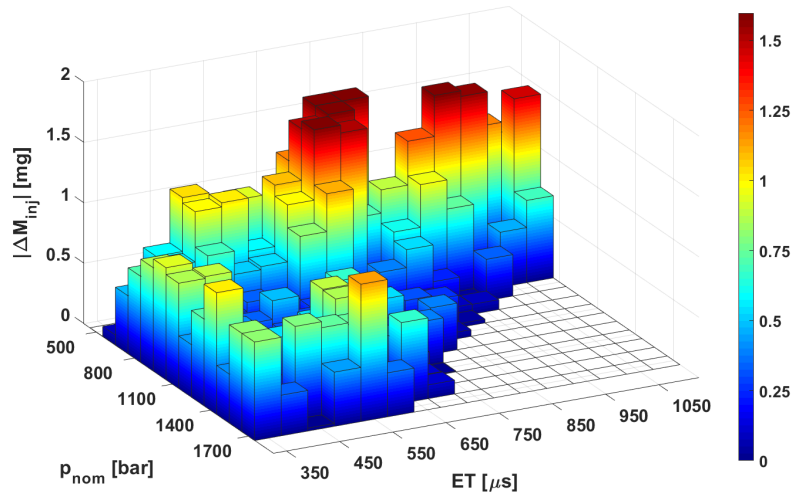
(b) T_{tank}=68 ℃.

Figure 4.12: Injected mass estimation error with respect to p_{nom} and ET under different T_{tank} values.

4.2.5   Discussion

The presented new strategy aimed at estimating the fuel injected quantity offers a simpler and more direct method than the compensative strategies mentioned in Sect. 6.2.3 where several procedures need to be accomplished
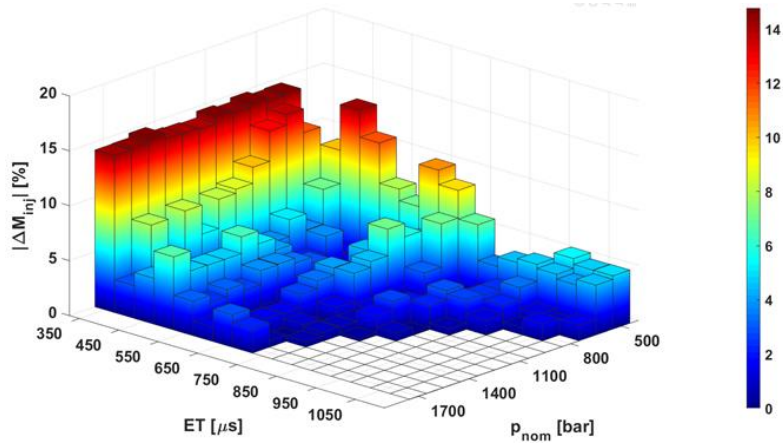
(a) $T_{tank}=40$ ℃.
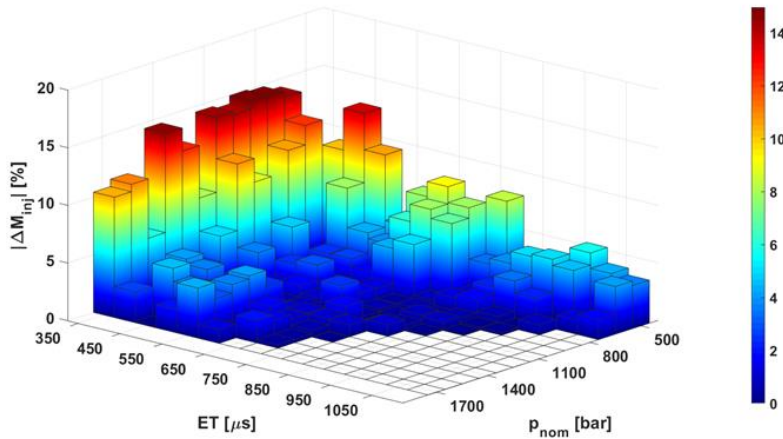
(b) $T_{tank}=68$ ℃.

Figure 4.13: Injected mass percentage error with respect to p_{nom} and ET under different T_{tank} values.

during the evaluation. Moreover, the proposed methodology could be applied to various types of injectors without modifying the injector internal structure.

By considering the error, that is $|\Delta M_{inj}|$, there are two primary sources. The first contribution is given by the correlation which cannot be ignored for

state-of-the-art injection systems although the fitting function is satisfactory with an accuracy within 0.5 mg. Another contribution, which is the primary source, is the inaccuracy prediction in the ITL due to the pressure waves superposition.

The injected flowrate pattern has been controlled both by the rail pressure p_{rail} (controlled by the ECU in the CR system) and by the needle dynamics. Usually, the latter factor has been considered roughly in the standard engine calibrations by choosing ET which differs markedly from the effective injection duration.

The correlation between the M_{inj} and ITL under different p_{nom} which is implemented on the engine ECU maps leads to a more consistent interpolation model since the selected ITL relates more closely to the needle lift dynamics with respect to ET. Moreover, the ITL-based correlation behaves independently to the injector thermal regime and it is important since it could be observed from Fig. 4.4 that the thermal effect of the injector influences remarkably the fuel injected quantity under fixed ET and p_{nom} working conditions.

The injected mass is lower than 3 mg for $p_{nom} \leq 800$ bar and $ET = 350$ μs (the pilot injection mass quantity is commonly lower than this value) based on the injector characteristics pertaining to T_{tank}=40 ℃ shown in Fig. 4.4. The corresponding fuel estimation mass percentage error is below 15% according to Fig. 4.13 for both two fuel temperature values which turns to be satisfied for the injected masses lower than 10 mg cases. However, the percentage error could reach 25 % when the fuel temperature varies from 40 ℃ to 68 ℃ with an open-loop control strategy. It should be noted that, under the low temperature combustion strategy, the pilot injected mass would reach 7-8 mg based on [115]. According to the 3D diagrams shown in Fig. 4.13, the corresponding percentage error is within 2%-15% range while the open-loop control strategy one is more than 30%. As a result, the injected mass control strategy could be applied to the first injection shot pertaining to the multiple injection train. As far as the multiple injections with short dwell times have been considered, the MIF time trace needs to be carefully taken into account by filtering the signal and removing the fluctuations generated by the pressure waves in order to realize the mass estimation procedure. This will be the future step of the new strategy development and optimization. Furthermore, the post injection for DPF regeneration aim could be controlled by the presented methodology.
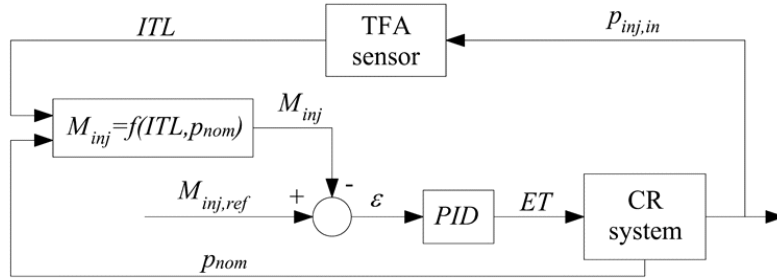
Figure 4.14: The scheme of the closed-loop strategy based on TFA analysis.

A schematic drawing of a feasible closed-loop strategy based on the current techinique has been shown in Fig. 4.14. The methodology is realized cycle-by-cycle with the information of ITL_{est}. The measured injector inlet pressure time history has been possessed through the TFA virtual sensor and the ITL has been estimated. By applying the correlation along with the parameters ITL_{est} and p_{nom}, the injected mass has been predicted ($M_{inj,est}$) and then compared with the target value ($M_{inj,ref}$) which is stored in the ECU calibration maps. The resulted difference, namely $\varepsilon = M_{inj,ref} - M_{inj,est}$, has been inserted into a PID controller as an input parameter and the output will be the corrected ET needs to be applied to the next injection cycle.

Chapter 5

Time-frequency analysis application to combustion noise in CI engines

5.1 Experimental facilities

The experimental campaign has been carried out on the dynamic test bed in the Politecnico di Torino IC laboratories. An AC dynamometer has been installed which features 520 Nm of nominal torque and 220 kW of nominal power. Its maximum speed is 12,000 rpm. Different types of diesel engines have been applied based on different injection strategies. A properly developed PCCI engine has been selected to perform single injection. It is a 3.0 liter, four-stroke prototype diesel engine supplied by Fiat Powertrain Technologies (FPT) Industrial, namely F1C engine. The important informations with regard to the engine have been displayed in Table 5.1. The premixed combustion phase HRR is restricted by the low compression ratio (14.6:1) and high EGR rate and it is an early PCCI injection strategy. A simple schematic drawing of the tested engine installed at the test bench has been shown in Fig. 5.1. With regard to the multiple injections, the tested engine A20DTR from General Motor and its main technical specifications have been displayed in Fig. 5.2 and Table 5.2. It is a Euro 5 diesel engine that fuels with conventional diesel oil. $PCCI$ fuel injection strategy is the late injection type and is obtained only at low load (about 2 bar, where in the F1C PCCI it could achieve 8 bar).

Table 5.1: Main specifications of the F1C engine

Engine type	3.0L diesel direct injection
Displacement	2998cm^3
Bore x stroke	95.8 mm x 104 mm
Compression ratio	14.6
Valves per cylinder	4
Turbocharger	Single stage with VGT
Fuel injection system	Common Rail solenoid injectors
EGR system type	Short-route cooled EGR
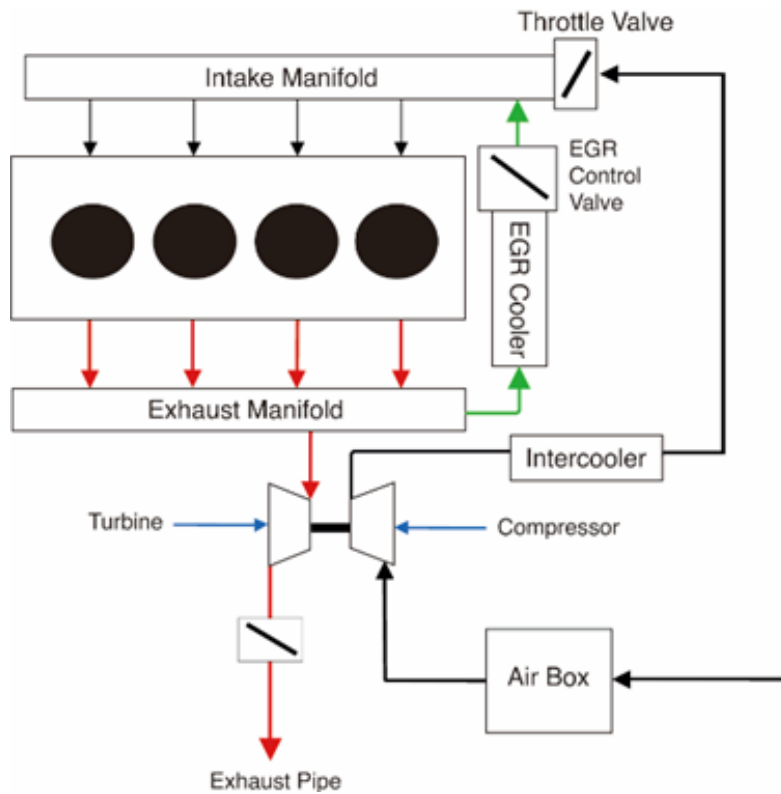
Figure 5.1: Schematic of the F1C engine.

With regard to the in cylinder gas pressure signal collecting method, a piezoelectric transducer featuring a high frequency has been mounted. It has been installed on the engine cylinder head and then fitted into a glow plug adapter. Another piezoresistive type pressure transducer has been placed in the intake manifold in order to reference the captured in-cylinder pressure with respect to the absolute one (pegging). The tested working points have been selected in order to represent the typical vehicle driving conditions along NEDC.

Table 5.2: Main specifications of the A20DTR engine

Engine type	2.0L Euro 5
Displacement	$1956cm^3$
Bore x stroke	93.0 mm x 90.4 mm
Compression ratio	16.3
Valves per cylinder	4
Turbocharger	Twin-stage with valve actuators and WG
Fuel injection system	Common Rail piezo indirect acting injectors
EGR system type	Short-route cooled EGR
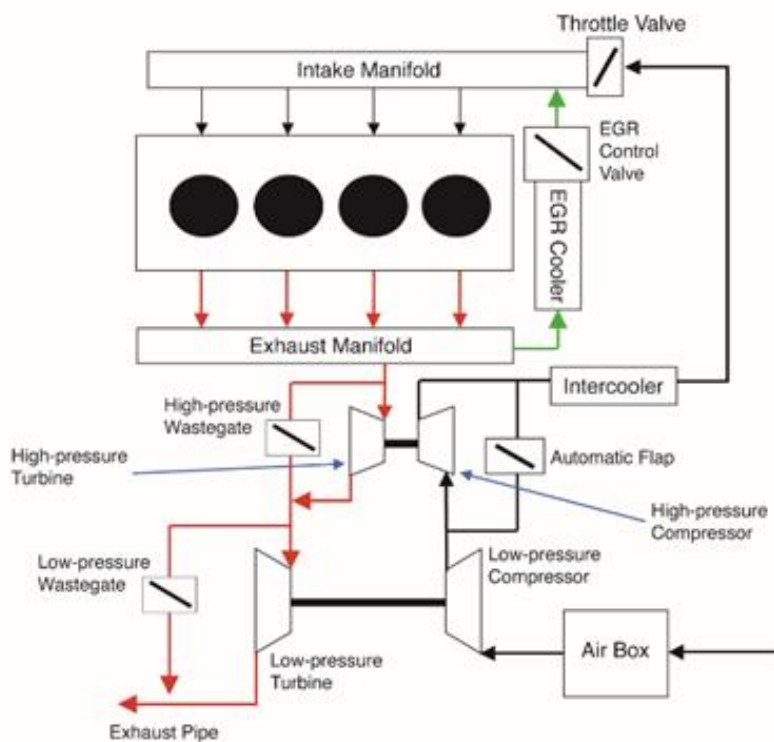
Figure 5.2: Schematic of the A20DTR engine.

The selected key points have been represented as speed n (rpm) and *bmep* (bar): 1400x3 for single injection strategy tested with F1C, 1500x5, 2000x2, 2000x5, 2500x8 and 2750x12 for multiple injection tested with A20DTR. As fas as the combustion noise evaluation method is concerned, AVL concerto commercial software has been applied with the input of the captured absolute in-cylinder pressure transients on the basis of the classic procedure [116, 117]. The measured pressure signal is needed to be processed preliminarily with a

low-pass type filter which features 5 kHz cut-off frequency in order to remove the pressure sensor installation effect. A fast Fourier transform function is then applied to the filtered pressure signal for the aim of evaluating the sound pressure level, namely SPL. The one-third octave band analysis has been selected in the combustion noise calculation. The frequency values have been split into different bands and within each band the obtained power spectral values are summed up and then redistributed to the corresponding center frequency. By considering the noise radiated from the engine due to the in-cylinder pressure variation, a transfer function which stands for the engine block attenuation has been applied. Moreover, the human ear sensitivity has also been taken into account during the calculation and the obtained combustion noise is measured in A-weighted dB.

5.2   In-cylinder pressure processing

During the combustion, the change in the in-cylinder pressure is due to the combustion event, the cylinder reciprocating movement as well as heat exchanges. With regard to the pressure rise due to the volume change and to the heat transfer from charge-to-wall, the change from p_{i-1} to p_{i-1} during the crank angle interval between θ_{i-1} and θ_i ($\theta = \omega \times t + \theta_0$) has been evaluated as a polytropic process based on the Rassweiler and Withrow theory [118, 119]:

$$
p_i = \begin{cases} p_{i-1}[V_{i-1}/V(\theta_i)]^{m_c} & \theta_i \leq \theta_{TDC} \\ p_{i-1}[V_{i-1}/V(\theta_i)]^{m_e} & \theta_i > \theta_{TDC} \end{cases} \tag{5.1a}
$$

where m_c and m_e refer to the polytropic exponents with regard to the compression and expansion strokes, respectively. The values of the exponents have been obtained by average values based on the pressure and volume data without the presence of the combustion. The polytropic pressure p has been considered as the motored pressure trace, namely p_{mot}, for the current study.

By subtracting the motored pressure p_{mot} from the in-cylinder pressure trace measured by the pressure sensors, namely p_{cyl}, the pressure difference Δp_{comb} could be obtained:

$$
\Delta p_{comb}(\theta_i) = p_{cyl}(\theta_i) - p_{mot} \tag{5.2}
$$
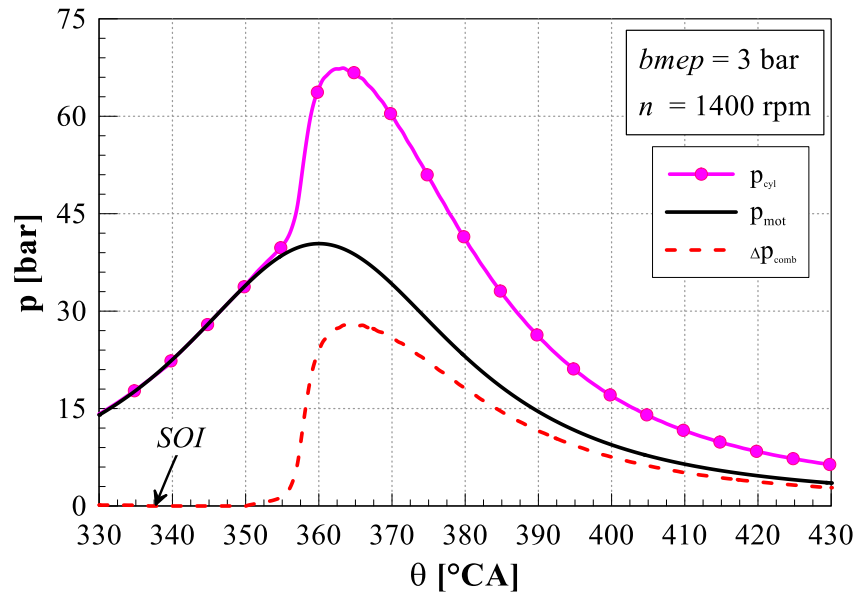
Figure 5.3: Δp_{comb}, p_{mot} and p_{cyl} versus θ distributions ($bmep = 3$ bar and $n = 1400$ rpm).

The working condition with $bmep = 3$ bar and $n = 1400$ rpm has been analysed with regard to the Δp_{comb}, p_{mot} and p_{cyl} and the result has been shown in Fig. 5.3.

5.3 Time-frequency analysis

By applying the time-frequency analysis to the signals, both time and frequency domains are considered as mentioned in Chap. 4. The evaluated spectrum could be used to detect the changes of a transient signals. The captured raw in-cylinder pressure signal p_{cyl} needs to be pre-processed by applying a selected filter in order to remove the spurious pressure fluctuations due to the pressure transducer installation. With regard to the filter, a low pass filter type featuring a 5 kHz cutting frequency has been applied. The combustion noise analysis has been carried out by evaluating the in-cylinder pressure signal based on the Choi-Williams distributions by considering the time-frequency analysis. The Choi-Williams distributions characterize the energy conservation properties pertaining to the time and frequency marginals which could preserve the physical meaning. The introduction of the kernel is

aimed at reducing the interference problems [120]. A common selection for the kernel is the Gaussian function [121]:

$$\varphi(\tau,\nu) = e^{-(2\pi\tau\nu)^2/\sigma} \tag{5.3}$$

In Eq. (5.3), the width of kernel is adjusted by the parameter σ. The time dependent autocorrelation function of the in-cylinder pressure signal $p_{cyl}(t)$ is performed as follows [122]:

$$R(\mu,\tau) = p_{cyl}(\mu+\frac{\tau}{2})p_{cyl}(\mu-\frac{\tau}{2}) \tag{5.4}$$

The Choi-Williams is then calculated in the Fourier transform:

$$CW(\nu,t) = \int_{-\infty}^{+\infty} e^{-j2\pi\nu\tau} \left[\int_{-\infty}^{+\infty} \frac{1}{\sqrt{\frac{4\pi\tau^2}{\sigma}}} e^{\frac{(\mu-t)^2}{4\tau^2/\sigma}} p_{cyl}(\mu+\frac{\tau}{2})p_{cyl}(\mu-\frac{\tau}{2})d\mu \right] d\tau \tag{5.5}$$

A time window function $h(\tau)$ can be applied to the integrand of Choi-Williams distribution in order to diminish the asynchronous cross-term interference. Moreover, another window function $g(t-\mu)$ is selected to constrain the signal portion to be analysed based on the frequency domain [123]. The modified Choi-Williams distribution by applying two window functions is defined as the smoothed Choi-Williams (SCW) with the following equation:

$$SCW(\nu,t) = \int_{-\infty}^{+\infty} e^{-j2\pi\nu\tau} [\int_{-\infty}^{+\infty} h(\tau)g(t-\mu)\frac{1}{\sqrt{\frac{4\pi\tau^2}{\sigma}}} e^{\frac{(\mu-t)^2}{4\tau^2/\sigma}}$$
$$p_{cyl}(\mu+\frac{\tau}{2})p_{cyl}(\mu-\frac{\tau}{2})d\mu]d\tau \tag{5.6}$$

There are different types of window functions to be selected and performed. In the present study, for both the time smoothing window function h and the frequency window function g, the Hanning window defined as following has been chosen:

$$w_H(n) = 0.5(1-\cos(2\pi\frac{n}{N})), 0 \leq n \leq N \tag{5.7}$$

where n is the discretized time instant along the window and N refers to the window support. The Hanning window is a continuous function and the center is placed at point $N/2$. In this way the window does not produce the spurious high frequencies components into the signal frequency aspect. The resolution

of the time domain is decided by the window temporal extension. Based on Heisenberg's uncertainty principle [124], there is a compromise between the time and frequency resolution. To be specific, a reduction in the time window length leads to a better frequency resolution but to a lower time resolution while a narrow frequency window results in a higher time resolution but with more uncertainty in the frequency domain. Therefore, special attention should be paid during the Choi-Williams distribution evaluation. In order to obtain the expected performance, the parameters of the window type with regard to the time support h and frequency content of window g needs to be considered carefully. The energy density spectrum, which referring to the frequency marginal of the smoothed Choi-Williams distribution of the in-cylinder pressure, has been obtained by integrating $SCW(\nu,t)$ over time at a specific frequency ν:

$$P_{CW}(\nu) = \int_{-\infty}^{+\infty} SCW(\nu,t)dt \tag{5.8}$$

As far as the combustion noise (Cn) is concerned, the sound pressure level has been considered by splitting the energy into different bands with a one-third octave bandwidth referring to the method explained in [79]. Afterwards, the energy E_i in each band interval could be obtained through the integral of P_{CW} over the frequency domain:

$$E_i = \int_{\nu_i}^{\nu_{i+1}} P_{CW}(\nu)d\nu \tag{5.9}$$

where ν_i and ν_{i+1} represent the extreme frequency values of the i-th band. The sound pressure level pertaining to the i-th band, namely SPL_i, is evaluated according to the logarithmic formula [125]:

$$SPL_i = 10\log(E_i/p_{ref}^2) \tag{5.10}$$

where p_{ref} is the reference pressure with respect to the human hearing threshold at 1 kHz and it equals to $20\,\mu$Pa.

The effective sound pressure level (SPL_{f_i}) has taken into account the two filters which stand for the engine block attenuation and human ear [126]. Finally, the overall combustion noise, namely Cn_{ov} [dB], evaluated through the three on-third octave bad levels is obtained [127]:

$$Cn_{ov} = 10 \log(\sum_i 10 \frac{SPL_{f_i}}{10}) \tag{5.11}$$

In order to evaluate the generated combustion noise based on the time domain during the combustion event, Eqs. (5.10) and (5.11) need to be reapplied at each time instant by performing the time marginal energy density of smoothed Choi-Williams distribution:

$$\dot{E}_i(t) = \int_{-\infty}^{+\infty} SCW(\nu,t)d\nu \tag{5.12}$$

In Eq. (5.10), E_i has been replaced with $\dot{E}_i$ in order to obtain the instantaneous sound pressure level:

$$S\dot{P}L_i(t) = 10 \frac{1}{E_i \times \ln 10} \dot{E_i}(t) \tag{5.13}$$

By considering the engine block and human hearing perception, the effective sound pressure level with respect to time, that is $S\dot{P}L_{f_i}(t)$, is obtained. Therefore, the instantanous combustion noise $\dot{C}n(t)$ [dB/ms] could be calculated based on Eq. (5.11). The combustion noise contribution of different combustion phases is then evaluated through the integration of $\dot{C}n(t)$ along time period and by applying one coefficient k which is obtained from the combustion noise experimental data:

$$Cn_j = \int_{t_j}^{t_{j+1}} \dot{Cn}(t)dt \times k \tag{5.14}$$

where j represents a specific combustion phase that its duration from t_j to t_{j+1}.

5.4   Mean instantaneous frequency

In order to detect each combustion phase occurred during the combustion, the mean instantaneous frequency (MIF) concept has been performed [118, 93]. This technique could provide the physical representation pertaining to the qualitative analysis as already mentioned in Sect. 4.2.1. With the input signal selected as the in-cylinder pressure signal, the significant time instants related

to the combustion could be identified. Firstly, the short-time Fourier transform (STFT) should be performed to the pressure time history $p_{cyl}(t)$:

$$F_l(\nu,t) = \int_{-\infty}^{+\infty} p_{cyl}(t)h(t-\tau)e^{-j2\pi\nu\tau}d\tau \qquad (5.15)$$

It should be noted that the window function h shown in the Eq. (5.15) is the same as the one chosen for the Choi-Williams distribution, that is the Hanning window function.

$F_l(\nu,t)$ squared is defined as the signal spectrogram P_f:

$$P_f(\nu,t) = |F_l(\nu,t)|^2 \qquad (5.16)$$

The probability density function of the instantaneous frequency $\bar{\nu}(t)$ is evaluated based on the function P_f:

$$\bar{\nu}(t) = \frac{1}{\int_{-\infty}^{+\infty} P_f(\nu,t)d\nu} \int_{-\infty}^{+\infty} \nu P_f(\nu,t)d\nu \qquad (5.17)$$

With the aid of the calculated mean instantaneous frequency $\bar{\nu}(t)$, the input pressure signal variation from the spectral content aspect could be detected. To be specific, the important time instants occurred during the combustion events, such as injection, spray vaporization, ignition and the following combustion process, could be identified by analysing $\bar{\nu}(t)$ trace. The first derivative of $\bar{\nu}(t)$, namely $\bar{\nu}'(t)$, is obtained by means of a finite difference formula.

5.5   Validation

The acoustic localization and multiple microphone array techniques have not been carried out in the proposed methodology. Generally speaking, the time-frequency analysis is able to provide a qualitative result and a scaling factor is required when considering the quantitate analysis. In the current research, the instantaneous combustion noise pattern has been scaled with respect to the global noise value based on the classic procedure explained in Sect. 5.1 in order to provide a correct combustion noise value after the integration process.

In Sects. 5.3 and 5.4, the methodology to obtain the combustion noise and mean instantaneous frequency has been presented and this has been validated
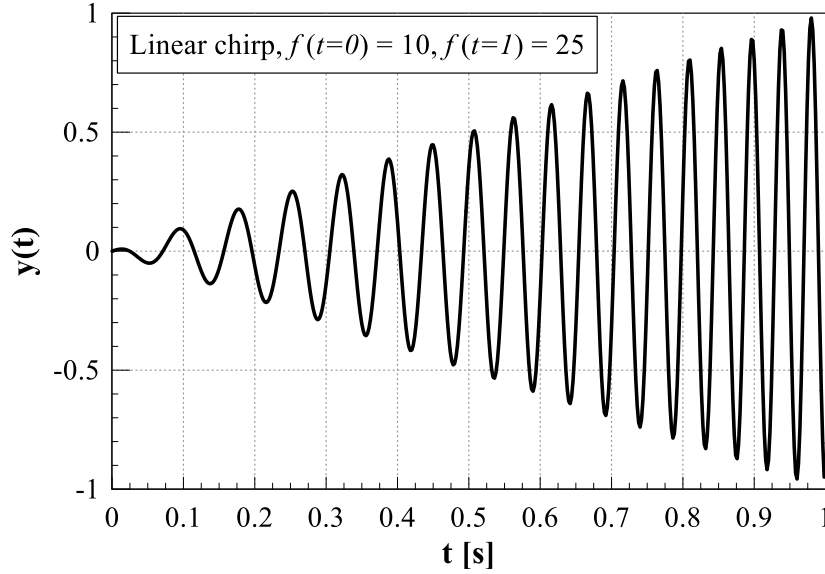
Figure 5.4: The tested linear chirp signal.

in order to verify its veracity and reliability. A linear chirp signal which has a linearly increasing amplitude defined in Eq. (5.18) has been tested:

$$y(t) = t \times \cos(2\pi f(t) \times t) \tag{5.18}$$

where the theoretical frequency $f(t)$ is expressed as $f(t) = \frac{f(t=1)-f(t=0)}{2T}t + f(t=0)$ and T refers to the time period. The chirp signal has been shown in Fig. 5.4.

The validation results pertaining to the frequency and the normalized instantaneous combustion noise of the selected chirp signal have been shown in Fig. 5.5. The upper figure, which corresponds to the frequency, has demonstrated that the mean instantaneous frequency $\bar{\nu}(t)$ evaluated from Eq. (5.17) (plotted in solid line) is almost overlapped with the theoretical frequency $f(t)$ (plotted in symbols). The lower figure shows the comparison with regard to the instantaneous combustion noise $\dot{C}n(t)$. The theoretical approach to calculate $\dot{C}n(t)$ for the linear chirp signal is derived from the cosinusoidal wave featuring a specific frequency $f(t)$ at each time instant which is the same as the chirp signal. The presented validation test, results displayed in Fig. 5.5, show that the methodology based on the time-frequency analysis could achieve
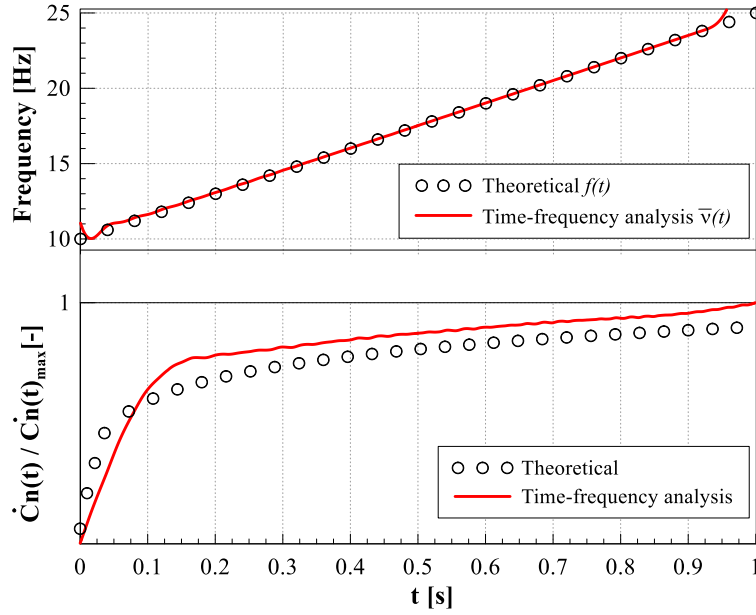
Figure 5.5: Validation of $\bar{\nu}(t)$ and the normalized $\dot{C}n(t)$ of a linear chirp signal.

reliable prediction in terms of mean instantaneous frequency and the normalized instantaneous combustion noise.

In the literature review, which focusing on the combustion noise evaluation, the in-cylinder pressure signal p_{cyl} has been more selected as the input parameter. Nevertheless, the presented time-frequency analysis shown in Sects. 5.3 and 5.4 appears to demonstrate that the p_{cyl} pressure signal does not lead to a reliable instantaneous combustion noise $\dot{C}n(t)$. An example with regard to the instantaneous combustion noise pertaining to a single injection ($bmep = 3$ bar and $n = 2000$ rpm) is shown in Fig. 5.6. Three different pressure signals, in-cylinder pressure p_{cyl}, combustion pressure signal Δp_{comb} and motored pressure p_{mot}, have been applied in the presented methodology in order to calculate $\dot{C}n(t)$. The in-cylinder pressure signal $p_{cyl}(t)$ is composed of the Δp_{comb} and the polytropic pressure signal p. When a multicomponent signal which features time varied frequency, that is, $p_{cyl}(t)$, has been processed with the Choi-Williams distribution, the perfomance is bad due to the specific feature of the kernal. When a small τ is applied, the kernal value is then small and the information from the autocorrelation function $p_{cyl}(\mu + \frac{\tau}{2})p_{cyl}(\mu - \frac{\tau}{2})$ is not fully considered. The loss of this information results in the poor resolution of the Choi-Williams distribution when it has been applied to study the characteristics
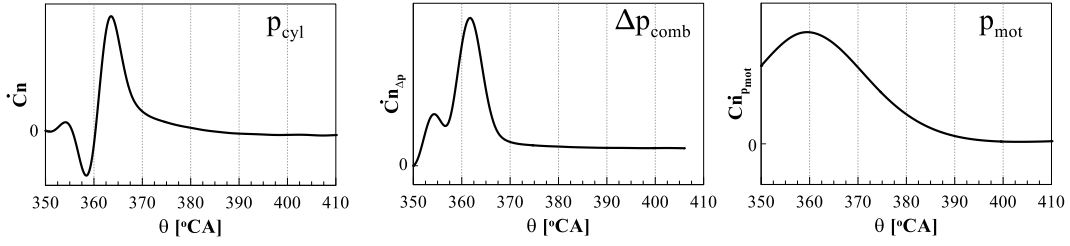
Figure 5.6: Instantaneous combustion noise evaluated from p_{cyl}, Δp_{comb} and p for a single injection ($bmep = 3$ bar and $n = 2000$ rpm).

of the signal. This explains the inconsistencies appeared in the $\dot{C}n(t)$ plot pertaining to in-cylinder pressure, shown in Fig. 5.6, that reveals a negative trend from $\theta \approx 355$ °CA to $\theta \approx 362$ °CA. In this way, the chosen pressure signal for the time-frequency analysis should be Δp_{comb} and the procedure shown in Sect. 5.3 needs to repeated with the input signal as Δp_{comb}. The corresponding instantaneous combustion noise is therefore named as $\dot{C}n_{\Delta p}(t)$ and the contribution is referred to as $Cn_{\Delta p}$.

The FFT analysis has been further performed for the validation process in the frequency domain. The obtained sound pressure level value from Eq. (5.10) is compared with respect to the one derived from the FFT. The previous introduced linear chirp signal and an engine working point in terms of $bmep = 3$ bar and $n = 2000$ rpm (F1C engine) have been selected for the validation. In Figs. 5.7 and 5.8, the results obtained from the classic procedure (described in Sect. 5.1) have been displayed in the solid bar and the hatched bar represents the result evaluated from the proposed time-frequency analysis method. Although the small differences have been detected due to the inaccuracy introduced by the smoothing window functions h and g, the innovative method to achieve the combustion noise is able to reach a reliable result.

5.6   Single injection result

A single injection under $bmep = 3$ bar and $n = 2000$ rpm has been reported in Fig. 5.9. In the plot, the filtered in-cylinder pressure p_{cyl}, the calculated motored pressure p_{mot}, the injected flowrate G_{inj} measured at the hydraulic rest rig, the mean instantaneous frequency $\bar{\nu}(t)$ and its first derivative $\bar{\nu}'(t)$,
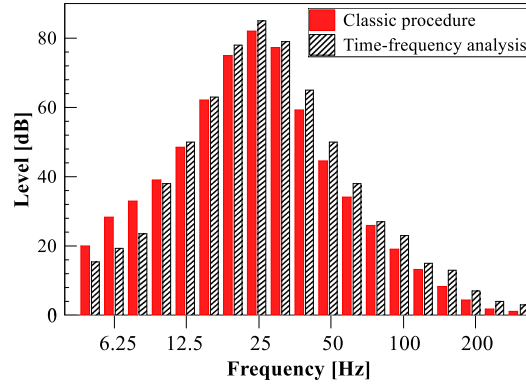
Figure 5.7: One-third octave bands pertaining to the chirp signal.
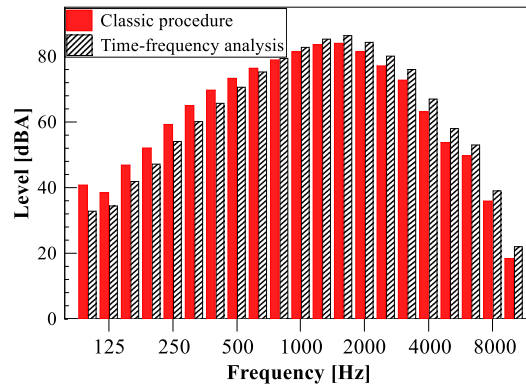
Figure 5.8: One-third octave bands pertaining to one operating point ($bmep = 3$ bar and $n = 2000$ rpm).

the instantaneous combustion noise $\dot{Cn}_{\Delta p}(\theta)$ evaluated based on Δp_{comb} have been demonstrated. Besides, a three-zone diesel combustion diagnostic tool presented in [128] has been applied to p_{cyl} and G_{inj} in order to obtain HRR and x_b time histories.

At the beginning ($\theta \approx 340$ °CA), $\bar{\nu}(\theta)$ starts to slowly increase since the fuel has been injected into the engine cylinder. The latterly decrease in $\bar{\nu}(\theta)$, located at $\theta \approx 346$ °CA, is due to the fuel evaporation process and this leads to a local minimum point 1 where $\bar{\nu}'(\theta)$ equals to zero. The considered fuel injection strategy is an early PCCI strategy which the advance fuel injection timing is occurred during the piston compression stroke ($SOI \approx 340$ °CA) and under low load. In this way the cool flames are presented during the combustion and the local minimum value of $\bar{\nu}(\theta)$, indicated as point 1, identifies the start of the cool flames and $\bar{\nu}(\theta)$ starts to grow with the combustion process. As far
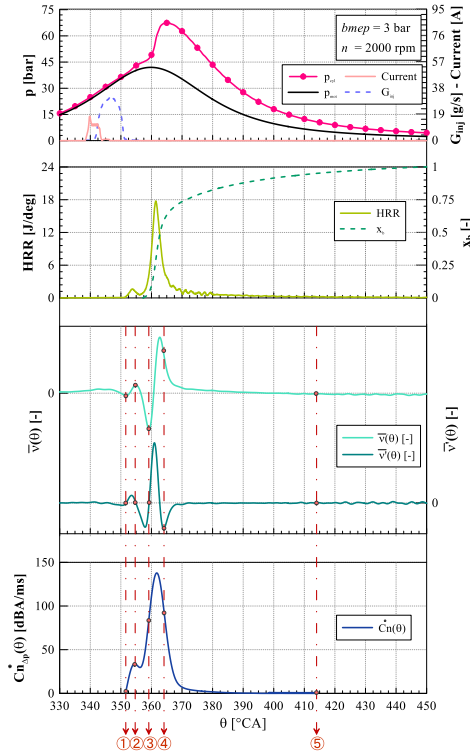
Figure 5.9: Single injection ($bmep = 3$ bar and $n = 2000$ rpm).

as the HRR pattern has been concerned, an obvious heat has been released during the cool flames period and the peak is reached at $\theta \approx 354$ °CA. The cool flames are finished when $\bar{\nu}(\theta)$ achieves the maximum value at point 2 and the corresponding $\bar{\nu}'(\theta)$ decreases into zero. Starting from point 3, $\bar{\nu}(\theta)$ starts to increase rapidly and this is related to the start of combustion (SOC) taken place in the premixed combustion phase. It lasts until $\bar{\nu}'(\theta)$ reaches the local minimum value, namely point 4. And from then on, $\bar{\nu}(\theta)$ starts to drop and $\bar{\nu}'(\theta)$ rises, which means the diffusive combustion phase starts to go on. The end of combustion is detected according to $x_b = 0.95$ and it is indicated as point 5 where is located around $\theta \approx 415$ °CA.

The corresponding smoothed Choi-Williams distribution $SCW(\nu, \theta)$ has been plotted in a 3D version in terms of time (crank angle θ) and frequency (ν) and the result is displayed in Fig. 5.10. It has been shown that $SCW(\nu, \theta)$ differs from zero only during the combustion period that lasts from $\theta \approx 350$ °CA to $\theta \approx 450$ °CA and during the premixed combustion stage a significant bump is taken place. As far as the frequency content of the physical phenomenon
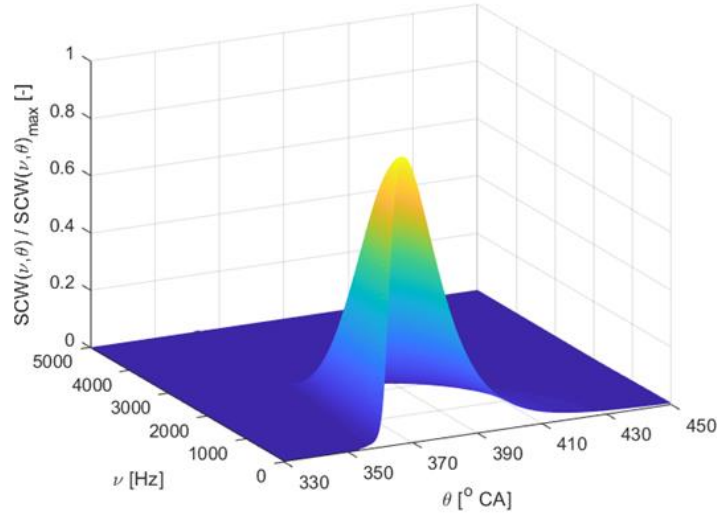
Figure 5.10: Normalized smoothed Choi-Williams distribution ($bmep = 3$ bar and $n = 2000$ rpm).

has been concerned, it never exceeds 3 kHz. Based on the plot, the integration of the instantaneous combustion noise $\dot{C}n_{\Delta p}(\theta)$ in terms of ν is realized by transecting the considered distribution in Fig. 5.10 with a constant θ plane.

The contributions of Δp_{comb} generated combustion noise with regard to different combustion stages to the coverall one have been achieved through the integration of the instantaneous combustion noise $\dot{C}n_{\Delta p}(\theta)$ along the time domain (crank-angle). In Table 5.3, the results have been presented.

As can be seen from Fig. 5.9, the instantaneous combustion noise $\dot{C}n_{\Delta p}(\theta)$ starts to increase since SOI when Δp_{comb} differs from zero. The rising rate of $\dot{C}n_{\Delta p}(\theta)$ pertaining to the premixed combustion phase is relatively high as the result of the suddenly increased in-cylinder pressure p_{cyl}. The rest contribution is given by the on-going diffusive combustion phase while $\dot{C}n_{\Delta p}(\theta)$ starts to slowly decrease into the null value. According to the results shown in Table 5.3, the premixed combustion phase shares a dominant contribution to the total combustion noise related to Δp_{comb} because of its rapid and unsteady process, and secondly, the diffusive combustion phase which has the longest duration, and the last is the cool flames.

Table 5.3: Combustion noise subdivision($bmep = 3$ bar and $n = 2000$ rpm)

Combustion stage	$Cn_{\Delta p}[dBA]$
Cool flames (1-2)	3.5
Premixed phase (3-4)	44.5
Diffusive phase (4-5)	22.4

It should be noted that the above interpretation and discussion concerning the combustion stages detections and the combustion noise contributions have been dedicated to the single injection PCCI strategy. They are also applicable to the medium working points. The same quantities shown in Figs. 5.9 and 5.10 have been plotted again in Figs. 5.11 and 5.12 with regard to a working point $bmep = 7$ bar and $n = 2000$ rpm. The combustion noise contribution of each phase to the overall one $Cn_{\Delta p}$ is also presented in Table 5.4.

The methodology to identify each combustion stage is the same as those applied in Fig. 5.9. Under this high load working condition, the cool flames still occurs before the premixed phase due to SOI is taken place early during the
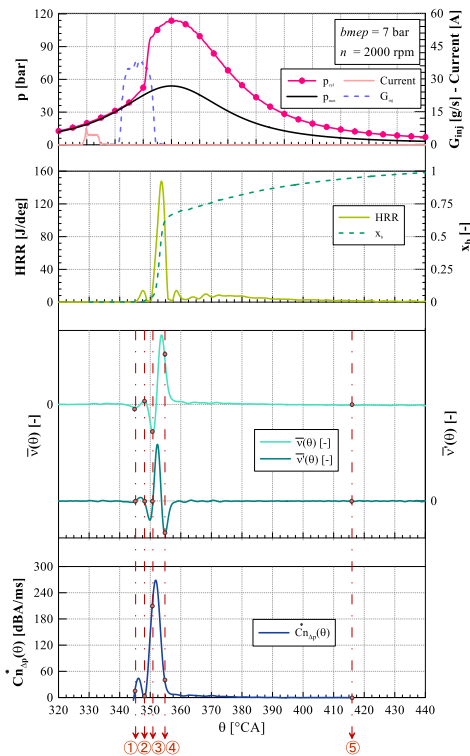
Figure 5.11: Single injection ($bmep = 7$ bar and $n = 2000$ rpm).
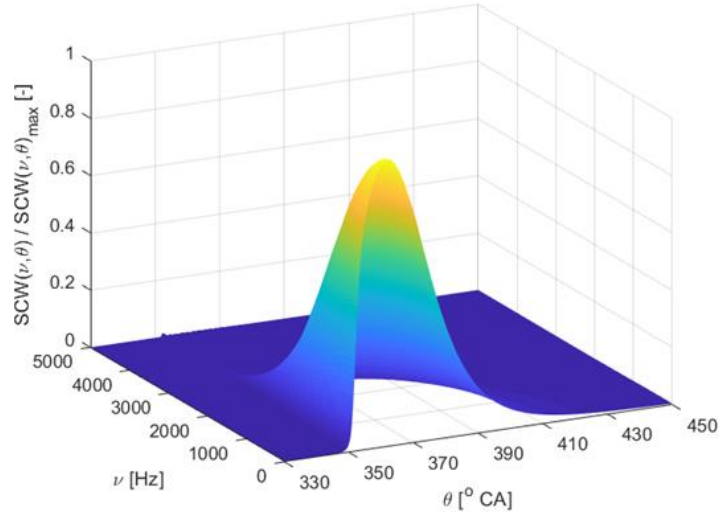
Figure 5.12: Normalized smoothed Choi-Williams distribution ($bmep = 7$ bar and $n = 2000$ rpm).

compression phase. The hot stage of the combustion process, that is premixed phase, releases a large amount of heat in a considerably short duration and this generates a maximum value of instantaneous combustion noise $\dot{C}n_{\Delta p}(\theta)$. During the latter part of the combustion, a mixing-controlled tail is presented and the generated combustion noise slowly reduces. It lasts for a relatively long time but results in a low level of combustion noise. Similarly, the premixed combustion stage gives the biggest contribution to the overall combustion noise while the cool flames contribution is not inappreciable.

Table 5.4: Combustion noise subdivision($bmep = 7$ bar and $n = 2000$ rpm)

Combustion stage	$Cn_{\Delta p}[dBA]$
Cool flames (1-2)	6.6
Premixed phase (3-4)	62.2
Diffusive phase (4-5)	10

5.7   Double injections low load condition

Figs. 5.13 and 5.14 correspond to a double injections strategy featuring the dwell time $DT \approx 1600$ µs. The operating point is $bmep = 2$ bar and $n = 2000$ rpm with a low temperature combustion strategy that the main injection is taken place after TDC.

In order to lengthen the ingintion delay, a high portion of EGR has been applied which equals to $x_{EGR} \approx 47\%$. As a result, a highly premixed combustion happens, as the combustion process pertaining to each injection shot begins when the corresponding injection has been finished. Indeed, positive ignition dwell are formed for both pilot and main injections and the fuel has been burned mostly under premixed combustion phase. As far as pilot combustion is concerned, it features a two-stage combustion with cool flames and hot ignitions. The evaporation of the pilot injected fuel decreases $\bar{\nu}'(\theta)$ and when the value of $\bar{\nu}'(\theta)$ reaches a local minimum the combustion starts. The time instant where $\bar{\nu}(\theta)$ equals to zero, namely point 1, indicates the beginning of the primary

Figure 5.13: Double injection ($bmep = 2$ bar and $n = 2000$ rpm).
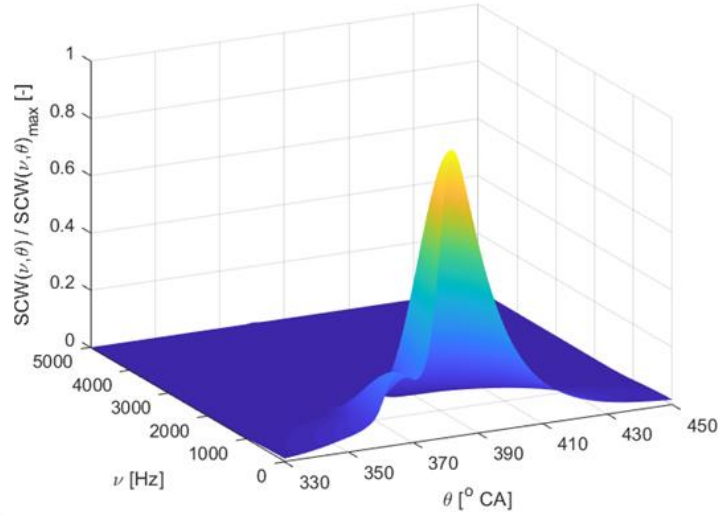
Figure 5.14: Normalized smoothed Choi-Williams distribution ($bmep = 2$ bar and $n = 2000$ rpm).

stage pertaining to the pilot combustion, that is cool flames. An unnoticeable heat has been released during this combustion stage and it finishes when $\bar{\nu}'(\theta)$ reaches back again to zero (point 2). The secondary combustion stage of the pilot combustion refers to the hot flames and it begins from point 3 where a local minimum $\bar{\nu}(\theta)$ value is reached. The overall ignition delay is defined on the basis of point 3 since it refers to SOC. After that, the diffusive combustion, also named as pool flames, begins at the inflection point of $\bar{\nu}(\theta)$ (point 4). The diffusive combustion of the pilot injection continues until $\bar{\nu}'(\theta)$ increases up to a local maximum value which is point 5. Meanwhile, the fuel evaporation pertaining to the main injected fuel starts and it leads to an increasing phase of $\bar{\nu}'(\theta)$. At around $\theta \approx 372\ °CA$, $\bar{\nu}'(\theta)$ equals to zero and $\bar{\nu}(\theta)$ reaches the local minimum value, it indicates the SOC of main combustion. The main combustion process is composed of two stages, that are premixed and diffusive combustion. The separation of these two phases has been detected by point 7 when $\bar{\nu}'(\theta)$ reached the minimum value. The end of diffusive combustion is defined on the basis of x_b same as the single injection condition.

As shown in Fig. 5.13, the intensive premixed combustion results in a larger combustion noise than in Fig. 5.9. Two significant peaks could be

observed in the instantaneous combustion noise pattern in Fig. 5.13 under the pilot-main injection schedule. It is also in line with the two bumps detected in the smoothed Choi-Williams distribution shown in Fig. 5.14. The first remarkable increase is due to the pilot premixed combustion phase while the latter one is caused by the main premixed phase.

The split of the overall combustion noise $Cn_{\Delta p}$ has been evaluated and reported in Table 5.5. It could be concluded that the dominant contribution to the total combustion noise is the main premixed phase, then the pilot hot flames. The diffusive phases pertaining to the pilot and main combustion generate small portions of combustion noise while the cool flames occurred during pilot combustion makes the lowest contribution.

5.8   Double injections medium load condition

Another pilot-main double injection working point ($bmep = 8$ bar and $n = 2500$ rpm) has been analysed and analogous variables as in Figs. 5.9, 5.11 and 5.13 have been plotted in Fig. 5.15. Under this case, during the pilot injection no cool flames have been presented due to the sufficient high in-cylinder pressure and temperature, not like the situation in Fig. 5.13. In this way, the HRR pattern exhibits a single-stage ignition pertaining to the pilot combustion. After the fuel is injected during the pilot shot, $\bar{\nu}(\theta)$ tends to decrease due to the evaporation process and this reaches a local minimum value, indicated as point 1.As soon as the pilot combustion starts, the HRR curve shows positive value. Zero value of $\bar{\nu}'(\theta)$ indicates the starting point of the pilot combustion and it is point 1 in Fig. 5.15. A high pressure rise rate is presented in $\bar{\nu}(\theta)$ since the premixed combustion phase is occurred for pilot combustion. The latter stage, that is the combustion with pool flames, begins from point 2 and $\bar{\nu}(\theta)$ tends to be stable. This stage continues until

Table 5.5: Combustion noise subdivision($bmep = 2$ bar and $n = 2000$ rpm)

Combustion stage	$Cn_{\Delta p}[dBA]$
Pilot cool flames (1-2)	5.9
Pilot hot flames (3-4)	17.9
Pilot pool flames (4-5)	9.6
Main premixed phase (6-7)	30.7
Main diffusive phase (7-8)	7.2

$\bar{\nu}'(\theta)$ reaches the minimum value, indicated as point 3. The subsequent further reduction of $\bar{\nu}(\theta)$ is caused by main injected fuel evaporation. With regard to the main injection, the starting time is detected by examining the minimum value in $\bar{\nu}(\theta)$ or the zero point of $\bar{\nu}'(\theta)$ which is indicated as point 4. Two combustion stages have been presented in the main combustion event. The premixed combustion results in a rapid increasing phase in $\bar{\nu}(\theta)$ during the period between $\theta \approx 365$ °CA to $\theta \approx 368$ °CA and the starting and end point have been detected through $\bar{\nu}'(\theta)$: zero value indicated as point 4 and the local minimum value point 5. During the latter diffusive combustion phase, $\bar{\nu}'(\theta)$ continues to decrease and the combustion ends when $x_b = 0.95$, indicated as point 6. Similarly, as in Fig. 5.14, two bumps could be notices in the 3D plot of the smoothed Choi-Williams distribution displayed in Fig. 5.16. The first peak is related to the pilot combustion and the latter one refers to the main combustion event.
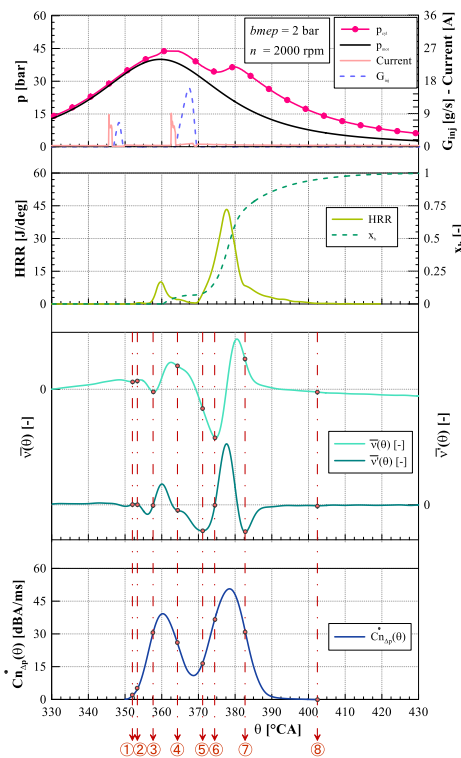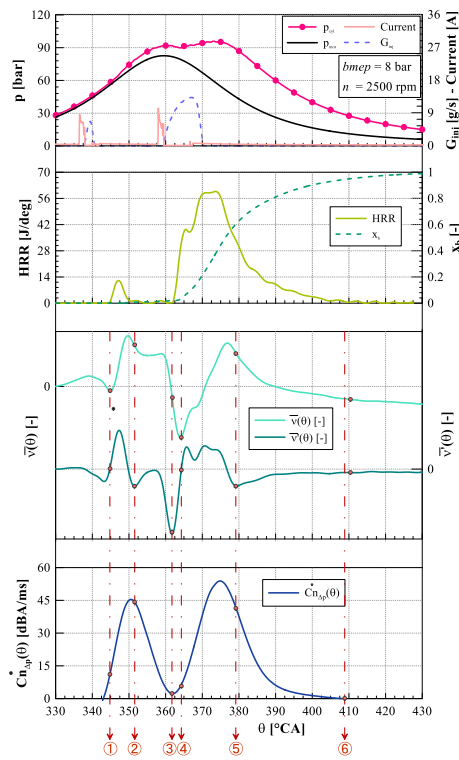

Figure 5.15: Double injection ($bmep = 8$ bar and $n = 2500$ rpm).
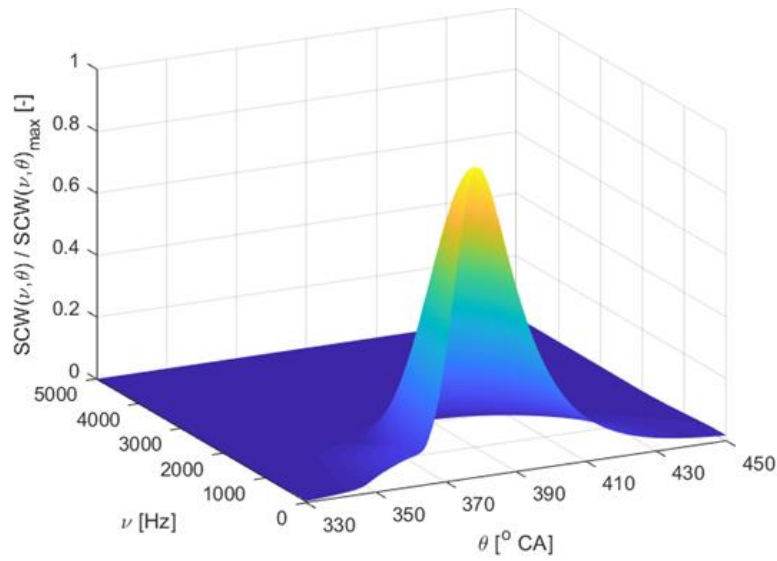
Figure 5.16: Normalized smoothed Choi-Williams distribution ($bmep = 8$ bar and $n = 2500$ rpm).

Based on the information derived from $\bar{\nu}(\theta)$ and $\bar{\nu}'(\theta)$, different combustion stages have been identified as have shown above and then by evaluating the corresponding combustion noise. The results have been summarized in Table 5.6. There are two significant growing phases of the instantaneous combustion noise $\dot{C}n_{\Delta p}(\theta)$ occurring from $\theta \approx 354$ °CA to $\theta \approx 350$ °CA and $\theta \approx 365$ °CA to $\theta \approx 380$ °CA which correspond to the premixed phases pertaining to the pilot and main injections. Finally, the instantaneous combustion noise $\dot{C}n_{\Delta p}(\theta)$ starts to gradually reduce into zero during the diffusive combustion stage. Based on the result shown in Table 5.6, it could be inferred that the main premixed combustion stage shares the biggest contribution to the overall combustion noise and this could be explained by its characteristics. The pilot premixed flames and the main diffusive combustion stage also generate remarkable proportions of combustion noise since they undergo a long period. Although the heat released by the pilot pool flames is relatively small, the generated combustion noise is not negligible.

Table 5.6: Combustion noise subdivision($bmep = 8$ bar and $n = 2500$ rpm)

Combustion stage	$Cn_{\Delta p}[dB]$
Pilot premixed (1-2)	15.4
Pilot pool flames (3-4)	13.9
Main premixed phase (4-5)	38.6
Main diffusive phase (5-6)	15.7

Chapter 6

Conclusions

6.1 Overview

In this work, different topics with regard to the diesel engines have been investigated. The diesel Common Rail system control has been carried out with the aid of a fully developed numerical model which is integrated with the proportional-integrative-derivative (PID) controller and the pressure control valve submodels. The parametric analyses on the PID controller has been studied under different engine working conditions. Moreover, the effect of the accumulator size on the rail pressure time history has been carried out and it suitable solutions for a fuel injection system without rail have been determined. With regard to the fuel injection system architectures, an innovative Common Feeding (CF) fuel injection system with the absence of rail has been developed for light duty commercial vehicle. Numerical and experimental tests have been performed with different accumulator volumes integrated at the pump delivery for various injection strategies. Then, the injected quantity control strategy based on time-frequency analysis has been carried out. By analyzing the injector inlet pressure signal with the short time Fourier transform, the injection temporal length (ITL) has been obtained. Therefore, a correlation based on ITL and the rail pressure can be used, that is independent on the fuel temperature. Finally, the instantaneous combustion noise has been assessed based on the time-frequency analysis technique. The input parameter is the in-cylinder pressure signal, measured on a Euro 5 diesel engine during the combustion process, and the quantitative contribution pertaining to the different combustion phases can be evaluated.

6.2 Results and discussion

6.2.1 CR injection apparatus modelling and analysis for the standard and decreased volume sizes

In Chap. 2, the submodels of the PID controller and the pressure control valve have been accessed and integrated in a previously prepared CR fuel injection system model. The fully predictive model has been validated with various steady state working conditions in terms of rail pressure and injected flowrate traces. The transient working conditions have been applied to the injection system in order to analyse the dynamic response of the presented pressure control system. The effect of the proportional, integrative and derivative gains on the system response have been studied. In general, a larger integrative gain gives a faster system response but results in a bigger pressure overshoot. When the pressure target is reached, the amplitude of the pressure oscillations tends to decrease by applying a higher value of K_i. When K_p increases, the settling time and the overshoot decreases but a bigger pressure oscillation under stable condition is occurred. Based on the study, K_p should be responsible for the overshoot amplitude control and K_i should be adjusted to reach an optimized steady-state error. As far as the derivative gain has been concerned, its effect on the pressure control during the transient working condition is negligible and it could be set to $K_d = 0$. Moreover, when the accumulator size is significantly decreased into 2.5 mm^3, the influence of the accumulator size on the rail pressure has been investigated. It has been found that the large reduction in V_{rail} is not helpful for the system pressure response under a pressure step transient condition. Compared with a bigger V_{rail}, p_{rail} begins to increase more steeply at the beginning but later the pressure rise rate starts to decrease. By modifying the PID parameters, the Minirail layout could reach the same dynamic response as the standard one during the pressure step transient but the performance can not be enhanced. The aim is to investigate the possibility of the realization of a fuel injection system without rail layout.

6.2.2 Application of a prototypal Common Feeding injection system

In Chap. 3, an innovative Common Feeding fuel injection system which is benefit from the easier installation process and lower manufacturing cost has been achieved for the Asian market. The proposed apparatus has been compared with the standard Common Rail system in order to analyse the injection performance under single and double injections strategies. With regard to the single injections, no noticeable difference has been observed between the two layouts when a small quantity has been injected. For a big injection, a smaller accumulator size generates a bigger pressure drop at the beginning since it is not able to maintain the average pressure during the injection event. In this way ECU has been adjusted to control the mean rail pressure and the initial pressure when the injection is not performed is much higher for a smaller accumulator size for the aim of compensation. It leads to a higher initial injection rate and a minor change has been found in the injector characteristics. Moreover, the frequency of the pressure oscillation has been changed since the accumulator shape has been modified. For a smaller V_{rail}, the cycle-to.cycle dispersion pertaining to the injected quantity increases but still in an acceptable range. Regarding to the double injections, for the pilot-main injections, the injector inlet pressure traces of different rail sizes layouts show similar trends when the pilot injection is not performed. The main injected mass is influenced greatly by the generated pressure waves due to the pilot injection, and the $V_{inj,main}$ vs DT features the same fluctuation frequency as the one in the standard layout. Analogous performance has been shown for the main-after injections. The performance simulation has been realized by applying a 1D numerical model. Based on the modelling result, when the rail volume size is reduced, the needle lift value is bigger and the opening velocity is augmented, the injection duration is longer. With regard to pilot-main injections, the main injected quantity tends to increase for a smaller accumulator size and it could be explained by the higher pressure existing in the delivery chamber.

6.2.3 Closed-loop control strategy of injected mass on the basis of time-frequency analysis

In Chap.4, a closed-loop control working on the fuel injected quantity has been carried out and realized. The presented control algorithm provides the development on achieving a cleaner and more efficient diesel engine. The injected mass has been real-time estimated on the basis of the time-frequency analysis applying on the captured injector inlet pressure signal. Single injections tests have been performed with this methodology to verify its reliability. Firstly, the thermal regime of the injector influence on the injected quantity has been studied by applying same working point under different T_{tank}. It has been discovered that the ITL value is responsible for the different injection rate patterns when T_{tank} varies. As a result, the injected mass could achieve a more accurate estimation based on the correlation between p_{nom} and ITL instead of ET. A TFA -based virtual sensor of the needle lift has been developed and designed for the estimation of the ITL. ITL has been computed through the two time instants identified from the MIF trend pertaining to the injector inlet pressure. After the energizing current, the first maximum value of MIF refers to the nozzle opening and it is defined as the starting time instant of the injection. The ending time instant could be detected by the maximum local value of MIF and it is explained by the induced water hammer effect when the injection is finished. The time duration between the starting time and ending time instants gives the injection duration, that is the estimated ITL_{est}. By applying the correlation in terms of the nominal pressure and ITL_{est}, the injected mass could be estimated and the procedure has been applied to an extended working points in order to check its accuracy. Based on the single injections result, it could be observed that the accuracy of the presented methodology aiming for estimating the injected mass features an error below 1.5 mg and the majority of the considered points are within 1 mg. The error of the injected mass estimation is given by two aspects: one corresponds to the $ITL - M_{inj}$ correlation and the other is to the inaccuracy of ITL_{est}. The proposed algorithm could be implemented in the control system in order to control the injected mass pertaining to the single injection or to the pilot injection or to an after injection of the multiple injection strategy.

6.2.4 Time-frequency analysis application to combustion noise in CI engines

In Chap. 5, time-frequency analysis has been applied to the Δp_{comb} pressure trace for the analysis of the combustion noise. With the aid of the mean instantaneous frequency information, the combustion noise evaluated on the basis of TFA is able to provide a detailed information related to the combustion process. The mean instantaneous frequency and its derivative have been applied to detect the combustion phases and the direct combustion noise contribution generated by Δp_{comb} with regard to the corresponding phase could be evaluated in order to provide a quantitative analysis in time domain. Choi-Williams distribution has been plotted as a function of time and frequency in 3D version and the combustion noise trend could be observed. The presented $\dot{CN}_{\Delta p}$ analysis has been implemented to an early PCCI engine which features a big combustion noise. Single injections strategy has been performed: based on the results shown by time-frequency analysis, the cool flames generate a noticeable combustion noise although it releases a nearly negligible HRR. Analogous phenomena is presented for higher load working points for an early fuel injection timing. The dominant contribution to the total combustion noise is given by the premixed stage since a significantly high HRR has occurred under a short period. The latter stage, that is diffusive stage, also results in a noticeable $CN_{\Delta p}$ (the second in terms of magnitude after the premixed combustion) because this stage undergoes a long duration. As far as double injections have been concerned, two bumps could be observed in the 3D smoothed Choi-Williams distribution plot which are due to the pilot and main combustion events. The pilot premixed as well as main premixed stage result in two local peaks in $\dot{CN}_{\Delta p}$. In this way, during these two stages, the high levels of the direct combustion noise have been generated. As the combustion noise is also influenced by the combustion duration, a higher value of $\dot{CN}_{\Delta p}$ have been detected when a longer duration is occurred for pool flames and diffusive stage. A qualitative and quantitate study of the combustion noise could be obtained from Δp_{comb} analysis on the basis of TFA. The presented algorithm could be implemented for real-time monitoring and also for the combustion models development and investigation.

References

[1] F. Zhao, K. Chen, H. Hao, and Z. Liu. Challenges, potential and opportunities for internal combustion engines in china. *Sustainability*, 12(12):4955, Jun 2020.

[2] P. Arya F. Millo and F. Mallamo. Optimization of automotive diesel engine calibration using genetic algorithm techniques. *Energy*, 158:807–819, 2018.

[3] F. Leach, R. Ismail, M. Davy, A. Weall, and B. Cooper. The effect of a stepped lip piston design on performance and emissions from a high-speed diesel engine. *Applied Energy*, 215:679–689, 2018.

[4] C. Chen, W. Lee, L. Wang, Y. Chang, H. Yang, L. Young, J. Lu, Y. I. Tsai, M. Cheng, and J. K. Mwangi. Impact of high soot-loaded and regenerated diesel particulate filters on the emissions of persistent organic pollutants from a diesel engine fueled with waste cooking oil-based biodiesel. *Applied Energy*, 191:35–43, 2017.

[5] F. Yang, C. Yao, J. Wang, and M. Ouyang. Load expansion of a dieseline compression ignition engine with multi-mode combustion. *Fuel*, 171:5 – 17, 2016.

[6] K. Vakiti, J. Deussen, C. Pilger, H. Nanjundaswamy, T. Szailer, M. Franke, D. Tomazic, K. Thomas, M. Romijn, K. Deppenkemper, and G. Vagnoni. In-use compliance opportunity for diesel powertrains. In *SAE Technical Paper*. SAE International, 04 2018.

[7] G. Boccardo, F. Millo, A. Piano, L. Arnone, S. Manelli, S. Fagg, P. Gatti, O. Herrmann, D. Queck, and J. Weber. Experimental investigation on a 3000 bar fuel injection system for a scr-free non-road diesel engine. *Fuel*, 243:342 – 351, 2019.

[8] Z. Sun, G. Li, C. Chen, Y. Yu, and G. Gao. Numerical investigation on effects of nozzle's geometric parameters on the flow and the cavitation characteristics within injector's nozzle for a high-pressure common-rail DI diesel engine. *Energy Conversion and Management*, 89:843–861, 2015.

[9] A. Celik, M. Yilmaz, and O. Yildiz. Effects of vortex tube on exhaust emissions during cold start of diesel engines. *Applications in Energy and Combustion Science*, 6:100027, 2021.

[10] K. Prashanth, S. Amjad, Srinivasa T., and B. Pavan. Experimental investigation of argon gas induction on diesel engine performance and emission characteristics: A comprehensive study on de-nox techniques. *Process Safety and Environmental Protection*, 152:471–481, 2021.

[11] W. Zhao, J. Yan, S. Gao, T. Lee, and X. Li. The combustion and emission characteristics of a common-rail diesel engine fueled with diesel, propanol, and pentanol blends under low intake pressures. *Fuel*, 307:121692, 2022.

[12] Q. Lan, F. Fan, Y. Bai, Y. Gu, and L. Wen. Experimental and numerical investigation on pressure characteristics of the dual-valve controlled fuel system for low-speed diesel engines. *Fuel*, 294:120501, 2021.

[13] K. Ju, J. Kim, and J. Park. Numerical prediction of the performance and emission of downsized two-cylinder diesel engine for range extender considering high boosting, heavy exhaust gas recirculation, and advanced injection timing. *Fuel*, 302:121216, 2021.

[14] V. Gupta, Z. Zhang, and Z. Sun. Modelling and control of a novel pressure regulations mechanism for common rail fuel injection systems. *Applied Mathematical Modelling*, 35(7):3473–3483, 2011.

[15] O. Aydogdu and M. Korkmaz. A simple approach to design of variable parameter nonlinear pid controller. *International Conference Advancements in Information Technology*, 2011.

[16] H. Hua, N. Ma, J. Ma, and H. Huang. Design of rail pressure tracking controller for novel fuel injection system. *Journal of Shanghai Jiaotong University*, 18(3):264–270, 2013.

[17] A. Ferrari and E. Salvo. Determination of the transfer function between the injected flow-rate and high-pressure time histories for improved control of common rail diesel engines. *International Journal of Engine Research*, 18(3):212–225, 2017.

[18] W. Xiao, F. Liang, W. Tan, X. Mao, L. Yang, and B. Zhuo. Analysis of common rail pressure build-up and assistant-establishment of engine phase position in starting process. *SAE Paper*, (2006-01-3525), 2006.

[19] A. E. Catania and A. Ferrari. Development and performance assessment of the new-generation cf fuel injection system for diesel passenger cars. *Applied Energy*, 91(1):483–495, 2012.

[20] A. E. Catania, A. Ferrari, and E. Spessa. Numerical-experimental study and solutions to reduce the dwell time threshold for fusion-free consecutive injections in a multijet solenoid-type cr system. *Journal of Engineering for Gas Turbines and Power*, 131(2):022804–1–022804–14, 2009.

[21] A. Ferrari and P. Pizzo. Fully predictive common rail fuel injection apparatus model and its application to global system dynamics analyses. *International Journal of Engine*, 18(3):273–290, 2017.

[22] N. Hambali, A. Masngut, A. Ishak, and Z. Janin. Process controllability for flow control system using ziegler-nichols (zn), cohen-coon (cc) and chien-hrones-reswick (chr) tuning methods. *Proceeding IEEE International Conference on Smart Instrumentation, Measurement and Applications*, 2014.

[23] Z. Jin, O. Vento, T. Zhang, A. Ferrari, A. Mittica, L. Ouyang, and S. Tan. Numerical-experimental optimization of the common-feeding injection system concept for application to light-duty commercial vehicles. *Journal of Energy Resources Technology*, 143(12):122304, 2021.

[24] J. Zhao, K. Wei, and P. Yue. Investigation of maximum temperature rise on high pressure common rail injector nozzle. Technical report, SAE Technical Paper, 2019.

[25] W. Naoki, W. Naoki, S. Scott, C. Emre, Y. Koji, and P. Lyle. Ignition and soot formation/oxidation characteristics of compositionally unique international diesel blends. Technical report, 2019.

[26] V. Soloiu, R. Gaubert, M. Muinos, J. Moncada, T. Beyerl, and G. Molina. Development and implementation of a common rail fuel injection system for flexible combustion for an experimental medium duty diesel engine. Technical report, SAE Technical Paper, 2017.

[27] A. Risi, T. Donateo, and D. Laforgia. Optimization of the combustion chamber of direct injection diesel engines. *SAE transactions*, 112:1437–1445, 2003.

[28] J. Weber, Olaf E. H, R. Puts, J. Kawamura, Y. Tomida, and M. Mashida. Next improvement potentials for heavy-duty diesel engine - tailor the fuel injection system to the combustion needs. *SAE International journal of engines*, 10:1119–1127, 2017.

[29] D. Kurczyński and P. Łagowski. Performance indices of a common rail-system ci engine powered by diesel oil and biofuel blends. *Journal of The Energy Institute*, 92:1897–1913, 2019.

[30] A. Ferrari, F. Paolicelli, and P. Pizzo. The new-generation of solenoid injectors equipped with pressure-balanced pilot valves for energy saving and dynamic response improvement. *Applied Energy*, 151:367–376, 2015.

[31] J. Hammer, D. Naber, M. Raff, and D. Zeh. Bosch diesel fuel injection system–with modularity from entry up to high-end segment. In *9. Tagung Diesel-und Benzindirekteinspritzung 2014*, pages 1–15. Springer, 2015.

[32] A. Ferrari, A. Mittica, and E. Spessa. Benefits of hydraulic layout over driving system in piezo-injectors and proposal of a new-concept cr injector with an integrated minirail. *Applied energy*, 103:243–255, 2013.

[33] K. Serizawa, D. Ueda, N. Mikami, Y. Tomida, and J. Weber. Realizing robust combustion with high response diesel injector with controlled diffusive spray nozzle and closed loop injection control. Technical report, 2017.

[34] K. Suh. Development of wobble-plate-type fuel pump in compression ignition engine fueled with dimethyl ether. *Journal of Energy Resources Technology*, 137(3), 2015.

[35] K. Ishiduka, K. Uchiyama, K. Higuchi, N. Yamada, K. Takeuchi, and O. Herrmann. Further innovations for diesel fuel injection systems: Close-loop control of fuel quantity by i-art. In *19th Aachen Colloquium, Aachen, Germany*, 2015.

[36] A. Ferrari, C. Novara, E. Paolucci, O. Vento, M. Violante, and T. Zhang. Design and rapid prototyping of a closed-loop control strategy of the injected mass for the reduction of co2, combustion noise and pollutant emissions in diesel engines. *Applied Energy*, 232:358–367, 2018.

[37] A. Ferrari, C. Novara, E. Paolucci, O. Vento, M. Violante, and T. Zhang. A new closed-loop control of the injected mass for a full exploitation of digital and continuous injection-rate shaping. *Energy Conversion and Management*, 177:629–639, 2018.

[38] K. Zhang, Z. Xie, and M. Zhou. Model-based optimization and pressure fluctuation control of pressure reservoir in electrically controlled fuel injection system for single cylinder diesel engine. In *Internal Combustion Engine Division Fall Technical Conference*, volume 58325, page V002T07A002. American Society of Mechanical Engineers, 2017.

[39] A. Ferrari, F. Paolicelli, and P. Pizzo. Hydraulic performance comparison between the newly designed common feeding and standard common rail injection systems for diesel engines. *Journal of Engineering for Gas Turbines and Power*, 138(9), 2016.

[40] R. Finesso, E. Spessa, and Y. Yang. Fast estimation of combustion metrics in DI diesel engines for control-oriented applications. *Energy Conversion and Management*, 112:254–273, 2016.

[41] T. Wintrich, J. Hammer, D. Naber, M. Raff, Claudius Rath, Andreas Stapelmann, Jürgen Meusel, Holger Gödeke, and K. Prevel. Motorsysteme. In Johannes Liebl and Christian Beidl, editors, *Internationaler Motorenkongress 2015*, pages 165–211, Wiesbaden, 2015. Springer Fachmedien Wiesbaden.

[42] L. Wang, G. Li, C. Xu, X. Xi, X. Wu, and S. Sun. Effect of characteristic parameters on the magnetic properties of solenoid valve for high-pressure common rail diesel engine. *Energy Conversion and Management*, 127:656–666, 2016.

[43] A. Ferrari and A. Mittica. Response of different injector typologies to dwell time variations and a hydraulic analysis of closely-coupled and continuous rate shaping injection schedules. *Applied Energy*, 169:899–911, 2016.

[44] C. A. MacCarley, W. D. Clark, and K. T. Nakae. An indirect sensing technique for closed-loop diesel fuel quantity control. *SAE transactions*, pages 188–196, 1990.

[45] F. Yan and J. Wang. In-cylinder oxygen mass fraction cycle-by-cycle estimation via a lyapunov-based observer design. In *Proceedings of the 2010 American Control Conference*, pages 652–657, 2010.

[46] T. Miyaura, A. Morikawa, Y. Ito, K. Ishizuka, and T. Tsuiki. Development of diesel engine using new fuel injection system-direct monitoring of fuel injection pressure using injector with built-in sensor, and its applications. Technical Report 2013-01-1739, SAE Technical Paper, 2013.

[47] J. Hammer, M. Raff, and D. Naber. Advanced diesel fuel injection equipment–a never ending BOSCH story. In *14. Internationales Stuttgarter Symposium*, pages 31–45. Springer, 2014.

[48] P. Voigt, H. Schiffgens, C. Daveau, J. Ogé, J. Béduneau, G. Meissonier, C. Tapin, and X. Lalé. Delphi injector closed loop control strategy using the "Switch" technology for diesel passenger cars–injector hardware. In *10. Tagung Diesel-und Benzindirekteinspritzung 2016*, pages 41–66. Springer, 2017.

[49] Z. Feng, M. Liang, and F. Chu. Recent advances in time–frequency analysis methods for machinery fault diagnosis: A review with application examples. *Mechanical Systems and Signal Processing*, 38(1):165–205, 2013.

[50] G. Purushottam and T. Rajiv. Multifault diagnosis of induction motor at intermediate operating conditions using wavelet packet transform and support vector machine. *Journal of Dynamic Systems, Measurement, and Control*, 140(8), 2018.

[51] T. Ahmad, G. Barat, T. Teymour, M. Saeid, R. Abbas, and A. Mohsen. Characterization of engine's combustion-vibration using diesel and biodiesel fuel blends by time-frequency methods: A case study. *Renewable Energy*, 95:422–432, 2016.

[52] T. Ahmad and A. MAlireza. Fault detection of injectors in diesel engines using vibration time-frequency analysis. *Applied Acoustics*, 143:48–58, 2019.

[53] S. Ji, X. Lan, J. Lian, H. Wang, M. Li, Y. Cheng, and W. Yin. Combustion parameter estimation for ice from surface vibration using frequency spectrum analysis. *Measurement*, 128:485–494, 2018.

[54] A. Ferrari and F. Paolicelli. A virtual injection sensor by means of time frequency analysis. *Mechanical Systems and Signal Processing*, 116:832–842, 2019.

[55] I. Jung, J. Jin, D. Lee, S. Lee, S. Yang, and K. Min. Closed-loop control method for monitoring and improving the diesel combustion noise. Technical report, SAE Technical Paper, 2016.

[56] A. Broatch, X. Margot, R. Novella, and J. Gómez-Soriano. Combustion noise analysis of partially premixed combustion concept using gasoline fuel in a 2-stroke engine. *Energy*, 107:612–624, 2016.

[57] S. Wang, C. Chalu, N. Duclaux, and M. Paquien. Noise optimization of diesel engines with new combustion systems. *SAE International Journal of Passenger Cars-Mechanical Systems*, 2(2009-01-2081):1387–1395, 2009.

[58] A. Broatch, R. Novella, J. Soriano, P. Pal, and S. Som. Numerical methodology for optimization of compression-ignited engines considering combustion noise control. *SAE International Journal of Engines*, 11:625–642, 2018.

[59] Q. Ma, Q. Zhang, J. Liang, and C. Yang. The performance and emissions characteristics of diesel/biodiesel/alcohol blends in a diesel engine. *Energy Reports*, 7:1016–1024, 2021.

[60] T. Nguyen and M. Mikami. Effect of hydrogen addition to intake air on combustion noise from a diesel engine. *International Journal of Hydrogen Energy*, 38(10):4153–4162, 2013.

[61] J. Dernotte, J. Dec, and C. Ji. Investigation of the sources of combustion noise in hcci engines. *International Journal of Engines*, 7(2):730–761, 2014.

[62] M. E. Badaouia, J. Danie, F. Guillet, and C. Serviere. Separation of combustion noise and pistonslap in diesel engine—part i: Separation of combustion noise and piston-slap in diesel engine by cyclic wiener filtering. *Mechanical Systems and Signal Processing*, 19:1209–1217, 2005.

[63] C. Serviere, J. Lacoumea, and M. Badaoui. Separation of combustion noise and piston-slap in diesel engine—part ii: Separation of combustion noise and piston-slap using blind source separation methods. *Mechanical Systems and Signal Processing*, 19:1218–1229, 2005.

[64] E. Giakoumis, A. Dimaratos, and C. Rakopoulos. Experimental study of combustion noise radiation during transient turbocharged diesel engine operation. *Energy*, 36(8):4983–4995, 2011.

[65] C. Giancarlo, C. Ornella, P. Fulvio, and P. Andrea. Diagnostic methodology for internal combustion diesel engines via noise radiation. *Energy Conversion and Management*, 89:34–42, 2015.

[66] A. Dowling and Y. Mahmoudi. Combustion noise. *Proceedings of the Combustion Institute*, 35:65–100, 2015.

[67] G. Shu, H. Wei, and R. Han. The transfer function of combustion noise in di-diesel engine. *SAE Technical Paper*, pages 2005–01–2486, 2005.

[68] A. Torregrosa, A. Broatch, R. Novella, and L. Mónico. Suitability analysis of advanced diesel combustion concepts for emissions and noise control. *Energy*, 36:825–838, 2011.

[69] G. Shibata, H. Ushijima, H. Ogawa, and Y. Shibaike. Combustion noise analysis of premixed diesel engine by engine tests and simulations. *SAE Technical Paper*, pages 2014–01–1293, 2014.

[70] S. d'Ambrosio, A. Ferrari, D. Iemmolo, and A. Mittica. Dependence of combustion noise on engine calibration parameters by means of the response surface methodology in passenger car diesel engines. *Applied Thermal Engineering*, 163:114209, 2019.

[71] G. Zamboni. Influence of fuel injection, turbocharging and egr systems control on combustion parameters in an automotive diesel engine. *Applied Science*, 9(3):484, 2019.

[72] K. Torii. Method using multiple regression analysis to separate engine radiation noise into the contributions of combustion noise and mechanical noise in the time domain. *SAE International Journal of Engines*, 7(3):1502–1513, 2014.

[73] A. Maruyama and G. Naoe. Study on combustion noise in small general purpose engines. *SAE Technical Paper*, pages 2014–32–0105, 2014.

[74] A. Singh, V. Kumar, and A. Agarwal. Evaluation of comparative engine combustion, performance and emission characteristics of low temperature combustion (pcci and rcci) modes. *Applied Energy*, 278:115644, 2020.

[75] V. Chaudhari and D. Deshmukh. Diesel and diesel-gasoline fuelled premixed low temperature combustion (ltc) engine mode for clean combustion. *Fuel*, 266:116982, 2020.

[76] E. Shim, H. Park, and C. Bae. Comparisons of advanced combustion technologies (hcci, pcci, and dual-fuel pcci) on engine performance and emission characteristics in a heavy-duty diesel engine. *Fuel*, 262:116436, 2020.

[77] S. Juttu, S. Gothekar, N. Marathe, N. Walke, and S. Dev. Cost effective bs-vi solution - a combined low temperature combustion and conventional diesel combustion concepts. *SAE International Journal of Advances and Current Practices in Mobility*, 1(1):45–54, 2019.

[78] G. Shibata, H. Ogawa, Y. Amanuma, and Y. Okamoto. Optimization of heat release shape and the connecting rod crank radius ratio for low engine noise and high thermal efficiency of premixed diesel engine combustion. *SAE Technical Paper*, pages 2015–01–0825, 2015.

[79] S. d'Ambrosio and A. Ferrari. Boot injection dynamics and parametrical analysis of boot shaped injections in low-temperature combustion diesel engines for the optimization of pollutant emissions and combustion noise. *Energy*, 134:420–437, 2017.

[80] A. Torregrosa, A. Broatch, R. Novella, J. Soriano, and L. Monico. Impact of gasoline and diesel blends on combustion noise and pollutant emissions in premixed charge compression ignition engines. *Energy*, 137:58–68, 2017.

[81] F. John, M. Patrick, and O. Axel. Internal combustion engine operable in pcci mode with postignition injection and method of operation. *US6684852B2*.

[82] S. Wang, C. Chalu, and F. Gautier. Optimization of combustion noise of modern diesel engines for passenger cars. *SAE Technical Paper*, 137:58–68, 2007.

[83] S. Busch, K. Zha, A. Warey, F. Pesce, and R. Peterson. On the reduction of combustion noise by a close-coupled pilot injection in a small-bore di diesel engine. *ASME 2015 Internal Combustion Engine Division Fall Technical Conference ICEF2015-1004*, 2015.

[84] E. Plamondon and P. Seers. Parametric study of pilot–main injection strategies on the performance of a light-duty diesel engine fueled with diesel or a wco biodiesel–diesel blend. *Fuel*, 236:1273–1281, 2019.

[85] A. Torregrosa, A. Broatch, A. García, and L. Mónico. Sensitivity of combustion noise and nox and soot emissions to pilot injection in pcci diesel engines. *Applied Energy*, 104:149–157, 2013.

[86] W. Park, Y. Ra, E. Kurtz, W. Willems, and R. Reitz. Use of multiple injection strategies to reduce emission and noise in low temperature diesel combustion. *SAE Technical Paper*, 177:2015–01–0831, 2015.

[87] B. Vaglieco. Multiple injection diesel combustion process in the high-speed direct injection diesel engine. *Advanced Direct Injection Combustion Engine Technologies and Development*, pages 155–174, 2010.

[88] S. Mendez and B. Thirouard. Using multiple injection strategies in diesel combustion: potential to improve emissions, noise and fuel economy trade-off in low cr engines. *SAE International Journal of Fuels and Lubricants*, 1(1):662–674, 2009.

[89] M. Denny, L. Ende, H. Persson, and Ö. Andersson. Manipulating heat release features to minimize combustion noise. *Fuel*, 263:116613, 2020.

[90] I. Arsie, R. Leo, C. Pianese, and M. Cesare. Combustion noise and pollutants prediction for injection pattern and egr tuning in an automotive common-rail diesel engine. *IFAC Proceedings*, 45(30):456–465, 2012.

[91] A. Torregrosa, A. Broatch, A. Gil, and J. Soriano. Numerical approach for assessing combustion noise in compression-ignited diesel engines. *Applied Acoustics*, 135:91–100, 2018.

[92] A. Ferrari, A. Mittica, P. Pizzo, and Z. Jin. Pid controller modelling and optimization in cr systems with standard and reduced accumulators. *International Journal of Automotive Technology*, 19(15):771–781, 2018.

[93] A. Ferrari, Z. Jin, O. Vento, and T. Zhang. An injected quantity estimation technique based on time–frequency analysis. *Control Engineering Practice*, 116:104910, 2021.

[94] A. Ferrari and R. Vitali. Instantaneous torque, energy saving and flow-rate ripple analysis of a common rail pump equipped with different delivery-pressure control systems. *International Journal of Engine Research*, 19(10):1036–1047, 2017.

[95] K. L. Chien, J. A. Hrones, and J. B. Reswick. On the automatic control of generalized passive systems. *Transactions of the American Society of Mechanical Engineering*, 74:175–185, 1952.

[96] G. Cohen and G. Coon. Theoretical consideration of retarded control. *Transactions of the American Society of Mechanical Engineering*, 75:827–834, 1953.

[97] J. G. Ziegler and N. B. Nichols. Optimum settings for automatic controllers. *Transactions of the American Society of Mechanical Engineering*, 64:759–768, 1942.

[98] K. J. Åström and T. Hägglund. Pid controllers: Theory, design and tuning. *2nd edition International Society of Americag*, 1995.

[99] J. J. Gude and E. Kahoraho. Kappa-tau type pi tuning rules for specified robust levels. *2nd IFAC Conference on Advances in PID Control*, 2012.

[100] M. Baratta, A. E. Catania, and A. Ferrari. Hydraulic circuit design rules to remove the dependence of the injected fuel amount on dwell time in multijet cr systems. *Journal of Fluids Engineering*, 130(12):121104–1–121104–13, 2008.

[101] A.E. Catania, A. Ferrari, and E. Spessa. Temperature variations in the simulation of high-pressure injection-system transient flows under cavitation. *International Journal of Heat and Mass Transfer*, 51:2090–2107, 2008.

[102] A. E. Catania and A. Ferrari. Development and assessment of a new operating principle for the measurement of unsteady flow rates in high-pressure pipelines. *Flow Measurement and Instrumentation*, 20(6):230–240, 2009.

[103] S. d'Ambrosio and A. Ferrari. Effects of pilot injection parameters on low temperature combustion diesel engines equipped with solenoid injectors featuring conventional and rate-shaped main injection. *Energy Conversion and Management*, 110:457–468, 2016.

[104] A. Ferrari and A. Mittica. Fem modeling of the piezoelectric driving system in the design of direct-acting diesel injectors. *Applied Energy*, 99:471–483, 2012.

[105] A. E. Catania, A. Ferrari, M. Manno, and E. Spessa. Experimental investigation of dynamics effects on multiple-injection common rail system performance. *ASME J. Eng. Gas Turbines Power*, 131(3):032806, 2008.

[106] A. Ferrari and T. Zhang. Influence of the injector setup on digital and continuous injection rate-shaping performance in diesel engine passenger cars. *Energy Conversion and Management*, 205:112259, 2020.

[107] A. Ferrari and O. Vento. Influence of frequency-dependent friction modeling on the simulation of transient flows in high-pressure flow pipelines. *ASME J. Fluids Eng.*, 142(8):081205, 2020.

[108] A. Ferrari and T. Zhang. Benchmark between bosch and zeuch method–based flowmeters for the measurement of the fuel injection rate. *International Journal of Engine Research*, 22(1):316–327, 2021.

[109] A.E. Catania, A. Ferrari, and E. Spessa. Temperature variations in the simulation of high-pressure injection-system transient flows under cavitation. *International Journal of Heat and Mass Transfer*, 51(7-8):2090–2107, 2008.

[110] A. Ferrari and A. Mittica. Thermodynamic formulation of the constitutive equations for solids and fluids. *Energy conversion and management*, 66:77–86, 2013.

[111] R. Payri, F. Salvador, M. Carreres, and J. D. L. Morena. Fuel temperature influence on the performance of a last generation common-rail diesel ballistic injector. part ii: 1d model development, validation and analysis. *Energy Conversion and Management*, 114:376–391, 2016.

[112] F. J. Salvador, J. Gimeno, M. Carreres, and M. Crialesi-Esposito. Fuel temperature influence on the performance of a last generation common-rail diesel ballistic injector. part i: Experimental mass flow rate measurements and discussion. *Energy Conversion and Management*, 114:364–375, 2016.

[113] C. Öztürk. Development of experimental techniques to minimise the leakage errors involved in fft based measurements. *Applied Acoustics*, 44(4):375–382, 1995.

[114] A. Ferrari and O. Vento. Influence of frequency-dependent friction modeling on the simulation of transient flows in high-pressure flow pipelines. *Journal of Fluids Engineering*, 142(8), 2020.

[115] Q. Fang, J. Fang, J. Zhuang, and Z. Huang. Influences of pilot injection and exhaust gas recirculation (egr) on combustion and emissions in a hcci-di combustion engine. *Journal Fluid Engineering*, 48(7), 2012.

[116] A. Austen and T. Priede. Origins of diesel engine noise. Technical report, SAE Technical Paper, 1959.

[117] Avl concerto v3.9 help manual. Technical report.

[118] S. d'Ambrosio, A. Ferrari, and L. Galleani. In-cylinder pressure-based direct techniques and time frequency analysis for combustion diagnostics in ic engines. *Energy Conversion and Management*, 99:299–312, 2015.

[119] G. M. Rassweiler and L. Withrow. Motion pictures of engine flames correlated with pressure cards. *SaE transactions*, pages 185–204, 1938.

[120] L. Cohen. Time frequency analysis: Theory and applications. 1994.

[121] H. Choi and J. William. Improved time-frequency representation of multicomponent signals using exponential kernels. *IEEE Trans. Acoust. Speech Signal Process.*, 37:862–871, 1989.

[122] J. Antoni. Cyclostationarity by examples. *Mechanical Systems and Signal Processing*, 23(4):987–1036, 2009.

[123] F. Hlawatsch, T. Manickam, R. Urbanke, and W. Jones. Smoothed pseudo-wigner distribution, choi-williams distribution, and cone-kernel representation: Ambiguity-domain analysis and experimental comparison. *Signal Processing*, 43(2):149–168, 1995.

[124] G. Folland and A. Sitaram. The uncertainty principle: a mathematical survey. *The Journal of Fourier Analysis and Applications*, 3(3):207–238, 1997.

[125] L. Beranek and T. Mellow. Acoustics (second edition) chapter 1 introduction and terminology. *Sound Fields, Transducers and Vibration*, pages 1–23, 2019.

[126] A. Martyr and M. Plint. Engine testing: The design, building, modification and use of powertrain test facilities. *Elsevier*, 2012.

[127] A. Schwarz and J. Janicka. *Combustion noise*, volume 102. Springer Science & Business Media, 2009.

[128] R. Finesso and E. Spessa. A real time zero-dimensional diagnostic model for the calculation of incylinder temperatures, hrr and nitrogen oxides in diesel engines. *Energy Conversion and Management*, 79:498–510, 2014.